eXPRESS Polymer Letters Vol.1, No.6 (2007) 333
Available online at www.expresspolymlett.com
DOI: 10.3144/expresspolymlett.2007.47

Editorial corner – a personal view

Biohybrid polymers: novel options for regenerative therapies

C. Werner[*]

Max Bergmann Center of Biomaterials, Leibniz Institute of Polymer Research Dresden & Center for Regenerative Therapies Dresden, Hohe Str. 06, 01069 Dresden, Germany

With the advent of regenerative therapies morphogenetic matrices polymeric materials capable of rekindling the cellular potential to regenerate tissues and organs evolve into a new paradigm of biomaterials research: Advanced therapeutic concepts require biodegradable cell scaffolds transmitting spatio-temporal sequences of signals to trigger cellular fate decisions. To this end, three-dimensional carrier structures have to provide fine-tuned physical characteristics and specific adhesion sites, the formation of chemokine gradients and the presentation of growth factors. So far, a vast majority of materials applied for that purpose is either based on reconstituted extracellular matrix biopolymers such as collagen I or on common biodegradable polymer (bio)materials such as polylactide. A wealth of technologies has been developed for the advanced processing of these materials.

To extend the resulting options biohybrid polymers – biopolymers covalently linked to synthetic polymers – receive more and more attention: A key feature of this emerging class of polymeric materials concerns the modulation of the specific signalling properties of the incorporated biomolecules. This may even allow for tuning of signal profiles of the bioactive scaffold structures beyond the characteristics of naturally occurring matrices – to switch cells into the ‘regeneration mode’. Another advantage of biohybrid polymers is related to their localized application via injection which is an important prerequisite of *in vivo* tissue engineering strategies. Based on these principles biohybrid polymers may be expected to induce regeneration processes where we are missing them as urgently as in the injured heart muscle after myocardium infarction.

Successful examples of biohybrid polymers include polyethylene glycol (PEG) based networks with enzymatically cleavable peptide units to permit the ingrowth of cells ‘on demand’, i. e. in response to the local cellular activity or PEG-tethered transforming growth factor beta (TGF-*b*) to regulate smooth muscle cell function. Self assembling nanostructures of peptide-amphiphiles define another category of biohybrid materials with particular advantages for *in vivo* tissue engineering strategies.

The rapid progress in genetic engineering and synthesis of biomimetic peptide and carbohydrate structures will broaden the applicability of biohybrid polymers further and foster the merging of the strengths of molecular life science and ‘classical’ polymer science for the rational design bioactive materials. Progress of regenerative therapies is critically dependent on that.

Prof. Dr. Carsten Werner
Member of International Advisory Board

---

[*] Corresponding author, e-mail: werner@ipfdd.de

eXPRESS Polymer Letters Vol.1, No.6 (2007) 334–344
Available online at www.expresspolymlett.com
DOI: 10.3144/expresspolymlett.2007.48

Isothermal crystallization kinetics of poly(ethylene terephthalate) and poly(methyl methacrylate) blends

A. Al-Mulla[*]

Chemical Engineering Department, Kuwait University, P.O. Box 5969, 13060 Safat, Kuwait

Received 25 March 2007; accepted in revised form 4 May 2007

Abstract. Different kinetic models like the Avrami, Tobin and Urbanovici-Segal models have been applied for determining the isothermal crystallization kinetics of virgin poly(ethylene terephthalate) (PET) and PET/poly(methyl methacrylate) (PMMA) blends. The different compositions investigated were PET90/PMMA10, PET75/PMMA25 and PET50/PMMA50 [wt/wt%]. The experimental data was fitted using Solver, a non-linear multi-variable regression program and linearization method. The effect of composition variation of PET/PMMA on parameters like crystallization rate constant and crystallization exponent were investigated. Urbanovici-Segal and Avrami models gave the best fit to the experimental data. Tobin model does not seem to fit the experimental data for the systems under investigation. Experimental results indicated that the crystallization rate constant values increased with decreasing temperatures.

Keywords: *polymer blends and alloys, thermal properties, crystallization kinetics, poly(ethylene terephthalate) (PET), poly(methyl methacrylate) (PMMA)*

1. Introduction

The commercial significance of semi-crystalline PET and amorphous PMMA is well known and confirmed by a large number of producers throughout the world. PMMA is a rigid commodity thermoplastic, while PET is a ductile engineering polymer. The melt rheological properties of PET and impact strength of PMMA can be improved by blending PET and PMMA. Semi-crystalline polymers like PET exhibit both crystalline and amorphous phases. Blending of an amorphous polymer like PMMA with PET can affect its physical and thermal properties. The balance between the crystalline and amorphous components of both polymers in the new blend is a function of the composition and chemistry of both the polymers as well as the processing conditions like cooling rates and thermal histories, used to generate the end product. Regarding the chemistry of the polymers used to form the blend various factors like, polymer chain structure, and average molecular weight can affect the rate of crystallization of the polymer, when cooled from the melt. PET has an ester repeat unit in the backbone while PMMA has the ester repeat unit in the side chain. Therefore, there is no affinity between PET and PMMA because of incompatibility; hence, an exploration of the crystalline state of PET in presence of PMMA is worth studying.

Bishara *et al.* [1] has reported the nonisothermal crystallization kinetics of PET/PMMA blends. In this study the crystallization enthalpy (ΔH) values were found to be dependent on the cooling rate and composition of the blend. Thermogravimetric analysis of PET/PMMA blends were carried out by Al-Mulla *et al.* [2]. TGA analysis revealed that the blends were heterogeneous in nature. Morphological studies of PET/PMMA blends were also reported in the same work. The blends were found

---

[*]Corresponding author, e-mail: adamalmulla@kuc01.kuniv.edu.kw

to exhibit a heterogeneous morphology. PMMA was found to form spherical particles and were seen dispersed in the PET matrix. Dewangan *et al.* [3] developed compatibilized PET/PMMA blends using amphiphilic block copolymers of poly(tert-butyl acrylate) and PMMA. The mechanical and rheological properties of the compatibilized blends have been reported.

The physical and mechanical properties of PET/PMMA blends depend on the blend composition, the physical and chemical interaction between the polymers, morphology of the blends, crystallization rate and extent of crystallization. The mechanical properties of the final product of the blend depend on the crystal structure, morphology and melt history. The time required for the crystallization depends on the nucleation, cooling rate and temperature of melt processing. In order to control the rate of crystallization and the degree of crystallinity and to obtain the desired morphology and properties, efforts have been made to study the crystallization kinetics and determine change in material properties of various polymers [4–9]. Differential scanning calorimeter has been useful in studying the polymer crystallization kinetics [10–11].

A review by Gerard *et al.* [12] deals with the DSC method of analyzing the ability of PET to crystallize. An important conclusion obtained from this work is that the phase changes taking place in PET depend mainly on the thermal history of the sample. This fact has also been supported by Wasiak *et al.* [13]. This paper claims that temperature has an effect on the amount of crystals formed. Although a knowledge of the crystallization kinetics of polymeric materials is important from the aspects of both fundamental and practical applications, only few studies have been carried out on the crystallization behaviour and rheological characterization of PET/PMMA blends.

For studying the isothermal crystallinity a number of mathematical models [14–18] have been proposed. Unlike Avrami model, use of the Tobin [18] and Urbanovici-Segal [19] model to analyze the isothermal crystallization data of semi-crystalline-amorphous polymers is rarely reported in the literature. Literature reports no previous work on the isothermal crystallization kinetic analysis of different compositions of PET/PMMA blends. Therefore, in the present work, all three macro kinetic models are used to analyze the isothermal crystallization data of three different compositions of PET/PMMA blends. The experimental data are fitted to each respective model using a nonlinear and a linear program to obtain the isothermal crystallization parameters. The goodness of the fit (measured using correlation coefficient, r^2) suggests the applicability of the model in describing the isothermal crystallization data of PET/PMMA blends.

2. Experimental

2.1. Materials

PET bottle grade was supplied in pellet form by Century Enka Pvt. Ltd. Pune, India. The intrinsic viscosity of the resin was 0.60 measured at 25°C in a 60/40 (V/V) phenol/tetrachloroethane mixture using a Cannon-Ubbelohde viscometer. Virgin PMMA injection molded in sheet form at an injection pressure of $1.03 \cdot 10^8$ Pa, cylinder temperature, 177 to 210°C and mould temperature of 80°C was used.

2.2. Sample Preparation

PET and PMMA were dried for five hours at 100°C to ensure low moisture levels. PET/PMMA blends were prepared by the melt mixing method in a 500 ml step polymerization reactor. Three different compositions of dried PET and PMMA (PET/PMMA, 50/50, 75/25 and 90/10, weight/weight percent) were made by weighing the accurate quantities. The mixture was melt mixed in the reactor, in a nitrogen atmosphere of 20 ml/min for one hour at 275°C. The stirrer speed was 100 r.p.m. The blended product was removed from the reactor and ground with a Moulinex super blender grater 3 at 400 r.p.m.

2.3. Isothermal crystallization studies

A Mettler-Toledo TA 4000 differential scanning calorimeter (DSC) was used to record the isothermal melt-crystallization exotherms as well as the subsequent melting endotherms for PET, PMMA and their blends. Each sample was used only once and all the runs were carried out in nitrogen atmosphere (20 ml/minute). Calibration of the temperature scale was done with pure indium standard (T_m^0 = 156.6°C and ΔH_f^0 = 28.5 J·g^{-1}) on every sample to ensure accuracy and reliability of the data obtained. Temperature calibration of the DSC instrument was carried out with a standard pan containing indium, lead and zinc whose melting temperature are, 156.6, 327.4 and 419.5°C respectively. Samples (10 mg) were dried completely at 100°C for five hours and then used for the analysis.

In a typical isothermal run, the sample was heated in DSC furnace from 30°C to 280°C at a heating rate of 10°C/min, under a nitrogen atmosphere. It was annealed for 10 minutes at 280°C. The sample was then cooled to the predetermined isothermal temperature (T_c [°C]) at a cooling rate of 100°C/min. The sample was kept at the isothermal temperature till the baseline was attained. Kinetic analysis software available in the Mettler instrument was used to convert the data into Excel files which was later analyzed using, Avrami, Tobin and Urbanovici-Segal models for estimation of the isothermal kinetic parameters of the PET/PMMA blends.

3. Theory

Estimation of isothermal crystallization parameters is normally carried out using the data obtained from crystallization exotherms with a basic assumption that the amount of crystallinity obtained is linearly proportional to the heat released during crystallization. By integrating the heat evolved during crystallization, a relation between relative crystallinity and time can be obtained (Equation (1)).

$$\theta(t) = \frac{\int_0^t \frac{\mathrm{d}H_c}{\mathrm{d}t}\,\mathrm{d}t}{\Delta H_c} \tag{1}$$

were t is the elapsed time and $\mathrm{d}H_c$ is the released heat during crystallization for small time interval $\mathrm{d}t$ and ΔH_c is the total enthalpy of crystallization for a specific crystallization temperature. ΔH_c can be given as Equation (2):

$$\Delta H_c = \int_0^\infty \frac{\mathrm{d}H_c}{\mathrm{d}t}\,\mathrm{d}t \tag{2}$$

The Avrami equation [14] given below (3) is mostly used to determine the time dependent relative crystallinity $\theta(t)$.

$$\theta(t) = 1 - \exp(-k_a t^{n_a}) \tag{3}$$

In Equation (3), k_a is the Avrami rate constant and n_a the Avrami exponent. k_a and n_a are temperature dependent parameters and are specific to a given crystalline morphology and type of nucleation [14]. The Tobin equation [16] is proposed on the basis of kinetic phase transformation and is given as Equation (4):

$$\theta(t) = \frac{k_t t^{n_t}}{1 + k_t t^{n_t}} \tag{4}$$

k_t and n_t are the Tobin rate constant and Tobin exponent respectively. The Tobin exponent, n_t, is governed by different types of nucleation and growth mechanisms [16].

Urbanovici and Segal [19] developed a new kinetic equation, which is a modification of the Avrami model. The relationship between the time-dependent relative crystallinity function $\theta(t)$ and the crystallization time given by Urbanovici-Segal model is as shown in Equation (5):

$$\theta(t) = 1 - [1 + (r-1)k_{us} t^{n_{us}}]^{\frac{1}{1-r}} \tag{5}$$

In this equation, k_{us} and n_{us} are the Urbanovici-Segal crystallization rate constant and exponent, respectively. k_{us} has the unit of (time)$^{-1}$. r is an optimization parameter which determines the extent of deviation for the Urbanovici-Segal equation from the Avrami equation. When r approaches 1, the Urbanovici-Segal equation becomes similar to the Avrami equation [20].

Kinetic analysis of virgin PET, and PET/PMMA blends were carried out using Equations (3), (4) and (5).

The objective was to obtain the isothermal crystallization rate constant and the crystallization exponent respectively. Two different analysis methods were used. One of the procedures used Solver, a nonlinear optimization function found in Excel. In the other approach Equations (3) and (4) were linearized and applied to the experimental data to obtain the isothermal kinetic parameters.

The goodness of the methods were confirmed using correlation coefficient (r^2). The greater the convergence of r^2 towards 1 the better is the quality of the fit.

The linearized logarithmic form of Equations (3) and (4) is represented as Equations (6) and (7):

$$\ln[-\ln(1-\theta(t))] = n\ln(t) + \ln k \tag{6}$$

$$\ln\left(\frac{-\theta}{\theta-1}\right)=\ln k+n\ln t \tag{7}$$

Plotting the first term in Equation (6) *versus* log$t$ one can obtain k and n from the slope and intercept respectively. Similarly on plotting the first term in Equation (7) as a function of ln$t$ the kinetic constants k and n can be determined.

3.1. Isothermal crystallization kinetics of virgin PET and PET/PMMA blends

Typical isothermal melt crystallization exotherms for PET90/PMMA10 [wt/wt%] after isothermal crystallization at crystallization temperatures ranging from 207 to 221°C are shown in Figure 1. Other blends also showed similar crystallization behaviours. After thermal stabilization, the heat flow signal, on crystallization exhibited an exotherm, a result of the thermal energy released due to crystallization. The onset and endset of crystallization is determined by drawing a tangent to the respective baselines.

Figures 2 and 3 are typical figures illustrating the sigmoidal behaviour of virgin PET and the blend of PET90/PMMA10 [wt/wt%]. As seen in Figures 2 and 3 the time needed to reach 100% relative crystallinity increased with increasing crystallization temperature, T_c. $t_{0.5}$ is an important parameter which can be obtained from the plot of relative crystallinity and time. $t_{0.5}$ is defined as the time needed to attain 50% crystallinity. Table 1 summarizes the values of crystallization half-time ($t_{0.5}$) using the Equation (8).

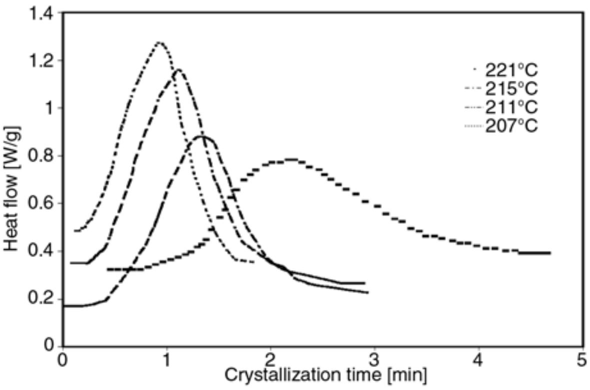

Figure 1. Isothermal melt crystallization exotherms for PET 90/PMMA10 observed at different crystallization temperatures

$$t_{0.5}=\left(\frac{\ln 2}{k}\right)^{\frac{1}{n}} \tag{8}$$

The $t_{0.5}$ values shown in Table 1 are found to decrease with decreasing crystallization temperature, T_c. Figure 4 indicates a plot of $t_{0.5}$ *versus* crystallization temperature, T_c. The $t_{0.5}$ values are found to decrease as the PET composition decreases in the blends. PET virgin has the maximum $t_{0.5}$ value.

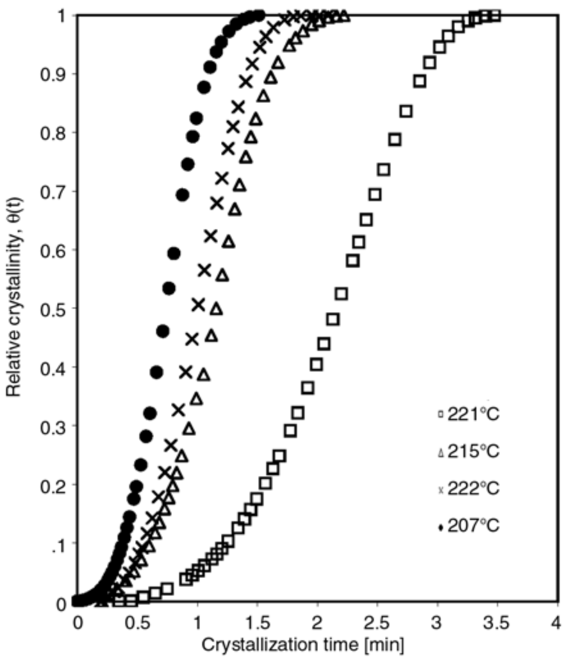

Figure 2. Relative crystallinity as a function of time of virgin PET

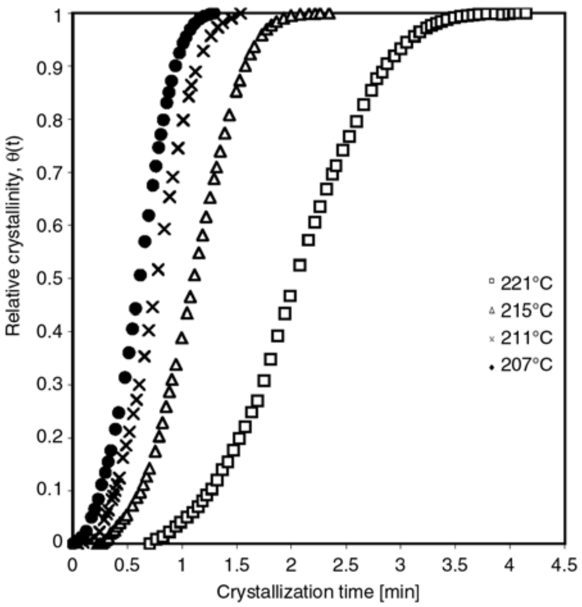

Figure 3. Relative crystallinity as a function of time of PET 90/PMMA10 [wt/wt%]

Table 1. Summary of isothermal crystallization parameters for virgin PET and its blends using Avrami model

	T_c [°C]	Isothermal kinetic constants based on Solver method					Isothermal kinetic constants based on linearization method				
		k_a [min^{-1}]	n_a	Average n_a	r^2	$t_{0.5}$ [min]	k_a [min^{-1}]	n_a	Average n_a	r^2	$t_{0.5}$ [min]
VIRGIN PET	221	0.04	3.78	3.33	1.00	2.14	0.04	3.78	3.33	1.00	2.14
	215	0.45	3.30		1.00	1.14	0.45	3.30		1.00	1.14
	211	0.70	3.30		1.00	1.00	0.70	3.30		1.00	1.00
	207	1.74	2.97		1.00	0.73	1.74	2.97		1.00	0.73
PET90/PMMA10	221	0.05	3.71	3.09	1.00	2.06	0.05	3.71	3.09	1.00	2.06
	215	0.50	3.31		1.00	1.10	0.50	3.31		1.00	1.10
	211	1.51	2.81		1.00	0.76	1.51	2.81		1.00	0.76
	207	2.55	2.55		1.00	0.60	2.55	2.55		1.00	0.60
PET75/PMMA25	221	0.44	4.36	3.80	1.00	1.11	0.44	4.35	3.80	1.00	1.11
	215	6.67	4.31		1.00	0.59	6.67	4.30		1.00	0.59
	211	8.81	3.58		1.00	0.49	8.81	3.58		1.00	0.49
	207	12.43	2.96		1.00	0.38	9.51	2.96		1.00	0.41
PET50/PMMA50	221	5.35	4.28	3.71	1.00	0.62	3.42	3.76	3.60	0.91	0.65
	215	11.99	3.79		1.00	0.47	11.97	3.79		1.00	0.47
	211	22.77	3.73		1.00	0.39	22.77	3.73		1.00	0.39
	207	21.68	3.04		1.00	0.32	21.68	3.04		1.00	0.32

T_c – crystallization temperature [°C]

According to Figure 4 it is obvious that for virgin PET and the polymer blends the crystallization half time increases with crystallization temperature. The analysis of half time of crystallization demonstrates that increasing concentration of PMMA in the blends lead to some kind of deceleration of the PET crystallization. This behaviour could be possibly caused by the decreasing segmental mobility of the PET chains in the presence of increasing amounts of PMMA.

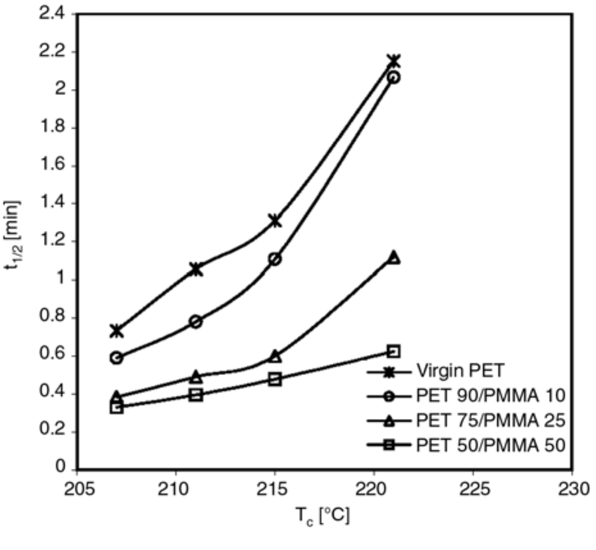

Figure 4. $t_{1/2}$ as a function of isothermal crystallization temperature for virgin PET and its blends

3.2. Application of the Solver method to determine the isothermal crystallization parameters for PET/PMMA blends using the Avrami and Tobin models

The Avrami Equation (3) was applied to the experimental data of virgin PET and PET/PMMA blends. Solver, a non-linear optimization method was used to obtain the isothermal crystallization parameters, k_a and n_a shown in Table 1. Figure 5 is a typical plot of relative crystallinity as a function of time for PET75/PMMA25 [wt/wt%] blend fitted using the Avrami model. The Avrami model is found to fit the data well at 207, 211 and 215°C

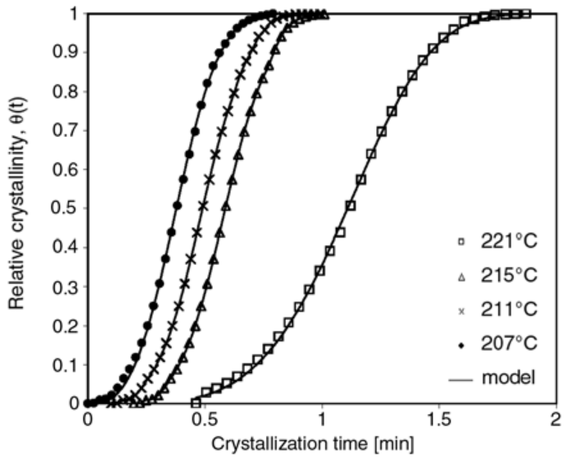

Figure 5. Plot of relative crystallinity as a function of time for PET 75/PMMA25 [wt/wt%] using Avrami model

while at 221°C the fitting is found to deviate slightly at the beginning and later stages of the conversion. The average value of the Avrami exponent for virgin PET and PET/PMMA blends is found to range from 3.09 to 3.80. n_a is found to be temperature dependent and is found to increase with increasing, T_c.

The isothermal rate constant values in Table 1 exhibits sensitivity to change with crystallization temperature. It increases with decreasing crystallization temperature. This could plausibly be due to the fact that the concentration of the crystallizable material (PET) decreases in the blend. The k_a values for PET50/PMMA50 are the highest compared to the other blends. This trend for PET50/PMMA50 could not be explained. A qualitative observation of Table 1 reveals that the k_a values vary from 0.04 to 22.77 min^{-1}.

The Tobin model (Equation (4)) was applied to the experimental data to obtain the Tobin's isothermal kinetic parameters, k_t and n_t. Figure 6 is a typical figure indicating the application of Tobin model using the Solver method. Table 2 summarizes the Tobin kinetic parameters along with the correlation coefficient (r^2) values obtained as a result of the best fit. According to Table 2 the Tobin exponent is found to range from 3.88 to 6.56. The Tobin exponents are found to be greater than Avrami exponents. The r^2 values obtained using Tobin equation are lower than the Avrami equation which indicates that Tobin model has a poor fit compared to Avrami model.

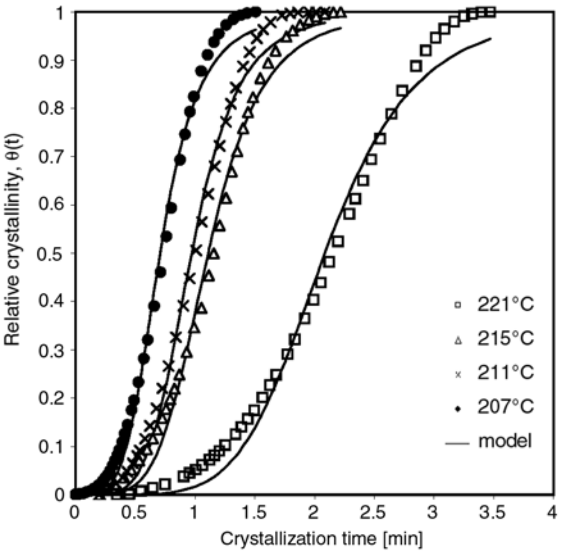

Figure 6. Plot of relative crystallinity as a function of time for virgin PET

Figure 7 is a typical plot showing the application of Equation (6) to PET75/PMMA25 data. The r^2 values and the kinetic constants obtained on fitting Equation (6) to the experimental data are given in Table 1. The r^2 values are 1 indicating that the fit is 100% perfect. The crystallization exponent is found to decrease with decreasing temperature. The average exponent values are found to lie in the range of 3.09 to 3.80. The isothermal rate constants are found to increase with decreasing crystallization

Table 2. Summary of isothermal crystallization parameters for virgin PET and its blends using Tobin model

		Isothermal kinetic constants based on Solver method			**Isothermal kinetic constants based on linearization method**		
	T_c [°C]	**k_t [min^{-1}]**	**n_t**	**r^2**	**k_t [min^{-1}]**	**n_t**	**r^2**
VIRGIN PET	221	0.02	5.53	0.99	0.02	4.89	0.97
	215	0.60	4.87	1.00	0.51	4.53	0.97
	211	1.15	4.93	1.00	0.91	4.52	0.96
	207	4.45	4.33	1.00	2.45	3.93	0.98
PET90/PMMA10	221	0.02	5.62	1.00	0.03	3.98	0.93
	215	0.70	4.92	1.00	0.36	3.98	0.97
	211	3.53	4.07	0.99	2.48	3.78	0.97
	207	8.11	3.88	1.00	5.29	3.59	0.97
PET75/PMMA25	221	0.58	6.56	1.00	0.58	6.56	1.00
	215	34.55	6.48	1.00	34.47	6.48	1.00
	211	56.32	5.50	1.00	33.78	5.10	0.96
	207	95.39	4.55	1.00	95.39	4.55	1.00
PET50/PMMA50	221	79.46	5.65	1.00	13.76	5.76	0.95
	215	80.04	5.51	1.00	70.81	4.90	0.97
	211	199.39	5.53	1.00	28.08	4.85	0.95
	207	198.13	4.56	1.00	89.03	4.23	0.98

T_c – crystallization temperature [°C]

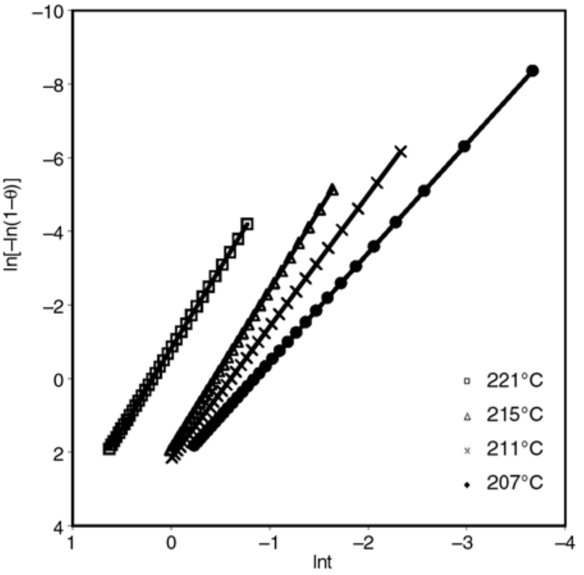

Figure 7. Plot of ln[–ln(1–θ)] as a function of logarithmic time for PET 75/PMMA25 [wt/wt%] using Avrami Model

temperatures. The highest value of rate constant is found to be for virgin PET at 211°C and is approximately 22.77 min^{-1}.

Figure 8 is a typical plot showing the application of Equation (7) to virgin PET. The correlation coefficient values and the kinetic constants obtained on fitting Equation (7) to the experimental data is given in Table 2. The isothermal exponent for crystallization is found to range between 3.59 to 6.60. The highest exponent values are found for PET75/PMMA25. The isothermal rate constants are found to increase with decreasing crystallization temperatures. The rate constant values are found to lie between 0.02 to 95.39 min^{-1}. Since the values of r^2 for the Tobin model lies between 0.93 to 1 the kinetic parameters obtained using this method is questionable.

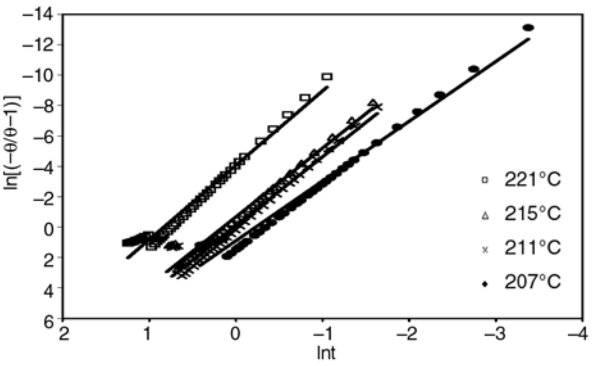

Figure 8. Plot of ln[–θ/(θ–1)] as a function of logarithmic time for PET virgin using Tobin model

3.3. Isothermal crystallization kinetics of virgin PET and PET/PMMA blends based on the Urbanovici-Segal analysis

The analysis based on Urbanovici-Segal model is done by fitting Equation (5) to the θ(t) obtained for each crystallization temperature. The Urbanovici-Segal kinetic parameters (i. e., n_{us}, k_{us} and r_{us}) and the r^2 values are summarized in Table 3. The r^2 values for the fit are found to be approximately 1.00. Figure 9 is a typical plot of relative crystallinity as a function of time for virgin PET based on Urbanovici-Segal model. The average value of the exponent (n_{us}) for isothermal crystallization is

Table 3. Summary of isothermal crystallization parameters for virgin PET and its blends using Urbanovici-Segal model

	T_c [°C]	r_{us}	k_{us} [min^{-1}]	n_{us}	Average n_{us}	r^2	$t_{0.5}$ [min]
VIRGIN PET	221	0.75	0.41	3.60	3.30	1.00	2.15
	215	0.80	0.67	3.35		1.00	1.31
	211	0.86	0.83	3.16		1.00	1.06
	207	1.01	1.21	3.05		1.00	0.73
PET90/PMMA10	221	0.91	0.43	3.38	2.76	1.00	2.07
	215	0.75	0.77	2.85		1.00	1.11
	211	0.70	1.06	2.47		1.00	0.78
	207	0.91	1.43	2.34		1.00	0.59
PET75/PMMA25	221	0.81	0.80	3.92	3.52	1.00	1.12
	215	0.89	1.50	3.85		1.00	0.60
	211	1.10	1.87	3.74		1.00	0.49
	207	0.76	2.19	2.58		1.00	0.38
PET50/PMMA50	221	0.78	1.43	3.87	3.25	1.00	0.62
	215	0.67	1.80	3.20		1.00	0.48
	211	0.73	2.20	3.30		1.00	0.40
	207	0.68	2.53	2.65		1.00	0.33

T_c – crystallization temperature [°C]

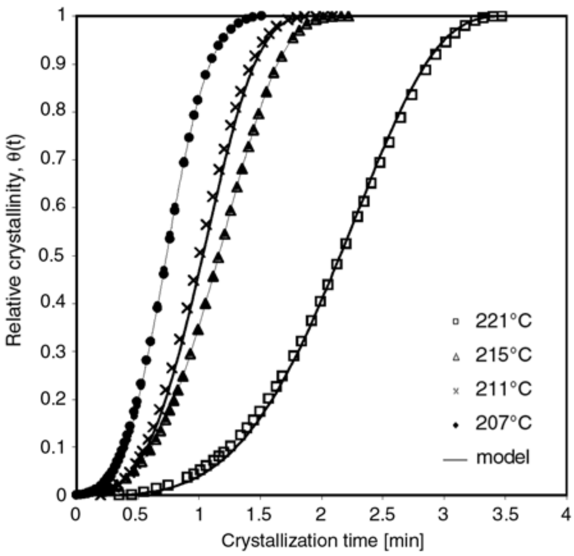

Figure 9. Relative crystallinity as a function of time for virgin PET using Urbanovici-Segal model

found to vary from 2.76 to 3.52. This may correspond to spherulitic growth [20].

The Urbanovici-Segal rate constant, k_{us} increases with decreasing crystallization temperature. This trend is similar to that indicated by Avrami and Tobin models.

r in Urbanovici-Segal model is the parameter which fine tunes the fit of the model to the experimental data. This could be the reason why the Urbanovici-Segal model provides a better fit to the data. k_a values (Table 1) are generally found to be higher than k_{us} values (Table 3) especially for PET/PMMA blends.

The n_a and n_{us} values obtained using the Avrami and Urbanovici-Segal model are in general found to be comparable. Based on the r^2 values and the physical observation of the plots Urbanovici-Segal model is found to be a good model for describing the isothermal crystallization kinetics of virgin PET and PET/PMMA blends.

The equation used to calculate the $t_{0.5}$ values for the Urbanovici-Segal model is given in Equation (9):

$$t_{0.5} = \left(\frac{0.5^{(1-r)}-1}{r-1}\right)\frac{1}{k_{us}} \tag{9}$$

where k_{us} and r have the same significance as indicated in Equation (5). The $t_{0.5}$ values have a similar trend to that of Avrami model.

The values obtained using Equation (9) are given in Table 3.

3.4. Overall comparison between Avrami, Tobin and Urbanovici-Segal using the Solver and linearization method

The efficacy of each kinetic equation in describing the experimental data is represented by the r^2 value. The closer the r^2 value to 1 the better is the quality of the fit. Physical observation of the plots and the r^2 values indicate that Urbanovici-Segal and Avrami method using Solver is a good multivariable regression program to fit the experimental data to the aforementioned models. Figure 6 and the r^2 values in Table 2 clearly show the deviation of the Tobin model from the experimental data. The Tobin model appears to mismatch the data for the complete experimental range. A typical example for the comparison between the three models is shown in Figure 10. If a comparison is made between Avrami and Urbanovici-Segal models a conclusion can be arrived that the Arvami model over-estimates the θ(t) in the middle stage (Figure 10) and underestimates it at the early and later stages of the crystallization.

No similarity exists between the isothermal kinetic constants estimated using the Solver and linearization method for the Avrami and the Tobin model. The Avrami exponent values are lower compared to the Tobin values. The conclusion which can be drawn based on the r^2 value is that Avrami and Urbanovici-Segal equation are good models to predict the isothermal kinetic constants for the

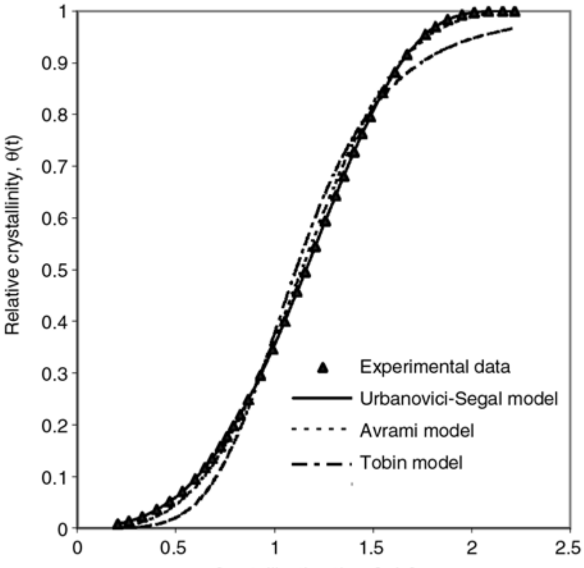

Figure 10. Modeling of virgin PET data using three different models at 215°C

PET/PMMA systems using both the Solver and linearization methods.

Identical crystallization rate constant values are obtained using Avrami model when the Solver and linearization methods were applied to the data obtained for the blends and virgin PET. To further substantiate the observation the rate constant and exponent values obtained using Tobin model were plugged into the respective equations and replotted against the relative crystallinity data of PET90/PMMA10. A typical plot depicting the compliance of the two different methods is indicated in Figure 11. As seen from the figure the Solver method seems to be more adaptable to determine the crystallization kinetic parameters of the system under investigation.

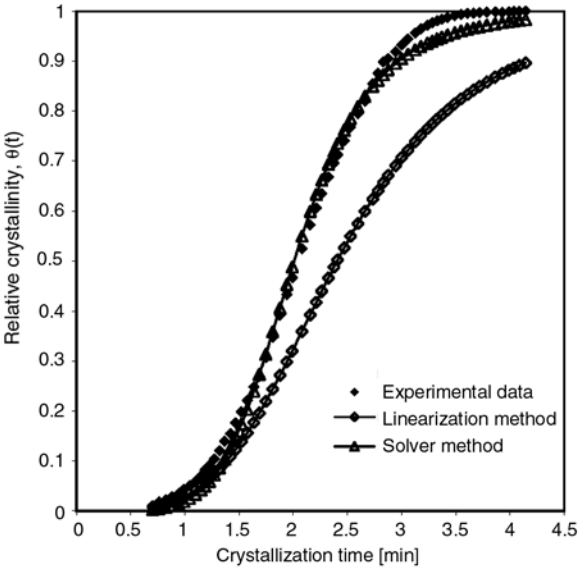

Figure 11. Comparison of the experimental data with Tobin model for PET 90/PMMA10 at 221°C using kinetic constants generated through Solver and linear fitting method

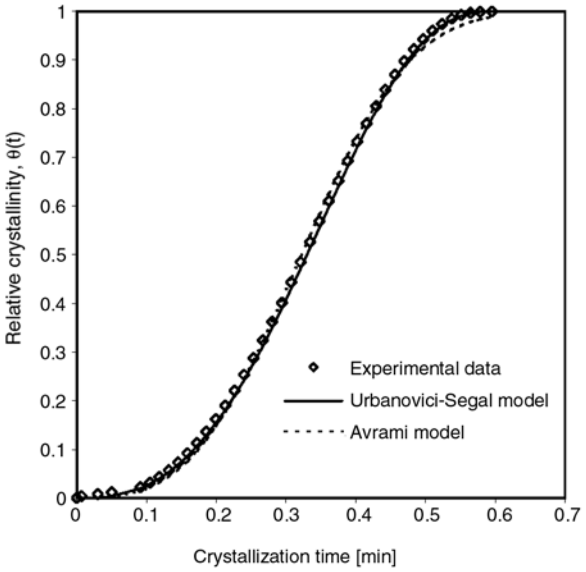

Figure 12. Comparison of the experimental data with Avrami and Urbanovici-Segal models for PET 50/PMMA50 at 207°C using kinetic constants generated through Solver

Figure 12 is a plot showing the compliance of Urbanovici-Segal model to a typical blend, (PET50/PMMA50), using the Solver method. The figure clearly indicates that the error between the experimental data and Urbanovici-Segal model is less compared to the Avrami model.

3.5. Temperature-dependence of the kinetic parameters

The Avrami parameter n_a depends on the crystallization temperature and the shape of the crystals being grown. The Avrami parameter, n_a, of virgin PET and PET/PMMA blends show fractional values (Tables 1 and 3). Such types of values are theoretically accounted in the general statistical Avrami theory of crystallization [21]. The Avrami theory supposes a partial overlapping of primary nucleation and crystal growth. In the case of diffusion controlled growth or other constraints on crystallization, fractional values could be found [21]. As seen in Tables 1 and 3 the isothermal crystallization exponent increases slightly with increasing temperature, plausibly indicating that diffusion controlled process might not be controlling the crystallization

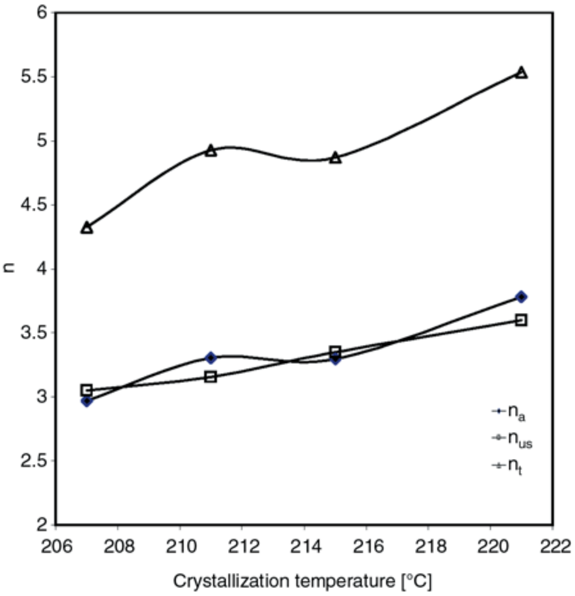

Figure 13. Crystallization exponent (n) obtained for different models as a function of crystallization temperature for virgin PET

mechanism in the present work [22]. Variation of n_a, n_t and n_{us} as a function of crystallization temperature is shown in Figure 13.

Tables 1 and 3 lists the average isothermal crystallization exponents obtained for the virgin polymers and the blends. The average isothermal crystallization exponent for PET is found to be approximately 3.33 for an isothermal temperature range of 207–221°C.

Xanthos *et al.* [23] and Kim and Kim [24] reported an average value of PET to be around 2.35 and 2.37 respectively. They report that the Avrami parameter n_a depends on the crystallization temperature and the shape of the crystals being grown. Literature cites different values of n_a for different polymeric systems. Even for a similar system different values of n_a have been reported. For example poly(3-hydroxy butyrate) (PHB) and its blends have an n_a of approximately 2 as reported by Dubini *et al.* [25]. Mansour *et al.* [26] reported the value of n close to 4. An *et al.* [27] observed the value of n to be 4 for PHB and n equal to 3 for PHB/polyvinyl alcohol blends.

When the temperature is low crystallization rate is controlled by diffusion of molecules at the crystal growth front (diffusion control); where as at temperatures closer to the melt temperature, as used in this study the rate limiting step of the crystallization process is the nucleation rate (nucleation control).

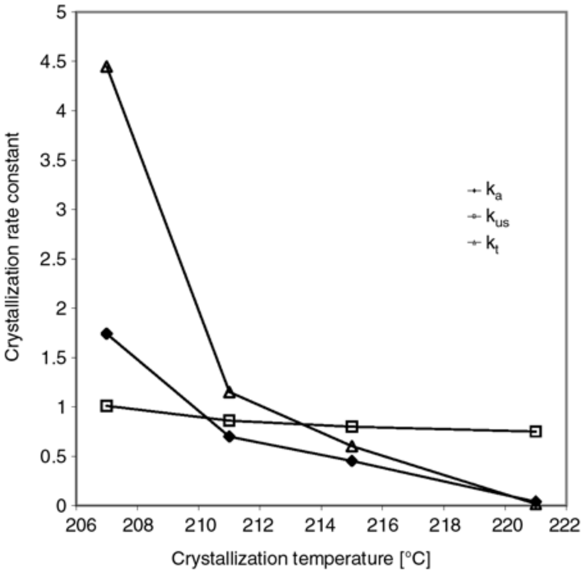

Figure 14. Crystallization rate constant obtained for different models as a function of crystallization temperature for virgin PET

Figure 14, illustrates the temperature-dependence of all the crystallization rate parameters (i. e., k_a, k_t and k_{us}). It is seen that the crystallization rate parameters exhibit temperature-dependence. It is worth noting that all the rate parameters have dimensions of min^{-1} and follow a defined pattern with increasing crystallization temperature.

4. Conclusions

The isothermal crystallization kinetics of virgin PET and PET/PMMA blends has been examined using DSC at crystallization temperatures ranging between 207 to 221°C. Avrami, Tobin and Urbanovici-Segal models were used to determine the isothermal crystallization parameters for virgin PET and PET/PMMA blends using the Solver and linearization method. r^2 value was used to determine the goodness of the model. The crystallization exotherms followed the Avrami and the Urbanovici-Segal model with exponents ranging between 3.09 to 3.80. The crystallization rate constants for the Avrami and Urbanovici-Segal model ranged between 0.04 to 22.77 and 0.41 to 2.53 min^{-1}. The crystallization rate parameters (k_a and k_{us}) determined on the basis of different macrokinetic models exhibit temperature dependence. Within the crystallization temperature range studied (i. e., 207 to 221°C) the values of the rate parameters were all found to increase with decreasing temperature for the PET/PMMA blends and virgin PET.

Acknowledgements

The author would like to thank Dr. Johnson Mathew and Bader Masiar for their professional help during the course of this work. The author would also like to thank the Research Administration of Kuwait University for providing funds from project EC 02/05 for carrying out this work.

References

[1] Bishara A., Shaban H. I.: Nonisothermal crystallization kinetics of poly(ethylene terephthalate) and poly(methyl methacrylate) blends. Journal of Applied Polymer Science, **101**, 3565–3571 (2006).

[2] Al-Mulla A., Shaban H.: Degradation kinetics of poly(ethylene terephthalate) and poly(methyl methacrylate) blends. Polymer Bulletin, **58**, 893–902 (2007).

[3] Dewangan B., Jagtap R. N.: Amphiphilic block copolymers of PtBA-b-PMMA as compatibilizers for blends of PET and PMMA. Polymer Engineering and Science, **46**, 1147–1152 (2006).

[4] Jabarin S. A.: Crystallization kinetics of polyethylene terephthalate. II. Dynamic crystallization of PET. Journal of Applied Polymer Science, **34**, 97–102 (1987).

[5] Gümther B., Zachmann H. G.: Influence of molar mass and catalysts on the kinetics of crystallization and on the orientation of poly(ethylene terephthalate). Polymer, **24**, 1008–1014 (1983).

[6] Mehta A., Gaur U., Wunderlich B.: Equilibrium melting parameters of poly(ethylene terephthalate). Journal of Polymer Science Part B: Polymer Physics, **16**, 289–296 (1978).

[7] Ozawa T.: Kinetics of non-isothermal crystallization. Polymer, **12**, 150–158 (1971).

[8] Misra A., Stein R. S.: Light scattering studies of the early stages of the crystallization of poly(ethylene terephthalate). Journal of Polymer Science Part B: Polymer Letters, **10**, 473–477 (1972).

[9] Stein R. S., Misra A.: Kinetics of growth of developing spherulites. Journal of Polymer Science Part B: Polymer Physics, **11**, 109–116 (1973).

[10] Booth A., Hay J. N.: The use of differential scanning calorimetry to study polymer crystallization kinetics. Polymer, **10**, 95–104 (1969).

[11] Hay J. N., Mills P. J.: The use of differential scanning calorimetry to study polymer crystallization kinetics. Polymer, **23**, 1380–1384 (1982).

[12] Gerard D., Garda M-R., Saiter J-M.: Experimental protocol to determine the ability of PET to crystallize. Journal of Thermal Analysis, **7**, 155–160 (2003).

[13] Wasiak A., Sajkiewicz P., Wozniak A.: Effect of cooling rate on crystallinity of i-propylene and polyethylene terephthalate crystallized in non-isothermal conditions. Journal of Polymer Science Part B: Polymer Physics, **37**, 2821–2827 (1999).

[14] Avrami M.: Kinetics of Phase Change. I General Theory. Journal of Chemical Physics, **7**, 1103–1112 (1939).

[15] Evans U. R.: The laws of expending circles and spheres in relation to the lateral growth of surface films and the grain-size of metals. Transactions of the Faraday Society, **41**, 365–374 (1945).

[16] Tobin M. C.: Theory of phase transition kinetics with growth site impingement. I. Homogeneous nucleation. Journal of Polymer Science Part B: Polymer Physics, **12**, 399–406 (1974).

[17] Malkin Y. A., Beghishev V. P., Keapin I. A., Bolgov S. A.: General treatment of polymer crystallization kinetics – Part 1. A new macrokinetic equation and its experimental verification. Polymer Engineering and Science, **24**, 1396–1401 (1984).

[18] Tobin M. C.: Theory of phase transition kinetics with growth site impingement. III. Mixed heterogeneous-homogeneous nucleation and nonintegral exponents of the time. Journal of Polymer Science Part B: Polymer Physics, **15**, 2269–2270 (1977).

[19] Urbanovici E., Segal E.: New formal relationships to describe the kinetics of crystallization. Thermochimica Acta, **171**, 87–94 (1990).

[20] Supahol P., Simoaon P., Sirivat A.: Effect of crystalline and orientational memory phenomena on the isothermal bulk crystallization and subsequent melting behavior of poly(trimethylene terephthalate). Polymer International, **53**, 1118–1126 (2004).

[21] Mandelkern L.: Crystallization of Polymers. McGraw-Hill, New York (1994).

[22] Arroyo M., Lopez-Manchado M. A. Avalos F.: Crystallization kinetics of polypropylene: II. Effect of the addition of short glass fibers. Polymer, **38**, 5587–5593 (1997).

[23] Xanthos M., Baltzis B. C., Hsu P. P: Effects of carbonate salts on crystallization kinetics and properties of recycled poly(ethylene terephthalate). Journal of Applied Polymer Science, **64**, 1423–1435 (1997).

[24] Kim S. P, Kim S. C.: Crystallization kinetics of poly(ethylene terephthalate): memory effect of shear history. Polymer Engineering and Science, **33**, 83–91 (1993).

[25] Dubini E., Beltrame M., Conetti A., Saves B., Martuscelli E.: Crystallization and thermal behaviour of poly (**D**(–) 3-hydroxybutyrate)/poly(epichlorohydrin) blends. Polymer, **34**, 996–1001 (1993).

[26] Mansour A. A., Saad G. R., Hamed A. M.: II. Dielectric investigation of cold crystallization of poly(3-hydroxybutyrate) and poly(3-hydroxybutyrate-co-3-hydroxyvalerate). Polymer, **40**, 5377–5391 (1999).

[27] An Y., Li L., Dong L., Mo Z., Feng Z.: Nonisothermal crystallization and melting behavior of poly(β-hydroxybutyrate)-Poly(vinyl-acetate) blends. Journal of Polymer Science Part B: Polymer Physics, **37**, 443–450 (1999).

eXPRESS Polymer Letters Vol.1, No.6 (2007) 345–355
Available online at www.expresspolymlett.com
DOI: 10.3144/expresspolymlett.2007.49

Morphology and contact angle studies of poly(styrene-co-acrylonitrile) modified epoxy resin blends and their glass fibre reinforced composites

N. Hameed[1]*, S. P. Thomas*[1]*, R. Abraham*[2]*, S. Thomas*[1]*

[1]School of Chemical Sciences, Mahatma Gandhi University, P. D. Hills, Kottayam, 686 560, India
[2]Department of Physics, St. Dominic's College, Kanjirappilly, Kottayam, Kerala, India

Received 1 April 2007; accepted in revised form 4 May 2007

Abstract. In this study, the surface characteristics of blends and composites of epoxy resin were investigated. Poly(styrene-co-acylonitrile) (SAN) was used to modify diglycidyl ether of bisphenol-A (DGEBA) type epoxy resin cured with diamino diphenyl sulfone (DDS) and the modified epoxy resin was used as the matrix for fibre reinforced composites (FRP's). E-glass fibre was used as the fibre reinforcement. The scanning electron micrographs of the fractured surfaces of the blends and composites were analyzed. Morphological analysis revealed different morphologies such as dispersed, cocontinuous and phase-inverted structures for the blends. Contact angle studies were carried out using water and methylene iodide at room temperature. The solid surface energy was calculated using harmonic mean equations. Blending of epoxy resin increases its contact angle. The surface free energy, work of adhesion, interfacial free energy, spreading coefficient and Girifalco-Good's interaction parameter were changed significantly in the case of blends and composites. The incorporation of thermoplastic and glass fibre reduces the wetting and hydrophilicity of epoxy resin.

Keywords: *thermosetting resins, polymer composites, morphology, contact angle, wettability*

1. Introduction

Among the thermosetting polymers, epoxy resins are the most widely used for high performance applications such as, matrices for fibre reinforced composites, coatings, structural adhesives and other engineering applications [1]. Many studies have been made to improve their toughness and crack resistance. In recent years, high performance thermoplastics have been extensively used to toughen thermosetting resins because of their high modulus and glass transition temperatures [2–4]. Morphology of the resulting polymer blends depends on the selection of the thermoplastic polymer, the epoxy precursors, hardener and on the curing cycle parameters [5–7]. The phase separation upon crosslinking is due to the increase in molecular weight of epoxy resin. This reaction induced phase separation (RIPS) leads to different morphologies. Dispersed, cocontinuous or phase-inverted structures can be obtained. Thermosets have historically been the principal matrix material for fibre reinforced composites for many applications [8–10].

A great deal of research interest has been made on the study of the wetting phenomena of polymeric systems [11–13]. An appropriate experimental technique for quantifying the surface properties of solids is the measurement of contact angles of liquids on solid surfaces. The term wettability is used to describe the extent to which a liquid spreads on a solid surface. The interfacial properties between a liquid and a polymer component are characterized

---

*Corresponding author, e-mail: sabut@sancharnet.in

by the surface energies of each phase and the contact angle between them. The contact angle method is relatively simple, very useful and highly sensitive to investigate the interfacial phenomena. The contact angle is an important parameter in surface science. It is the angle between the surface of the wetted solid and a line tangent to the curved surface of the drop at the point of three-phase contact.

In this paper, systematical experimental studies on the morphological and wetting behaviour of epoxy resin (DGEBA) modified with SAN (Styrene Acrylonitrile) and then reinforced with glass fibres were made. The phase separation in blends and arrangement of fibres in composites were investigated. The hydrophilic/hydrophobic nature of the specimens was well established. The study is aimed to reduce the hydrophilic nature of epoxy resin by thermoplastic modification. The study is also directed to the effect of thermoplastic/fibre content on the surface properties of blends and composites.

2. Experimental

2.1. Materials used

Commercially available diglycidyl ether of bisphenol-A (DGEBA) epoxy resin (L-12, Atul Ltd., India) with an epoxide equivalent of 180–200 was used. The curing agent used was 4,4’-diaminodiphenyl sulfone (DDS, Atul Ltd., India). The thermoplastic modifier used was poly(styrene-co-acrylonitriole) (SAN-A, Bayer, Germany) with 25% of acrylonitrile (AN) content. The reinforcement (chopped E-glass fibre mat) was supplied by Ceat Ltd., India. The density of glass fibre is 2.51 g/cm^3. The chemical structures of epoxy resin and DDS are given in Figure 1. The composition of E-glass fibre is given in Table 1.

Table 1. Composition of E-glass fibre

Glass fibre type	SiO_2	Al_2O_3	CaO	MgO	B_2O_3	Na_2O
E-glass	54.5	14.5	17	4.5	8.5	0.5

2.2. Blend preparation

Melt-mixing technique was adopted for the preparation of blends. SAN was first dissolved in epoxy resin at 180°C with constant stirring in a magnetic stirrer. After getting a homogeneous solution, stoichiometric amount of DDS was added and dissolved completely without changing the temperature. The resulting solution was poured in to an open mould. The blend was cured at 180°C for 3 hours and then post cured at 200°C for 2 hours in an oven. After curing, blends were allowed to cool slowly to room temperature. Blends with 5, 10, 15 and 20 phr SAN were prepared.

2.3. Composite preparation

Fibre reinforced composites were fabricated using the compression moulding technique. Glass fibre mat was cut to size and heated in an oven at 150°C to make it moisture free before processing. 10 phr blend was used as the matrix for composites. The SAN modified epoxy resin and hardener mixture, before curing, was applied to the pre-weighed glass fibre sheets. Eight layers were added successively in order to get 3 mm thickness for the composites. The laminates were compressed in a mould. It is then cured at 180°C for 3 hours and then post cured at 200°C for 2 hours. The laminates were allowed to cool slowly to room temperature. Four different compositions were prepared, where the resin-fibre volume ratio are 70:30, 60:40, 50:50 and 40:60 respectively. The composites were also prepared using neat epoxy as the matrix for comparison.

Blends were designated as ES5, ES10, ES15 and ES20, where E and S correspond to epoxy resin and

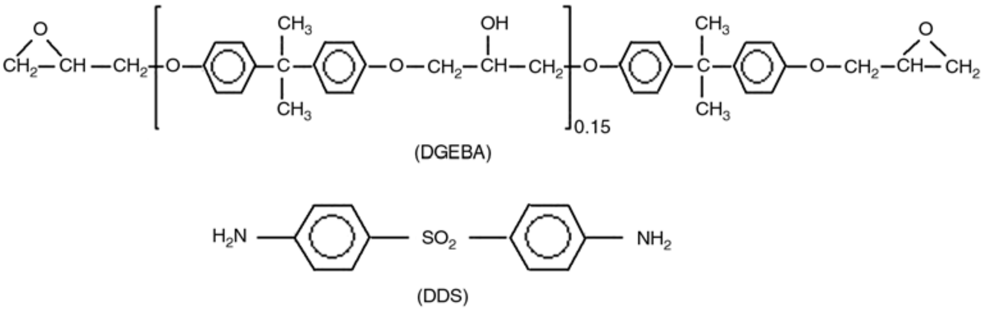

Figure 1. Chemical structures of epoxy resin and DDS

SAN respectively and the numbers 5, 10, 15 and 20 represent the wt% of SAN (in phr). The composites were designated as EG30, EG40, EG50, EG60, ESG30, ESG40, ESG50 and ESG60 where the numbers represent the fibre volume from 30 to 60% and G represents the glass fibre.

3. Characterization

3.1. Scanning electron microscopy

The morphology of the blends and composites was examined using scanning electron microscopy (SEM). The SEM micrographs of failed specimens were analyzed with a Zeiss FESEM Supra 25 scanning electron microscope.

3.2. Contact angle

Contact angle measurements of the blends and composites were conducted in a FTA 100 series (First Ten Angstroms, Portsmouth, Virginia 23704, USA). Water (distilled many times) and methylene iodide (Kemphasol, Bombay) were used for the analyses of samples. Measurements were carried out on samples of dimension 6×2×0.3 cm^3 at room temperature in closed chambers. The volume of the sessile drop was maintained as 5 µl in all cases using a microsyringe. For accuracy, measurements were repeated 5–10 times on different pieces of the same sample.

4. Theory and calculations

When a liquid drop is brought onto the surface of a solid, the contact of liquid/solid reaches an equilibrium condition and we say the liquid drop is in a static state. Whether it will wet the surface or not depends on the relative magnitudes of the molecular forces that exist within the liquid (cohesive) and between the liquid and the solid (adhesive). The angle with which the liquid subtends the solid is known as the contact angle (θ) as shown in Figure 2. Such a contact angle is used to characterize the wettability of a liquid on a solid surface. Because the contact angle ranges from 0 to 180°, there are two extreme cases. If the contact angle is equal to 0°, i. e., a liquid film is formed on a solid surface, then we can say that a perfect wetting occurs. The other case is that the contact angle is equal to 180°, i. e., a perfect liquid sphere is set on the solid surface. In this case, the contact angle is related to the characteristic surface energies of different interfaces among the liquid used and solid surfaces.

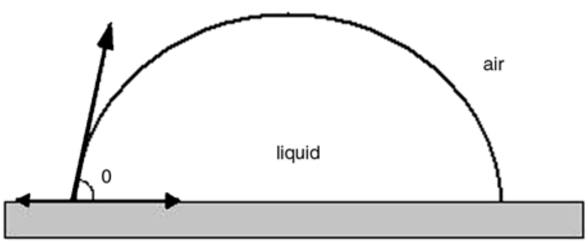

Figure 2. Sessile drop spread wetting

It is well established from the literature that contact angle measurements can be used in the calculation of surface tensions [14–16]. In the case of pure liquids and smooth, homogeneous, rigid, and insoluble solid surfaces, the contact angle is a thermodynamic parameter, which can be used to calculate the solid interfacial tension by different techniques [16, 17]. These techniques were inspired by the idea of using the Equation (1) first derived by Thomas Young in 1805 which is given by [13]:

$$\cos\theta = \frac{\gamma_s - \gamma_{sl}}{\gamma_l} \qquad (1)$$

This equation is a thermodynamic equilibrium condition for an ideal solid-liquid-fluid capillary system. The contact angle (θ) is uniquely determined by the three surface energies namely, the surface energy of the solid (γ_s), surface energy of the liquid (γ_l) and the interfacial free energy between the solid and the liquid (γ_{sl}). The condition for the derivation of Young's equation is the requirement of a homogeneous, inert, non-porous and non-deformable solid surface.

In Equation (1), the values of γ_s and γ_l cannot be determined directly. An approximate measure of surface free energy of the solid (γ_s) can be taken as the critical surface tension (γ_c) at which cosθ = 1 [18]. The critical surface tension can be obtained by the extrapolation of the plot of cosθ against the surface tension for a homologous series of liquids. However, the precise value of γ_s depends on the particular series of liquids used to determine it.

Considering the solid dispersion forces, Fowkes [19] presented a more appropriate method using a geometric mean equation. Modification of Fowkes equation was later made by Owens and Wendt [20] and Kaelble [21] assuming the polar attraction forces. Wu [22] used a harmonic equation to obtain the value of γ_s, which combines both the polar and dispersion forces. Wu's approach has been satisfactorily verified by several other authors [23, 24]. To verify Wu's approach, two liquids of dissimilar polarity are selected. For obtaining the γ_s of polymers, water and methylene iodide have been reported as the useful pair of liquids [25]. The harmonic mean equations for water and methylene iodide are given as Equations (2) and (3):

$$(1+\cos\theta_w)\gamma_w = 4\left[\frac{\gamma_w^d\gamma_s^d}{\gamma_w^d+\gamma_s^d}+\frac{\gamma_w^p\gamma_s^p}{\gamma_w^p+\gamma_s^p}\right] \tag{2}$$

$$(1+\cos\theta_m)\gamma_m = 4\left[\frac{\gamma_m^d\gamma_s^d}{\gamma_m^d+\gamma_s^d}+\frac{\gamma_m^p\gamma_s^p}{\gamma_m^p+\gamma_s^p}\right] \tag{3}$$

where the superscripts d and p stands for the contribution due to dispersion and polar forces respectively. Data for water and methylene iodide, taken from the literature [20] is given in the Table 2.

γ_s^d and γ_s^p for different samples of epoxy/SAN blends, epoxy/glass fibre composites and epoxy/SAN/glass fibre composites were determined by solving Equations (2) and (3) with the help of a C program.

According to Owens-Wendt theory, the total free surface energy (γ_s) is the sum of its dispersive (γ_s^d) and polar (γ_s^p) components (4):

$$\gamma_s = \gamma_s^d + \gamma_s^p \tag{4}$$

The work of adhesion (W_A) can be calculated using the Equation (5):

$$W_A = (1+\cos\theta)\gamma_l \tag{5}$$

The interfacial free energy can be calculated using the Dupre's equation [26] (6):

$$\gamma_{sl} = \gamma_s + \gamma_l - W_A \tag{6}$$

The spreading coefficient (S_c) [26] and Girifalco-Good's interaction parameter (ϕ) between the polymer and the liquid were calculated the using the Equations (7) and (8):

Table 2. The dispersive (γ_l^d) and polar (γ_l^p) components and surface energy (γ_l) for selected liquids

Liquid	γ_l [mJ/m²]	γ_l^d [mJ/m²]	γ_l^p [mJ/m²]
Water	72.8	21.8	51.0
Methylene iodide	50.8	49.5	1.3

$$S_c = \gamma_s - \gamma_{sl} - \gamma_l \tag{7}$$

$$\phi = \frac{\gamma_l(1+\cos\theta)}{2(\gamma_l\gamma_s)^{\frac{1}{2}}} \tag{8}$$

5. Results and discussion

5.1. Morphological analysis

Morphological analysis of the blend was performed using scanning electron microscopy. The SEM micrographs of fractured surfaces of epoxy/SAN blends are given in the Figure 3. The micrographs confirm the two-phase morphology of the blends. The heterogeneous morphology of the blends is due to the reaction induced phase separation (RIPS). Initially the system was miscible due to the low molecular weight of the epoxy prepolymer but during curing, molecular weight increases and the contribution to the entropy and free energy of mixing lessened resulting in two-phase morphology. Different morphologies such as dispersed, cocontinuous and phase inverted were developed depending on the composition. 5 phr and 10 phr blends show dispersed morphology in which SAN particles are uniformly dispersed in the continuous epoxy phase. The number of domains increased with composi-

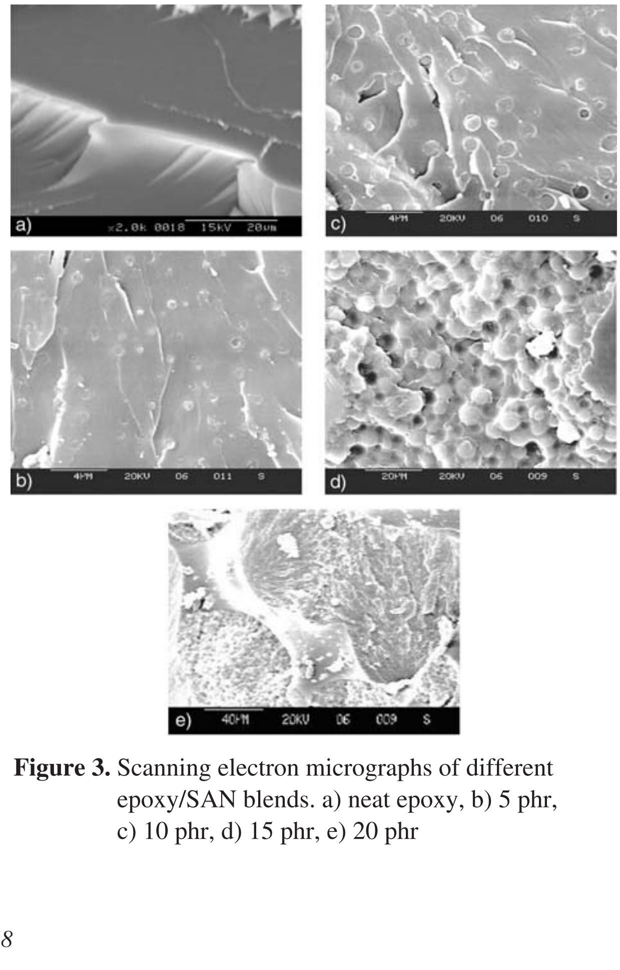

Figure 3. Scanning electron micrographs of different epoxy/SAN blends. a) neat epoxy, b) 5 phr, c) 10 phr, d) 15 phr, e) 20 phr

tion and the dispersed domains has uniform particle size distribution. The number average diameter ($\overline{D}_n$), weight average diameter ($\overline{D}_w$) and poly dispersity index (*PDI*) of the 5 phr and 10 phr blends were calculated using the Equations (9), (10) and (11):

$$\textit{Number average diameter}, \overline{D}_n = \frac{\sum n_i d_i}{\sum n_i} \qquad (9)$$

$$\textit{Weight average diameter}, \overline{D}_w = \frac{\sum n_i d_i^2}{\sum n_i d_i} \qquad (10)$$

$$\textit{Polydispersity index}, PDI = \frac{\overline{D}_w}{\overline{D}_n} \qquad (11)$$

where n_i is the number of domains having diameter d_i. The interparticle distance and interfacial area per unit volume were calculated using the Equations (12) and (13) [27]:

$$\textit{Interparticle distance} = d_{TP}\left[\left(\frac{\pi}{6\phi_{TP}}\right)^{\frac{1}{2}} - 1\right] \qquad (12)$$

$$\textit{Interfacial area per unit volumene} = \frac{3\phi_{TP}}{r} \qquad (13)$$

d_{TP} is the number average diameter of the domains, r is the number average radius of the domains and ϕ_{TP} is the volume fraction of the dispersed phase. These parameters are given in Table 3. It can be seen that the domain diameter was increased with increase in SAN content while poly dispersity index remains constant indicating the uniform particle size distribution. The interparticle distance decreased whereas the interfacial area per unit volume increased on increasing the SAN content in the blends. In the case of 15 phr blends the thermoplastic particles found to coagulate and results in cocontinuous morphology. When the SAN content is more than 15 phr, blends exhibited a phase-inverted morphology, which consisted of epoxy domains in thermoplastic continuous phase. This may be due to the viscosity difference between thermoset and thermoplastic [28]. The phase separation in thermoplastic modified epoxy resin occurs via. spinodal decomposition and is determined by the two competitive processes i. e., phase separation and crosslinking reaction [29]. The SEM of fractured surface, given in Figure 3, revealed that the surfaces of blends were rough and rigid but the surface of unmodified epoxy resin was smooth, indicating the characteristics of a brittle material. It is to be noted that the surface of the blend becomes more and more rough as the concentration of SAN increases. The roughness of the surface has a significant contribution to the surface properties of blends. The SEM pictures of epoxy/glass fibre composites with different fibre volume percentage

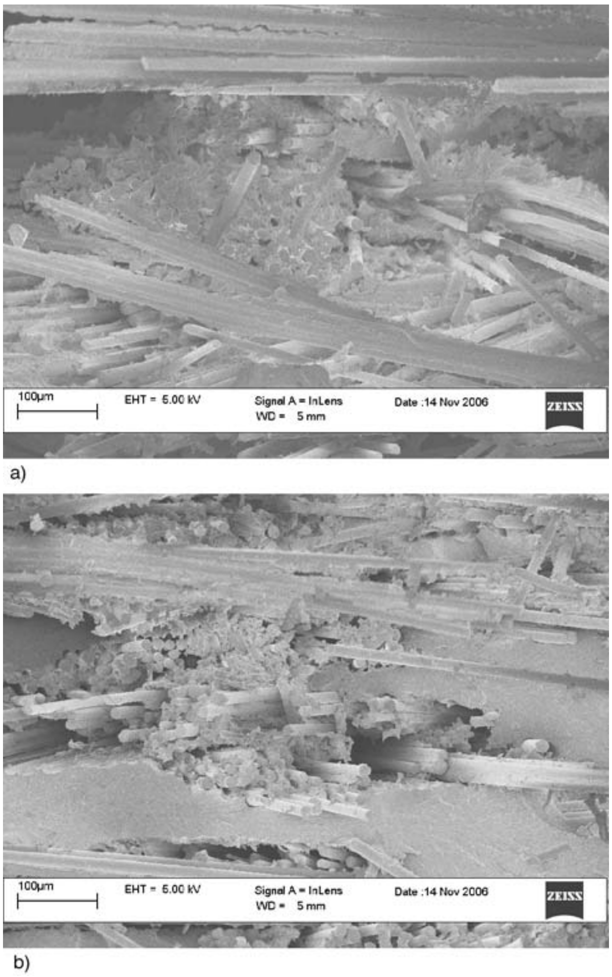

Figure 4. Scanning electron micrographs of failed surfaces of epoxy/SAN/glass fibre composites. a) EG, b) ESG

Table 3. The number average diameter, weight average diameter, poly dispersity index, interparticle distance and interfacial area per unit volume of epoxy/SAN blends

SAN content [phr]	D_n [µm]	D_w [µm]	PDI	Interparticle distance [µm]	Interfacial area per unit volume [µm^{-1}]
5	0.65	0.68	1.04	0.79	0.48
10	0.97	1.01	1.05	0.66	0.69

are shown in Figure 4. Here also the surface becomes rougher by the incorporation of fibres.

5.2. Contact angle measurements

The variation of contact angle against blend composition is given in the Figure 5. It can be observed that the blends possess higher contact angle compared to neat epoxy resin. The increase of contact angle of water and methylene iodide is prominent up to 20 phr blends. The less affinity of the blends indicates the reduction in the hydrophilic nature of the blends due to the addition of thermoplastic.

Figure 6 represents the variation of contact angle with increase in volume percentage of glass fibre of neat epoxy/glass fibre composites (EGs) (Figure 6a) and epoxy/SAN/glass fibre composites (ESGs) (Figure 6b). In all cases the contact angle is high when compared to neat cured epoxy resin. In case of EGs, θ value increases with increase in fibre loading whereas ESGs shows a decline in the θ value after 50 vol% fibre loading. This may be due to the presence of excess of non-polar groups on the surface of the blends by the addition of SAN. The increase in contact angle value can also be compared with the increase in surface roughness of the polymer surface [30]. It has been shown that the contact angle increases with increase in the roughness of the surface. The roughness of polymer surface was observed with SEM, (Figure 3 and Figure 4). The roughness of the sample surface increases by the addition of SAN thermoplastic in to the epoxy matrix. In the case of composites also, incorporation of glass fibres increases the surface roughness.

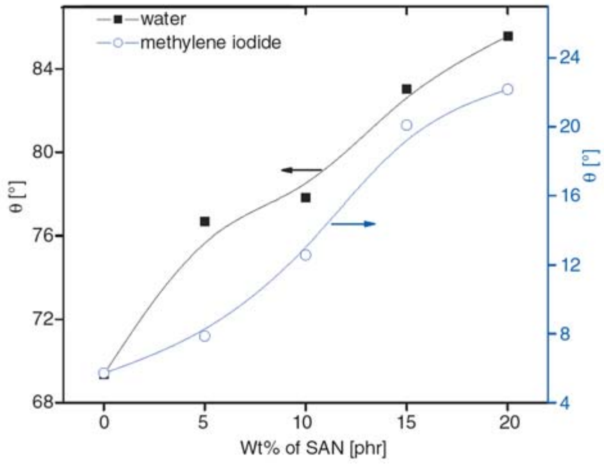

Figure 5. Contact angle against the SAN concentration for different epoxy/SAN blends

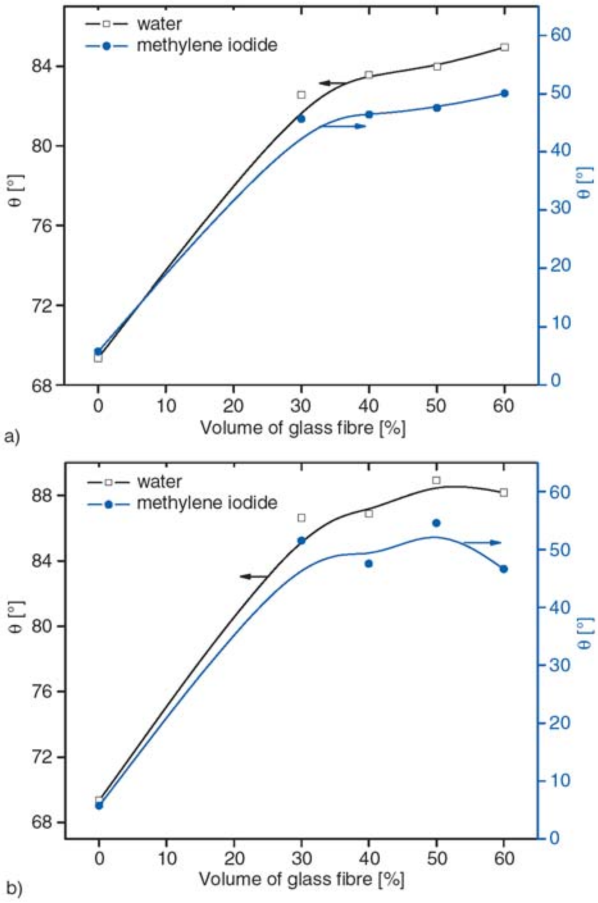

Figure 6 a) Contact angle against glass fibre concentration for epoxy/glass fibre composites (EGs), b) contact angle against glass fibre concentration for epoxy/SAN/glass fibre composites (ESGs)

Figures 7a and 7b shows the typical contact angle data (water as the liquid) at various time intervals for the epoxy/SAN blends and epoxy/glass fibre composites respectively. From the results shown in the figures, we can see that, the contact angles of samples were dramatically decreased initially. Then the contact angles changed very slowly with the elapse of time. After that, the contact angles were approaching to a static value for each of the samples. As compared with the pure epoxy, blends and composites have higher contact angles. With the increase of SAN content, the contact angles at any moment increased in the case of blends.

These results reveal that the addition of the SAN thermoplastic or glass fibre can decrease the hydrophilic nature of the epoxy, and the contact angles can be changed significantly through changing the concentration of the additive. From the above results of contact angles, a general trend of the change of contact angle (θ) with time (t) for the matrices can be established and schematically shown in Figure 8. From the figure, three characteristic regions on the curves of contact angle with respect to time can be seen. The first region is characterized by a sharp slope in which the contact angle is decreased very rapidly. The second region of the curve shows a much smaller slope, and the third region shows the values of the contact angles are almost constant. The third region on the curve in Figure 8 is characterized by a steady state behavior of wetting. A steady contact angle is reached because the cohesive interaction that helps a drop to form the spherical shape is balanced by the adhesive interaction, which is responsible for the spreading of the liquid [31].

The work of adhesion (W_A), which is the work required to separate the solid and liquid decreases in the case of both blends and composites. This fact is clear from the Figure 9a and Figure 9b, which represents the variation of W_A with respect to change in concentration of SAN thermoplastic and glass fibre respectively. The solid surface free

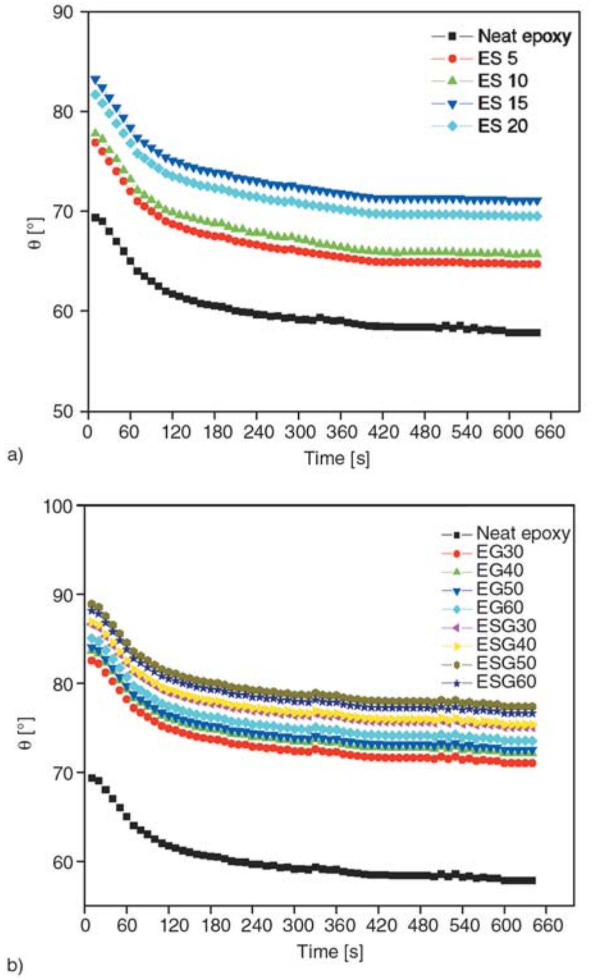

Figure 7. a) Contact angle vs time for epoxy/SAN blends with different concentrations of SAN, b) contact angle vs time for composites with different concentrations of glass fibre

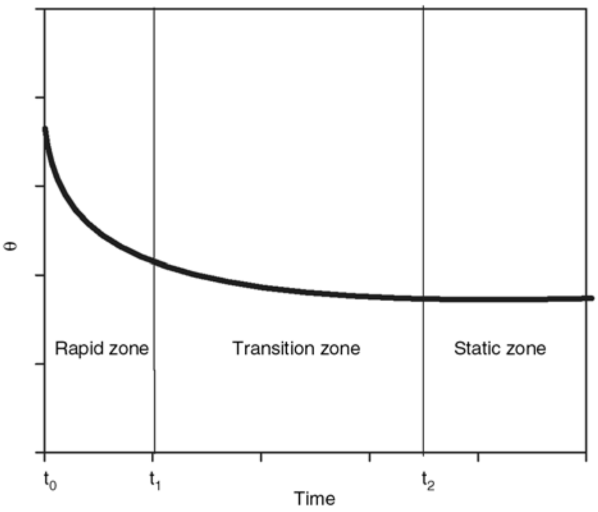

Figure 8. General form of the curves of contact angle *vs* time

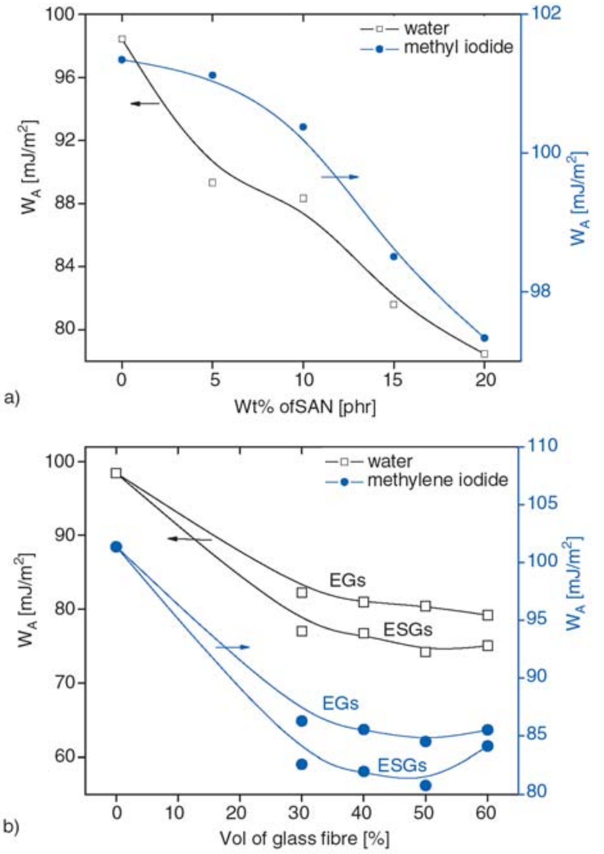

Figure 9. a) Work of adhesion as a function of composition for epoxy/SAN blends with different concentrations of SAN, b) work of adhesion as a function of composition for composites with different concentrations of glass fibre

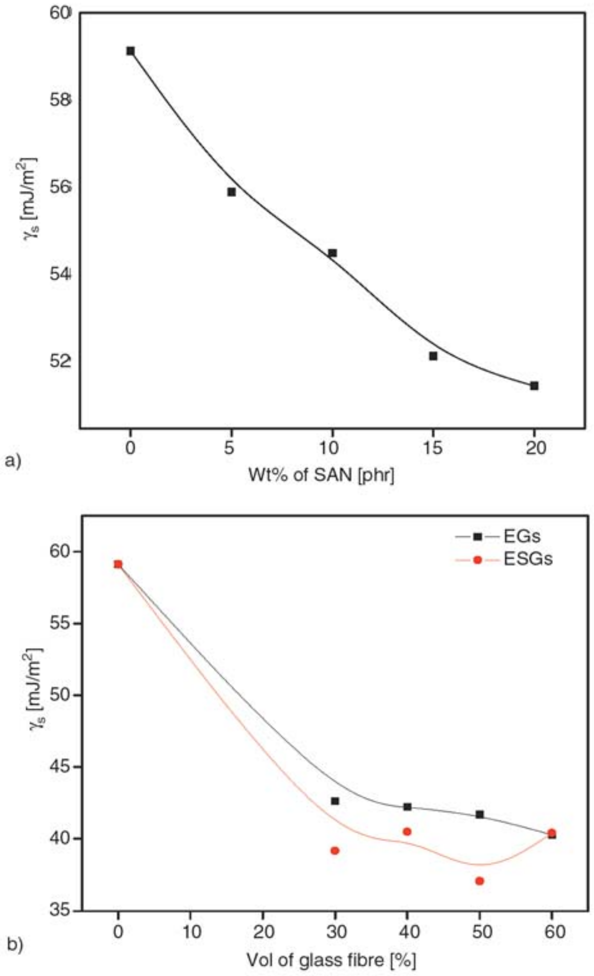

Figure 10. a) Surface free energy as a function of composition for epoxy/SAN blends with different concentrations of SAN, b) surface free energy as a function of composition for composites with different concentrations of glass fibre

Table 4. Surface free energy and Girifalco-Good's interaction parameter of blends and composites

Sample	γ_s^d	γ_s^p	γ_s	ϕ_w	ϕ_m
Neat epoxy	47.55	11.58	59.13	0.770	0.954
ES5	47.15	8.71	55.87	0.701	0.939
ES10	46.48	8.45	54.93	0.698	0.940
ES15	44.90	6.47	51.38	0.667	0.954
ES20	43.11	5.67	49.58	0.654	0.950
EG30	34.51	8.10	42.61	0.738	0.907
EG40	34.54	7.67	42.21	0.730	0.926
EG50	34.07	7.60	41.67	0.730	0.925
EG60	32.84	7.44	40.28	0.731	0.918
ESG30	32.26	6.89	39.15	0.721	0.923
ESG40	34.08	6.41	40.49	0.706	0.937
ESG50	30.75	6.30	37.05	0.714	0.924
ESG60	34.59	5.81	40.41	0.691	0.945

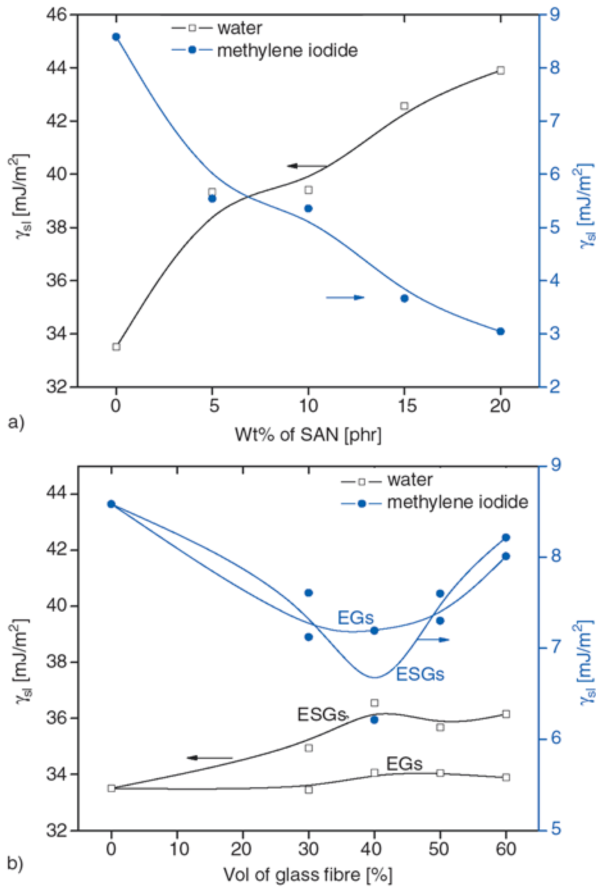

Figure 11. a) Interfacial free energy as a function of composition for epoxy/SAN blends with different concentrations of SAN, b) interfacial free energy as a function of composition for composites with different concentrations of glass fibre

energy of blends and composites obtained from Equations (2) and (3) based on the contact angle values of water and methylene iodide is plotted in Figures 10a and 10b. It can be seen that the surface free energy decreases with SAN content and the least value was observed in the case of 15 phr blends and 50 vol% fibre composites. W_A and γ_s are higher and θ is lower in the case of neat epoxy/glass fibre composites (EGs) when compared to SAN modified epoxy/glass fibre composites (ESGs).

The surface free energy (γ_s) and its dispersive and polar components are given in the Table 4. It can be observed from the Figure 10a that the γ_s values showed a decreasing trend upon blending. Both the dispersive as well as the polar components decreased up to 20 phr blends. Whereas, no significant variation in γ_s can be observed in the case of composites (Figure 10b).

Figures 11a and 11b shows the interfacial free energy (γ_{sl}) between the blend/composite surface and test liquids, water and methylene iodide. Blend surface behaves contradictory to both liquids. γ_{sl} of

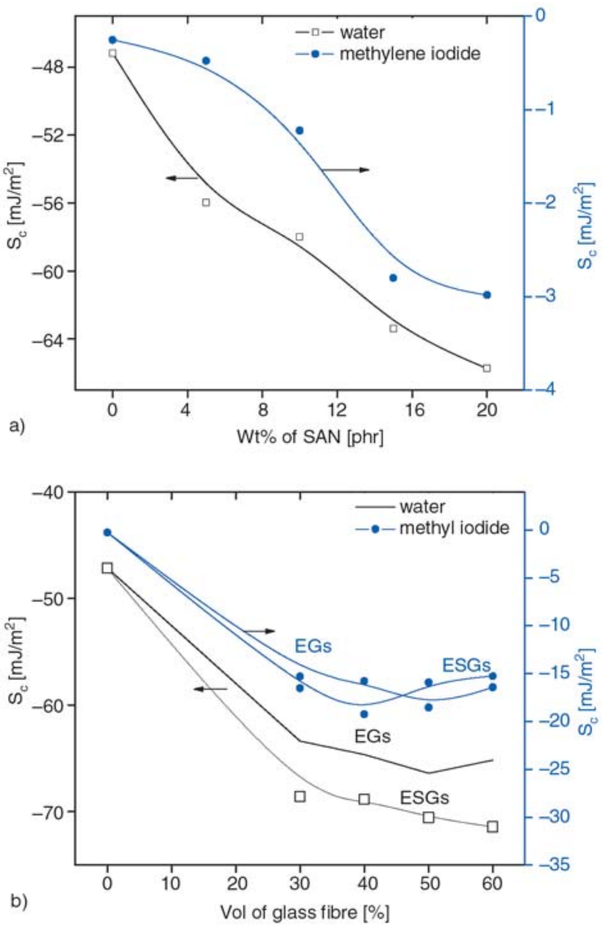

Figure 12. a) Spreading coefficient as a function of composition for epoxy/SAN blends with different concentrations of SAN, b) spreading coefficient as a function of composition for composites with different concentrations of glass fibre

water increase significantly and that of methylene iodide decreases upon blending (Figure 11a). Both these values reach optimum in the case of 20 phr blend. Composites also showed a decreasing trend with respect to fibre loading (Figure 11b).

The spreading coefficient (S_c) implies that a liquid will spontaneously wet and spread on the solid surface if the value is positive. Whereas, a negative value of S_c implies the lack of spontaneous wetting and spreading and so the existence of a finite contact angle (i. e., $\theta>0$). The spreading coefficients of blends and composites for water and methylene iodide are given in Figure 12. It is to be noted that the wetting due to methylene iodide and water decreases upon blending. The values indicate that methylene iodide (less negative) is the better wetting agent when compared to water for epoxy blends and composites.

Girifalco-Good's interaction parameter (ϕ) calculated using Equation (8) provides a good understanding of the degree of interaction between the test liquids and polymer surface. The values are given in the Table 4. A higher value indicates greater interaction. ϕ_w and ϕ_m are the Girifalco-Good's interaction parameter due to water and methylene iodide respectively. Highest value was observed in the case of neat epoxy and which decreased upon blending and fibre reinforcing. The interaction of methylene iodide with the polymer surface is higher than that of water. Incorporation of SAN as well as glass fibre reduces ϕ_w values. From the Girifalco-Good's interaction parameter values it can be suggested that the interaction of a polar liquid like water is reduced and that of a non-polar liquid like methylene iodide was not changed significantly upon blending.

The polar component of surface free energy (γ_s^p) decreases as the concentration of SAN increases. This may due to the presence of excess of non-polar groups on the surface of the blends. This nature of the blends also decreases the hydrophilic nature of the blends and composites. The prominent changes in the surface properties such as W_A, γ_{sl}, S_c and ϕ with composition of blends and composites are due to the above reasons and also due to the increase in the surface roughness.

6. Conclusions

The morphology and wetting behaviour of epoxy/SAN blends and glass fibre reinforced composites were studied in detail. It was observed that morphology of the blends changed from dispersed, cocontinuous and phase inverted structures as the SAN concentration increased from 5 to 20 phr. The roughness of the surface also increased with SAN content. Composites also had a well-packed structure as the glass fibres are closely packed in the matrix. The wetting behaviour showed significant changes in the case of blends and composites. The hydrophobic nature of the blends and composites are well understood from the increase in contact angle value compared to neat resin. The reason was assumed to be the excess number of non-polar groups on the surface and the increase in the roughness of the surface. In general, the effect of thermoplastic and fibre in epoxy is that it reduces the wettability and hydrophilicity of blends and composites.

References

[1] Potter W. G.: Epoxide resins. Springer-Verlag, New York (1970).

[2] Tercjak A., Serrano E., Remiro P. M., Mondragon I.: Viscoelastic behavior of thermosetting epoxy mixtures modified with syndiotactic polystyrene during network formation. Journal of Applied Polymer Science, **100**, 2348–2355 (2006).

[3] Salmon N., Carlier V., Schut J., Remiro P. M., Mondragon I.: Curing behaviour of syndiotactic polystyrene-epoxy blends: 1. Kinetics of curing and phase separation process. Polymer International, **54**, 667–672 (2005).

[4] Francis B., Rao V. L., Ramaswamy R., Jose S., Thomas S., Raju K. V. S. N.: Morphology, viscoelastic properties, and mechanical behavior of epoxy resin modified with hydroxyl-terminated poly(ether ether ketone) oligomer with pendent tert-butyl groups. Polymer Engineering and Science, **45**, 1645–1654 (2005).

[5] Blanco I., Cicala G., Lo Faro C.., Recca A.: Development of a toughened DGEBS/DDS system toward improved thermal and mechanical properties by the addition of a tetrafunctional epoxy resin and a novel thermoplastic. Journal of Applied Polymer Science, **89**, 268–273 (2003).

[6] Prolongo S. G., Cabanelas J. C., Fine T., Pascault J-P.: Poly(phenylene ether)/epoxy thermoset blends based on anionic polymerization of epoxy monomer. Journal of Applied Polymer Science, **93**, 2678–2687 (2004).

[7] Swier S., van Mele B.: The heat capacity signal from modulated temperature DSC in non-isothermal conditions as a tool to obtain morphological information during reaction-induced phase separation. Polymer, **44**, 6789–6806 (2003).

[8] Guo Z. S., Du S., Zhang B., Temperature field of thick thermoset composite laminates during cure process. Composites Science and Technology, **65**, 517–523 (2005).

[9] Boyard N., Serré C., Vayer M.: A physical approach to define a class A surface in polymer thermosetting composite materials. Journal of Applied Polymer Science, **103**, 451–461(2007).

[10] Jacob G. C., Starbuck J. M., Fellers J. F., Simunovic S., Boeman R G.: Fracture toughness in random-chopped fiber-reinforced composites and their strain rate dependence. Journal of Applied Polymer Science, **100**, 695–701 (2006).

[11] Mannan K. M., Talukder M. A. I.: Characterization of raw, delignified and bleached jute fibres by study of absorption of moisture and some mechanical properties. Polymer, **38**, 2493–2500 (1997).

[12] Cantero G., Arbelaiz A., Llano-Ponte R., Mondragon I.: Effects of fibre treatment on wettability and mechanical behaviour of flax/polypropylene composites. Composites Science and Technology, **63**, 1247–1254 (2003).

[13] Güleç H. A., Sarioglu K., Mutlu M.: Modification of food contacting surfaces by plasma polymerisation technique. Part I: Determination of hydrophilicity, hydrophobicity and surface free energy by contact angle method. Journal of Food Engineering, **75**, 187–195 (2006).

[14] Neumann A. W., Good R. J., Hope C. J., Sejpal M.: An equation-of-state approach to determine surface tensions of low-energy solids from contact angles. Journal of Colloid and Interface Science, **49**, 291–304 (1974).

[15] Spelt J. K., Li D., Neumann A.W.: The equation of state approach to interracial tensions, in 'Modern Approaches to Wettability' (Eds.: Schrader M. E., Loeb G. I.), Plenum Press, New York, 101 (1992).

[16] Grundke K., Bogumil T., Werner C., Janke A., Pöschel K., Jacobasch H. J.: Liquid-fluid contact angle measurements on hydrophilic cellulosic materials. Colloids and Surfaces A: Physicochemical and Engineering Aspects, **116**, 79–91 (1996).

[17] Oss C. J. V., Chaudhury M. K., Good R. J.: Interfacial Lifshitz-van der Waals and polar interactions in macroscopic systems. Chemical Reviews, **88**, 927–941 (1988).

[18] Fox H. W., Zisman W. A.: The spreading of liquids on low-energy surfaces. III. Hydrocarbon surfaces. Journal of Colloid Science, **7**, 428–442 (1952).

[19] Fowkes F. M.: Additivity of intermolecular forces at interfaces. I. Determination of the contribution to surface and interfacial tensions of dispersion forces in various liquids. Journal of Physical Chemistry, **67**, 2538–2541 (1963).

[20] Owens D. K., Wendt R. C.: Estimation of the surface free energy of polymers. Journal of Applied Polymer Science, **13**, 1741–1747 (1969).

[21] Kaelble D. H., Dynes P. J., Cirlin E. H.: Interfacial bonding and environmental stability of polymer matrix composites. The Journal of Adhesion, **6**, 23–48 (1974).

[22] Wu S.: Calculation of interfacial tension in polymer systems. Journal of Polymer Science Part C: Polymer Symposia, **34**, 19–30 (1971).

[23] El-Shimi A., Goddard E. D.: Wettability of some low energy surfaces. Journal of Colloid and Interface Science, **48**, 242–248 (1974).

[24] Pyter R. A., Zografi G., Mukerjee P.: Wetting of solids by surface-active agents: The effects of unequal adsorption to vapor-liquid and solid-liquid interfaces. Journal of Colloid and Interface Science, **89**, 144–153 (1982).

[25] Lin J. W. P., Dudek L. P., Majumdar D.: Wetting properties of homopolymers and copolymers of pentafluorostyrene and methylacrylate and homopolymer blends. Journal of Applied Polymer Science, **33**, 657–667 (1987).

[26] Dupré A.: Theorie mechanique de la chaleur. Gauthier-Villars, Paris (1869).

[27] Francis B., Thomas S., Asari G. V., Ramaswamy R., Jose S., Rao V. L.: Synthesis of Hydroxyl-terminated poly(ether ether ketone) with pendent tert-butyl groups and its use as a toughener for epoxy resins. Journal of Polymer Science Part B: Polymer Physics, **44**, 541–556 (2006).

[28] Song X. Z., Zheng S. X., Huang J., Zhu P. P., Guo Q. P.: Miscibility, morphology and fracture toughness of tetrafunctional epoxy resin/poly (styrene-co-acrylonitrile) blends. Journal of Material Science, **35**, 5613–5619 (2000).

[29] Yamanaka K., Inoue T.: Structure development in epoxy resin modified with poly(ether sulphone). Polymer, **30**, 662–667 (1989).

[30] Grundke K., Bogumil T., Gietzelt T., Jacobasch H. J., Kwok D. Y., Neumann A. W.: Wetting measurements on smooth, rough and porous solid surfaces. Progress in Colloid and Polymer Science, **101**, 58–63 (1996).

[31] Lazghab M., Saleh K., Pezron I., Guigon P. Komunjer L.: Wettability assessment of finely divided solids. Powder Technology, **157**, 79–91 (2005).

eXPRESS Polymer Letters Vol.1, No.6 (2007) 356–363
Available online at www.expresspolymlett.com
DOI: 10.3144/expresspolymlett.2007.50

Novel fluorescent amphiphilic block copolymers: photophysics behavior and interactions with DNA

X. J. Lu, L. Z. Meng, X. X. Zhong*

Department of Chemistry, Wuhan University, Wuhan 430072, P. R. China

Received 23 March 2007; accepted in revised form 5 May 2007

Abstract. In this study, novel amphiphilic fluorescent copolymers poly(N-vinylpyrrolidone)-*b*-poly(N-methacryloyl-N'-(α-naphthyl)thiourea) (PVP-*b*-PNT) were synthesized via ATRP with poly(N-vinylpyrrolidone)-Cl as macroinitiator and N-methacryloyl-N'-α-naphthylthiourea (NT) as hydrophobic segment. PVP-*b*-PNT copolymers were characterized by ^{1}H NMR, GPC-MALLS and fluorescence measurements. The aggregation behavior of PVP-*b*-PNT in water was investigated by transmission electron microscope (TEM) and dynamic light scattering (DLS) measurement. The photophysics behavior of PVP-*b*-PNT showed that block copolymer formed strong excimer. The interaction of DNA with the block copolymer made the excimer of block copolymer quench. The cytotoxicity result of PVP-*b*-PNT in cell culture in vitro indicated that this copolymer PVP-*b*-PNT had good biocompatibility.

Keywords: *biocompatible polymers, block, fluorescence, excimer*

1. Introduction

Amphiphilic block and graft copolymers consisting of hydrophilic and hydrophobic segments are self-assembling materials, which are capable of forming polymer assemblies, micelles, and vesicles in aqueous solutions, and have been used extensively in both research and technology [1, 2]. Amphiphilic block copolymers are also very attractive polymers as carriers for the controlled delivery of drugs due to their water soluble part and hydrophobic part [3, 4].

Fluorescent polymers are gaining increased attention due to their high sensitivity and ease of measurement. For example, conjugated polymer chemosensors have recently been used with great success for the detection of a range of analytes from biomolecules to explosives [5]. Fluorescent polymers have several advantages over small molecule sensors due to enhancements associated with electronic communication between receptors along the polymer backbone, processability, and ease of structural modification.

Photophysical studies on fluorescent polymers in confined environments play a vital role in many natural and biological processes. The behavior of polymers in solution can be studied by attaching labels of various types, and inferring motion or location of the polymer from the label. Fluorescent labels have been employed using special shape, position or depolarization of light to obtain information about the macromolecule [6]. In aqueous media, amphiphilic copolymers self-organized into micelles which are one of organized environments. The most important property of such compartmentalized micellar media is that they have the ability to concentrate guest molecules into relatively small effective volumes and then to promote the re-encounter of such molecules [7]. This property also makes them a good device for inducing efficient electrostatic interactions between the micelle head groups and the guest molecules as well as strong

---

*Corresponding author, e-mail: lzhmeng@whu.edu.cn hydrophobic interactions of these molecules with the micelle chains.

Poly(N-vinylpyrrolidone) (PVP) is a very interesting polymer because it is well water-soluble, biocompatible and has been extensively used in pharmaceutical industry [8]. Recently, PVP can be found in various drug delivery systems, including microspheres, nanoparticles, liposomes, and polymer conjugates. The researches of amphiphilic PVP copolymer used as a promising fluorescent probe for measurements of biomacromolecules [9] and a promoter for enhancement of DNA amplification by polymerase chain reaction [10] were investigated.

In our case, we preferred amphiphilic fluorescent copolymer that had a good biocompatiblity and well-defined structure. Atom transfer radical polymerization (ATRP) is an extremely active area of polymer synthesis research [11]. From this point of view we have prepared well-defined PVP by ATRP. The resulting product has a controlled molecular weight and narrow molecular weight distribution. In this contribution novel amphiphilic fluorescent copolymers poly(N-vinylpyrrolidone)-*b*-poly(N-methacryloyl-N'-(α-naphthyl) thiourea) (PVP-*b*-PNT) were synthesized via ATRP with PVP-Cl as macroinitiator and N-methacryloyl-N'-α-naphthylthiourea (NT) as hydrophobic segment. The photophysics behavior of the amphiphilic block copolymers was investigated by fluorescent measurements in detail. The major application of the fluorescent polymer in aqueous media was used in the field of biological molecules, so the interaction of the block copolymer with DNA was described and the cytotoxicity of the copolymers in vitro were also evaluated. The results showed that the copolymers exhibited exquisite fluorescence property and good biocompatibility.

2. Experimental section

2.1. Materials

N-Vinylpyrrolidone (VP, Acros, 99%) was purified by distillation under reduced pressure to remove the inhibitors before use. CuCl (Aldrich, 98%) was purified by stirring in acetic acid, washed with methanol, and then dried in vacuum. Methacryloyl chloride was prepared by refluxing a mixture of thionyl chloride and methacrylic acid, followed by distillation. $CuCl_2$ (Aldrich, 99.9%), 2,2'-bipyridine (bpy, Acros, 99%), methyl 2-chromopropionate (MCP, Aldrich, 97%) and N, N-dimethylformamide (DMF, Acros, HPLC grade) were used as received without further purification. Plasmid pBR322 DNA was from Huamei Biological Engineering Company. α-Naphthylamine, basic alumina and all other reagents were from Shanghai No.1 Chemical Reagent Factory and used as received without further purification.

2.2. Preparation of N-methacryloyl-N'-(α-naphthyl) thiourea (NT)

KSCN (17.05 g, 0.175 mmol) was dissolved in 150 ml of anhydrous acetonitrile and the solution was then cooled by an ice-salt bath. Under stirring methacryloyl chloride (14.4 ml, 0.15 mol) was added dropwise into it. And then the reaction was allowed to stir for 5 h at room temperature. The precipitated KCl was removed by filtration. α-Naphthylamine (18.61 g, 0.13 mol) was dissolved in 60 ml of acetonitrile and added dropwise into the above filtrate with stirring at room temperature. The system turned to yellow from dark red and began to precipitate rapidly. After being filtrated and washed with water, the yellow precipitate was vacuum-dried. The solid was dissolved in acetone and subsequently a large excess of cold water was added to give crystalline NT, yield: 75%; mp: 135–137°C. ^1H NMR (300 MHz, $CDCl_3$): δ (ppm) 12.53 and 8.88 (each s, 1H, 2NH), 7.19–7.93 (m, 7H, ArH), 5.99 and 5.67 (each m, 1H, CH_2=), 2.05 (s, 3H, CH_3). Elemental analysis: Calcd for $C_{15}H_{14}N_2OS$ [%]: C, 66.64; H, 5.22; N, 10.36; S, 11.86. Found [%]: C, 66.59; H, 5.30; N, 10.28; S, 11.78. ESI-MS (in CH_3CN): *m*/*z* (*RI*): 271 (M^++1, 100) [12].

2.3. Preparation of amphiphilic block copolymer by ATRP

Amphiphilic block copolymers PVP-*b*-PNT were synthesized by ATRP in DMF. Macroinitiator PVP-Cl (target DP = 250) was synthesized according to the procedure for the polymerization of VP [13]. The M_n was 18 600 g/mol and PDI was 1.26 by GPC-MALLS in DMF. In a typical run, a 25 ml round-bottom flask was charged with DMF (5 ml), NT, macroinitiator PVP-Cl and catalyst CuCl/bpy with the following relative molar ratio NT:PVP-Cl:CuCl:bpy = 20:1:1:2 (i. e. target DP = 20). The flask was sealed with a rubber septum and evacuated and back-filled with nitrogen for three times. The flask placed in a preheated oil bath was kept at 60°C for 24 h. Then the reaction mixture was diluted with $CHCl_3$ and passed through a basic alumina column to remove ATRP catalyst. The resulting solution was then concentrated and the copolymer was precipitated into excess diethyl ether. The obtained copolymer was dried under vacuum to provide PVP-*b*-PNT-III. This protocol was repeated with varying the molar ratios of NT to PVP-Cl to obtain more water-soluble amphiphilic block copolymer PVP-*b*-PNT-I and II.

2.4. Instruments

All ^{1}H NMR spectra were recorded on a Varian Mercury VX-300 MHz spectrometer (USA). Elemental analysis was conducted on a Flash EA 1112 series elemental autoanalyzer (Italy). Mass spectra were obtained on an LCQ-Advantage electrospray ionization-mass spectrometer (ESI-MS) (Finnigan, England). Steady-state fluorescence spectra of copolymer solution were obtained on a Shimadzu RF-5301PC spectrometer (Japan) at room temperature. Gel permeation chromatography-multi-angle laser light scatting (GPC-MALLS) is convenient for determination of the true molecular weight and molecular weight distribution of polymer without standard sample. Number molecular weights M_n, and polydispersity M_w/M_n of the samples were determined by a DAWN®DSP multi-angle laser photometer in DMF at a flow rate of 1.00 ml/min at 25°C.

2.5. Transmission electron microscope (TEM) observation

The size and morphology of copolymer aggregates were recorded by a JEM-100CXII transmission electron microscope (Japan). The polymer solutions were placed onto the TEM copper grid covered by a polymer support film. After 15 min, the excess solution was allowed to dry in atmosphere and at room temperature for 2 h before observation.

2.6. Dynamic light scattering observation

Dynamic light scattering (DLS) was used for the determination of particle size in water. For this analysis, a series of aqueous solutions of PVP-*b*-PNT with concentration of 2 g/l were prepared by dissolving the polymer directly in water. Each measurement was carried out in triplicate at 25°C at an angle of 90°C. The size distribution of particles and the intensity of mean size were recorded.

2.7. In vitro cytotoxicity test

The cytotoxicity of PVP-*b*-PNT was evaluated by using the MTT assay according to the method of Mosmann [14]. 5 000 A549 cells/well, MTT solution 2.0 g/l and Hank's balanced salt solution (HBSS) as a medium were selected to carry out the cytotoxicity tests. The test was performed as follows: after A549 cells were attached to the 96 wells and incubated for 24 h at 37°C, the different concentration of PVP-*b*-PNT dissolved in HBSS were added to the wells. To each well 50 µl of MTT solution was added after the wells were incubated for another 72 h at 37°C. The plates were incubated for an additional 4 h at 37°C and the MTT solution was removed. Negative (HBSS) control wells were treated similarly as above. Absorbance was measured spectrophotometrically at 550 nm using a MuLTiskAn MK3 unit. Cell viability (as a percent of the negative control) was calculated from the absorbance values.

3. Results and discussion

3.1. ATRP of PVP-*b*-PNT block copolymer

Block copolymers were prepared via ATRP using the PVP-Cl as macroinitiator, NT as hydrophobic monomer and CuCl/bpy complex as catalyst in DMF. Though a bpy-based catalyst is less active compared to tripodal amines and cyclic amines [11], the investigation on ATRP of acrylamide and dimethyl(1-ethoxycarbonyl)vinyl phosphate using CuCl/bpy as catalyst were reported [15, 16]. So the bpy ligand was chosen to prepare PNT block. In this section, a series of well-defined block copolymers (PVP-*b*-PNT) with different hydrophobic segment is synthesized using the same PVP-Cl (M_n = 18 600, PDI = 1.26) via ATRP. The increase of molecular weight with conversion and relatively low PDI of the copolymers demonstrate the controllable characteristic of this polymerization.

The chemical composition of block copolymers is determined by ^{1}H NMR. A typical ^{1}H NMR spectrum of PVP-*b*-PNT-III in $CDCl_3$ is shown in Fig-

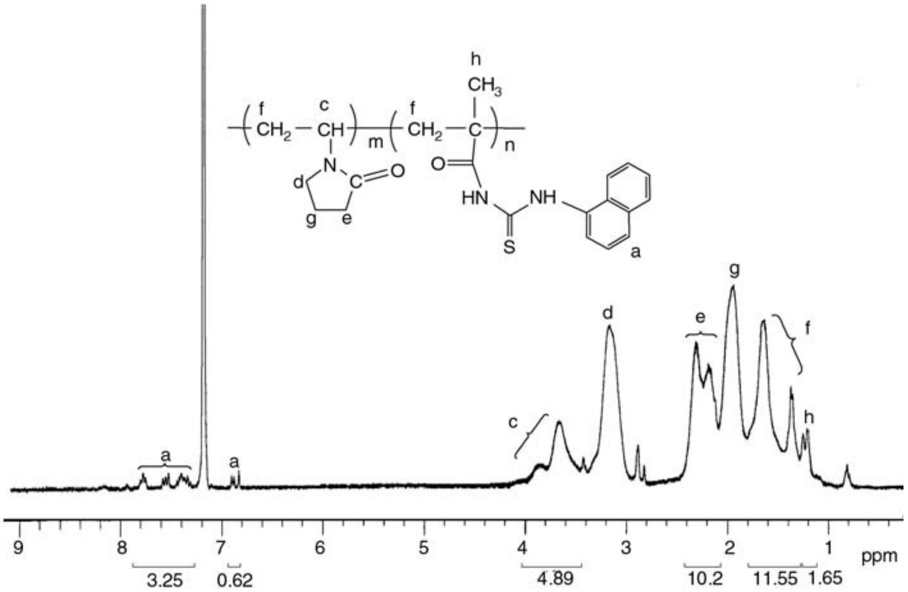

Figure 1. ^{1}H NMR spectrum of PVP-*b*-PNT-III in $CDCl_3$

ure 1. The multiple of shift from 6.8 to 7.93 is attributed to the protons of the hydrophobic naphthyl groups of the block copolymer. The hydrophobic content is calculated from the relative integrated area of peak a corresponding to the protons of the naphthyl groups of the hydrophobic chains compared to that of peak c corresponding to the protons of CH–N group in the hydrophilic backbone. The molecular weights of final copolymers were determined by GPC-MALLS in DMF.

The molecular weights of the block copolymers determined from ^{1}H NMR are consistent with those determined by GPC-MALLS in DMF and the molecular weight distributions are relatively low which are listed in Table 1. These results confirm that the molecular weight and the unit composition of block copolymers can be successfully controlled by varying the molar ratio of monomer to macroinitiator via sequential ATRP.

Table 1. Molecular characteristics of PVP-*b*-PNT

Entry	Yield[a] [%]	^{1}H NMR		M_n[b] [g/mol]	M_w/M_n[b]
		PVP	PNT		
PVP-Cl		100	0	18 600	1.26
PVP-*b*-PNT-I	89	97	3	20 000	1.33
PVP-*b*-PNT-II	83	95	5	21 300	1.32
PVP-*b*-PNT-III	78	90	10	22 500	1.38

[a] Yield of copolymer determined by gravimetric.

[b] Number-average molecular weight and polydispersity in DMF by GPC-MALLS.

3.2. Aggregation behavior of PVP-*b*-PNT in water

The fluorescence emissions of PVP-*b*-PNT solution in aqueous show the same excimer emission in λ_{max} = 448 nm in Figure 2. The intramolecular and intermolecular aggregations exist in all block PVP-*b*-PNT in water even for that with the shortest hydrophobic block in copolymer backbone. A similar result was reported for pyrene labeled poly(N-isopropylacrylamide) [17].

In aqueous solution the PVP-*b*-PNT can orient themselves in a way that they expose their hydrophilic groups toward water and simultaneously protect their hydrophobic groups from the contact with water, and consequently they are able to form hydrophobic microdomains by inter- and intramol-

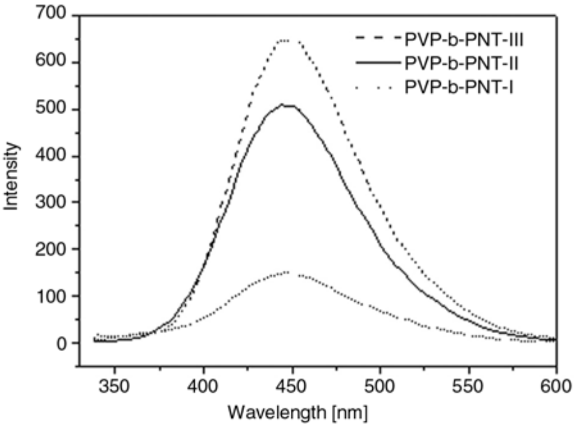

Figure 2. Fluorescence emission spectra of PVP-*b*-PNT solution at the concentration of 0.4 g/l at 20°C excited at 330 nm

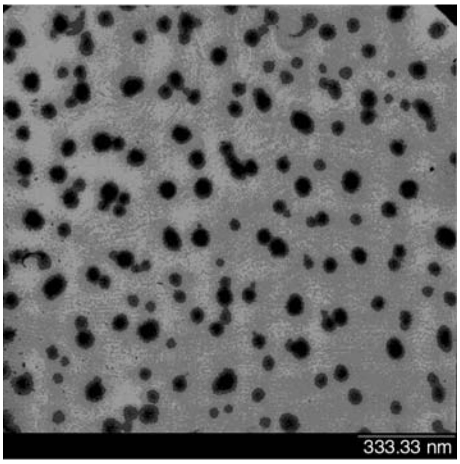

Figure 3. TEM of PVP-*b*-PNT-III aqueous solutions 2 g/l

ecular interactions. PVP-*b*-PNT micelles with short hydrophobic block in this case should have a core-shell structure.

The successful formation of micelles was confirmed by TEM measurement. Figure 3 shows the TEM image of the micelles formed by PVP-*b*-PNT-III copolymers. It can be seen that the micelles take a spherical morphology. Micelles composed of PVP-*b*-PNT-III in water at a concentration of 2 g/l feature a single narrow size distribution with a mean diameter about 40 nm. As a typical example, the particle size distribution of PVP-*b*-PNT-III micelles determined by dynamic light scattering is shown in Figure 4. Mean sizes of micelles formed by PVP-*b*-PNT-III copolymers are ca. 58 nm in diameter, which are much larger in the size than that observed by TEM in dried model.

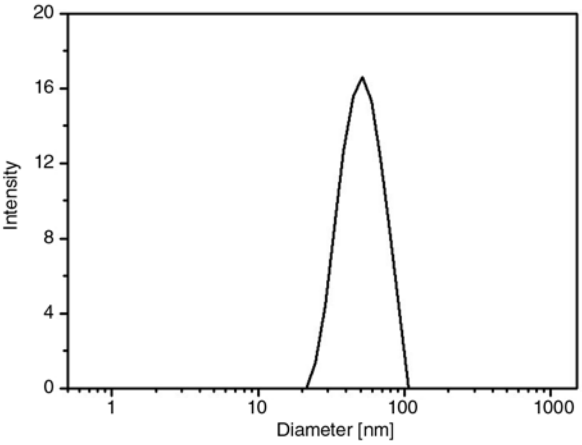

Figure 4. Size distribution of micells composed of PVP-*b*-PNT-III aqueous solutions 2 g/l measured by DLS

3.3. The effect of chain architecture on photophysics

When the fluorescent hydrophobes (naphthyl group) were incorporated in the copolymer, the photophysical response may effectively probe the copolymer behavior on the microscopic level [18]. The distribution of the labels was not expected to be random, but rather that the PVP-*b*-PNT copolymers would present a blocky architecture. We can address this question with respect to the distribution of the fluorescent groups along the macromolecules to form excited-state excimers under conditions of high density labels [19]. If a polymer carries a small number of naphthyl distribution along the chain, the naphthyl*/naphthyl encounter probability will be low; hence, excimer emission will be weak compared to the monomer emission. Conversely, if the copolymer presents blocks of high naphthyl density, the contribution of naphthyl excimers to the overall emission will be high.

To make this spectroscopic tool to be used effectively, it was necessary to dissolve the labeled polymers in a good solvent to avoid solvent-induced clustering of the labeles. Here, we measured the emission of PVP-*b*-PNT in $CHCl_3$. $CHCl_3$ is a good solvent for all the PVP-*b*-PNT samples prepared. The emission of block naphthyl-labeled PVP samples showed only one broad emission I_E, centered between 440 and 450 nm, characteristic of naphthyl excimer emission. It should be noted that the monomer emission was not observed in PVP-*b*-PNT solutions. This phenomenon is quite different from the previous literatures on naphthyl-labeled dendrimer and random polymers [20, 21].

In order to investigate the chain architecture on the photophysics of copolymer, we measured the emission of the random naphthyl-labeled PVP with equal absorbance of PVP-*b*-PNT dissolved in $CHCl_3$. The fluorescence spectrum in Figure 5 shows two major bands, one at shorter wavelength (monomer emission) with λ_{max} = 375 nm and the other a broad but weak band at longer wavelengths (excimer emission) with λ_{max} = 448 nm. The emission of random polymer shows both monomer and excimer emission, which is different from the block polymer. The fluorescent observation results show that the copolymers with a blocky architecture tend to present strong excimer emission than random copolymer.

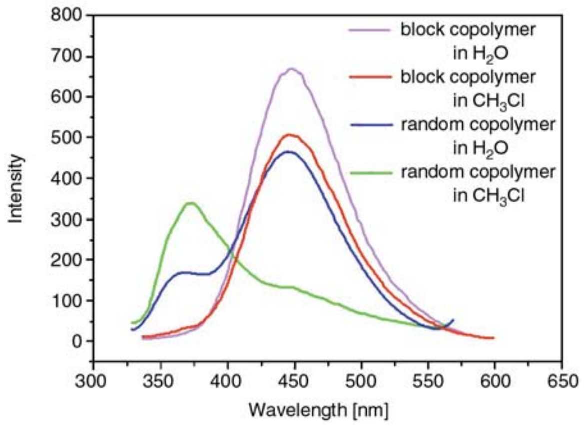

Figure 5. Fluorescence emission spectra of random and block copolymers solution at 20°C excited at 330 nm. Both solutions in $CHCl_3$ have equal absorbance (A_{330} = 0.2)

The appearances of the excimer band with maximum around 448 nm are observed in random and block polymers. Generally the naphthyl excimer emission is about 400 nm, but in this case, the excimer emission wavelength of PVP-*b*-PNT and random polymer is red shifted to 448 nm, which is due to the hydrophobic monomer chemistry structure. Naphthyl thiourea monomer has a tautomeric form, which brings a big conjugated π bond between naphthyl and thiourea residue [22]. The special structure makes higher fluorescence efficiency and reflects the red shift in excimer emssion. A similar phenonmenon was observed in other conjugated polymers [23].

At the same time, we dissolved the random and block polymers in water, respectively. As the emission spectra recoded in Figure 2, two trends are apparent: 1. the I_E of block polymer and random polymer increase; 2. the I_E is significantly higher of aqueous solution of block polymers, compared to the random polymers.

The block polymers exhibit stronger excimer band than that of the random polymers in both $CHCl_3$ and aqueous media. These results suggest that inter- and intra-molecular associations facilitate excimer formation for block and random polymers. But the association ability is stronger in block polymers than in random polymers. For block polymer solution in $CHCl_3$, the broad excimer emission I_E centering between 440 and 450 nm derives from intramolecular association. The intramolecular association results from interactions between the naphthyl groups within the block itself. For the block polymer solution in water, the strong excimer emission I_E comes from inter- and intra-association of block chains. Meanwhile, the intramolecular and intermolecular association results from interactions between naphthyl groups at the different chains.

3.4. Interactions with DNA

The blocking of the fluorescent probe into the polymer backbone provides the possibility to employ luminescent techniques at very low concentrations. The nucleotide sensing and quantification by means of luminescent probes represent an important target in supramolecular chemistry due to their many biological and biomedical implications [25]. The interaction of the PVP-*b*-PNT with DNA is described and we found the potential molecular recognition of this for DNA in aqueous solution.

Fluorimetric titrations were conducted with addition of DNA solutions. The fluorescence spectra were shown in Figure 6. The excimer emission was quenched after DNA addition. An interpretation for DNA's quenching effect could be a multitopic hydrogen bonding interaction between the hydrophobic thiourea and the DNA fragment. Bisthiourea moieties selectively bind to dihydrogenphosphate via multitopic hydrogen bonding, giving stronger complexes with $H_2PO_4^-$ [24]. Naphthyl or groups bounded to polymer interact in aqueous media tend to form a sandwich-like dimeric conformation (excimer) regularly [25]. In the solution of PVP-*b*-PNT and DNA, the interaction between DNA and thiourea of polymer chain inhibits naphthyl groups to form a sandwich-like dimeric conformation which increases the excited-state energy and decreases fluorescence intensity.

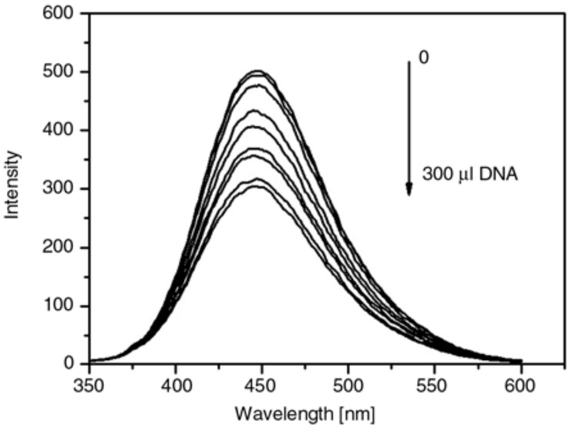

Figure 6. Fluorescence spectroscopy of PVP-*b*-PNT-III aqueous solution ($5\cdot10^{-5}$ g/ml in 0.05 M Tris-HCl, pH = 7.4) upon the addition of DNA (0.114 mol/l) at 20°C excited at 330 nm

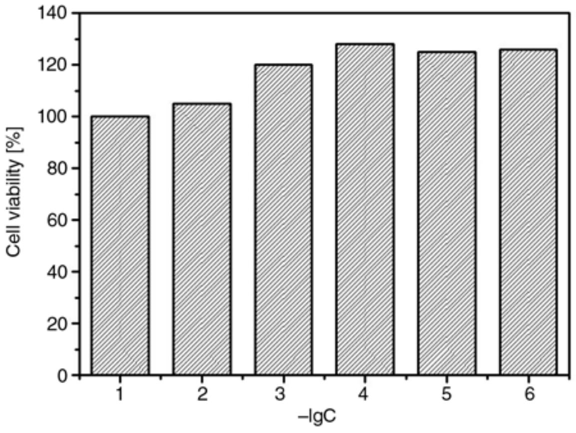

Figure 7. Cytotoxicity of PVP-*b*-PNT-III in vitro by MTT assay

3.5. Cytotoxicity of PVP-*b*-PNT in vitro

To determine biocompatibility of the fluorescent copolymer PVP-*b*-PNT, its cytotoxicity towards A549 cells was determined by means of the MTT assays. The effect of copolymer concentration on cell viability was illustrated in Figure 7, within experimental error, negligible, the cell viabilities being above 100% relative to a negative control at concentration of PVP-*b*-PNT-III ranging from 10^{-6} to 10^{-1} mg/ml. In other words, solution of PVP-*b*-PNT-III has no apparent cytotoxic effect on A549 cells. This may be attributed to the biocompatibility of the hydrophilic PVP shell formed by PVP-*b*-PNT-III on self-aggregation.

4. Conclusions

New fluorescence copolymers PVP-*b*-PNT were synthesized by ATRP with PVP-Cl and N-methacryloyl-N'-α-naphthylthiourea (NT). For the block polymer solution in water, the emission of PVP-*b*-PNT samples showed only one broad emission I_E, centered between 440 and 450 nm, characteristic of naphthyl excimer. The higher excimer emission I_E comes from inter- and intra-aggregation between naphthyl groups at the different chains. DLS and TEM observation suggested block polymers in water self-assembled into spherical micelles. For block polymer solution in $CHCl_3$, the broad excimer emission I_E derives from intramolecular association between the naphthyl groups within the block itself. Fluorescence measurements of the structurally well-defined PVP-*b*-PNT polymer can provide templates for developing a wide rang of fluorescent amphiphilic macromolecules and characterize conformational dynamics of polymer chains.

Acknowledgements

The authors are grateful to National Natural Science Foundation for financial support (Grant No. 20474044 and 20644002) and Prof. Y. Liang, Jianghan University for his help in cell cytotoxicity test.

References

[1] Gref R., Minamitake Y., Peracchia M. T., Trubetskoy V., Torchilin V., Langer R.: Biodegradable long-circulating polymeric nanospheres. Science, **263**, 1600–1603 (1994).

[2] Discher D. E., Eisenberg A.: Polymer vesicles. Science, **297**, 967–973 (2002).

[3] Kukula H., Schlaad H., Antonietti M., Förster S.: The formation of polymer vesicles or 'peptosomes' by polybutadiene-block-poly(l-glutamate)s in dilute aqueous solution. Journal of the American Chemical Society, **124**, 1658–1663 (2002).

[4] Yusa S-I., Fukuda K., Yamamoto T., Ishihara K., Morishima Y.: Synthesis of well-defined amphiphilic block copolymers having phospholipid polymer sequences as a novel biocompatible polymer micelle reagent. Biomacromolecules, **6**, 663–670 (2005).

[5] He F., Tang Y., Yu M. H., Feng F., An L. L., Sun H., Wang S., Li Y. L, Zhu D. B, Bazan G. C.: Quadruplex-to-duplex transition of g-rich oligonucleotides probed by cationic water-soluble conjugated polyelectrolytes. Journal of the American Chemical Society, **128**, 6764–6765 (2006).

[6] Carvell M., Robb I. D., Small P. W.: The influence of labeling mechanisms on the fluorescence behaviour of polymers bearing fluorescein labels. Polymer, **39**, 393-398 (1998).

[7] Chowdhury P., Chakravorti S.: Effect of pH in the photophysics of 2-hydroxy 1-naphthaldehyde in micellar systems. Journal of Photochemistry and Photobiology A: Chemistry, **179**, 95–104 (2006).

[8] Haaf F., Sanner A., Straub F.: Polymer of N-vinyl pyrrolidone: synthesis, characterization and uses, Polymer Journal, **17**, 143–152 (1985).

[9] Wu Z. Q., Gong S. L., Li C., Zhang Z., Huang W. H., Meng L. Z., Lu X. J. He Y. B.: Novel water-soluble fluorescent polymer containing recognition units: synthesis and interactions with PC12 cell. European Polymer Journal, **41**, 1985–1992 (2005).

[10] Zhang L. F., Liang Y., Meng L. Z., Lu X. J., Liu Y. H.: Preparation and PCR-amplification properties of a novel amphiphilic poly(N-vinylpyrrolidone) (PVP) copolymer. Chemistry and Biodiversity, **4**, 163–174 (2007).

[11] Matyjaszewski K., Xia J.: Atom transfer radical polymerization. Chemistry Review, **101**, 2921–2990 (2001).

[12] Li C., Lu X. J., Meng L. Z., Zhang L. F., He Y. B: Amphiphilic random copolymers based on N-isopropylacrylamide: self-aggregation behavior and interactions with nucleotides. Journal of Applied Polymer Science, **105**, 2532–2539 (2007).

[13] Lu X. J., Gong S. L., Meng L. Z., Li C., Yang S., Zhang L. F: Controllable synthesis of poly(N-vinylpyrrolidone) and its block copolymers by atom transfer radical polymerization. Polymer, **48**, 2835–2842 (2007).

[14] Mosmann T.: Rapid colorimetric assay for cellular growth and cytotoxic assays. The Journal of Immunological Methods, **65**, 55–63 (1983).

[15] Huang J., Matyjaszewski K.: Atom transfer radical polymerization of dimethyl(1-ethoxycarbonyl)vinyl phosphate and corresponding block copolymers. Macromolecules, **38**, 577–3583 (2005).

[16] Jewrajka S. K., Mandal B. M.: Living radical polymerization. 1. The case of atom transfer radical polymerization of acrylamide in aqueous-based medium. Macromolecules, **36**, 311–317 (2003).

[17] Winnik F. M.: Fluorescence studies of aqueous solutions of poly(N-isopropylacrylamide) below and above their LCST. Macromolecules, **23**, 233–242 (1990).

[18] Liaw D. J., Huang C. C., Sang H. C., Kang E. T.: Intramolecular hydrophobic aggregation of amphiphilic polysulfobetaine with various hydrophobic groups in aqueous solution. Langmuir, **15**, 5204– 5211 (1999).

[19] Lankkanen A., Winnik F. M., Tenhu H.: Pyrene-labeled graft copolymers of N-vinylcaprolactam: synthesis and solution properties in water. Macromolecules, **38**, 2439–2488 (2005).

[20] Ghaddar T. H., Whitesell J. K., Fox M. A.: Excimer formation in a naphthalene-labeled dendrimer. Journal of Physics Chemistry: B, **105**, 8729–8731 (2001).

[21] McCormick C. L., Hoyle C. E., Clark M. D.: Water-soluble copolymers. 35. Photophysical and rheological studies of the copolymer of methacrylic acid with 2-(1-naphthylacetyl)ethyl acrylate. Macromolecules, **23**, 3124–3129 (1990).

[22] Li C., Meng L. Z., Lu X. J., Wu Z. Q., Zhang L. F., He Y. B.: Thermo- and pH-sensitivities of thiosemicarbazone-incorporated, fluorescent and amphiphilic poly(N-isopropylacrylamide). Macromolecular Chemistry and Physics, **206**, 1870–1877 (2005).

[23] Fox M. A., Thompson H. W.: Synthesis and photophysical characterization of group transfer polymers with pendent aryl chromophores. Macromolecules, **30,** 7391–7396 (1997).

[24] Buhlmann P., Nishizawa S., Xiao K., Umezawa Y.: Strong hydrogen bond-mediated complexation of H_2PO_4(by neutral bis-thiourea hosts. Tetrahedron, **53**, 1647–1654 (1997).

[25] Kramer M. C., Welch C. G., Steger J. R., McCormick C. L.: Water-soluble copolymers. 63. rheological and photophysical studies on the associative properties of pyrene-labeled poly[acrylamide-co-sodium 11-(acrylamido)undecanoate]. Macromolecules, **28**, 5248–5254 (1995).

eXPRESS Polymer Letters Vol.1, No.6 (2007) 364–369
Available online at www.expresspolymlett.com
DOI: 10.3144/expresspolymlett.2007.51

Performance of epoxy-nanocomposite under corrosive environment

N. Abacha[*], *M. Kubouchi, K. Tsuda, T. Sakai*

Tsuda & Kubouchi Laboratory, Department of Chemical Engineering, Tokyo Institute of Technology, 2-12-1-S1-17 O-okayama, Meguro-ku, Tokyo 152-8552, Japan

Received 17 March 2007; accepted in revised form 9 May 2007

Abstract. Nanocomposite materials consisting of polymeric matrix materials and natural or synthetic layered minerals like clay are currently an expanding field of study because these new materials often exhibit a wide range of improved properties over their unmodified starting polymers. Epoxy/organoclay nanocomposites have been prepared by intercalating epoxy into the organoclay via direct mixing process. The clay exfoliation was monitored by X-ray diffraction (XRD) and transmission electron microscopy (TEM). Water diffusion and sulfuric acid corrosion resistance of epoxy-based nanocomposites were evaluated. Diffusion was studied through epoxy samples containing up to 6 phr (parts per hundred resin) of an organically treated montmorillonite. The diffusion of the environmental solution was measured by noting the increase in weight of the samples as a function of immersion time in these solutions at 80°C. The effect of the degree of exfoliation of the organoclay on water barrier and corrosion resistance was specifically studied. The data have been compared to those obtained from the neat epoxy resin to evaluate the diffusion properties of the nanocomposites. The flexural strength of the epoxy/organoclay nanocomposites samples made was examined to compare their mechanical performance under corrosive conditions as a function of immersion time and temperature. It was found, that the organoclay was mainly intercalated with some exfoliation and that addition of the organoclay yields better flexural strength retention under immersion into sulfuric acid.

Keywords: *thermosetting resins, diffusion, nanocomposite, acid aging*

1. Introduction

The research on polymer-layered silicate nanocomposites is currently an expanding field of investigation, this is mainly due to the large potential to achieve property enhancement significantly greater than that attainable using conventional fillers or polymers blends [1–3].

Understanding and controlling the various factors that govern the making of exfoliated thermoset/layered silicate nanocomposite is rather complex, several research projects have focused and made contribution to understand some of these issues [4–6]. Nanocomposites have the ability and the potential to reduce the permeability of polymer composites against ingress of corrosive substances. The reduction in permeability that can be attained from the exfoliation of layered silicates into polymers depends on the permeating agent being investigated. Few studies have been carried up to now on the effect of moisture on the barrier properties of nanocomposites [7–9], although very limited studies have treated the corrosive environment on the nanocomposites.

Epoxy based thermosetting polymer resins are widely used in the industry due to their superior characteristics such as good mechanical properties, and good resistance to chemicals. Significant use of epoxy resins as the matrix material in fiber reinforced composites, for the application in the aero-

---

[*] Corresponding author, e-mail: abacha@chemeng.titech.ac.jp

space and automotive industry [10–12]. However, such composites are highly susceptible to environmental conditions, primarily due to the degradation of epoxy matrix [8, 10, 11].

In our laboratory, epoxy/layered silicate nanocomposite has been developed, and the effects on the morphology development and properties have been investigated. The characterization of the environmental degradation (immersion in water or in sulfuric acid) under temperature of 80°C was focused on. It is expected that the addition of organoclay could increase the life service time by offering a barrier to water/ acid transportation.

2. Experiments

2.1. Materials and sample preparation

Bisphenol A type Epoxy Epomik R140 from Mitsui Chemical Co., Ltd was used as the matrix; Jeffamine D230 a diamine curing agent from Huntsman Co., and the organoclays used was the Nanomer I.28E from Nanocor Inc.

The organoclay was swelled with the curing agent and mixed with a mechanical stirrer at 1500 rpm for 1 h at 60°C, followed by ultra-sonication for an additional 1 h. After this, epoxy resin was added. Prior to curing, a degassing under vacuum was applied. Curing was done in two stages first at 70°C for 6 h followed by a post cure at 110°C for an additional 6 h. The load of the clay was varied from 0.5 to 6 phr (parts per hundred resin).

2.2. Characterization

X-Ray diffraction (XRD) was performed on a Philips Xpert MPD PW3050 X-ray diffractometer with a CuKα as a radiation source ($\lambda = 1.54$), operated at 40 kV and 30 mA. Samples were scanned at diffraction angles (2θ's) from 2° to 10° at a scan speed of 0.016°/s.

Transmission Electron microscope (TEM) photographs were taken with a JEOL JEM 2010F using an acceleration voltage of 200 kV.

The penetration depth of the sulfur (S) element was monitored using the coupled Scanning Electron Microscopy (SEM)/Energy dispersive X-ray spectrometer (EDS) JEOL JSM-5310LV analysis of the cross section of the immersed samples in sulfuric acid. Bending test was done according to ASTM D790 with Shimadzu Autograph AGS-1KNJ machine.

2.3. Measurement of weight change

The mass uptake of samples having dimension 60×25×2 mm immersed in deionized water and 10 mass% sulfuric acid medium separately at 80°C using constant temperature bath, was measured by recording the amount of the solution absorbed within a fixed interval of immersion time.

Before immersion all samples were dried at 60°C for 50 h and their initial weights and dimensions were measured. The specimens were periodically removed, wiped with filter paper to remove excess solution, and then were kept for 1h at room temperature before their weights – wet condition – were taken. Solution content was determined using Equation (1):

$$M_t\,[\%] = \frac{W_t - W_0}{W_0} \cdot 100 \qquad (1)$$

where M_t, W_t and W_0 are the solution content at a given time, weight of the sample at the time of the measurement and initial weight, respectively.

3. Results and discussion

3.1. Nanocomposite morphology

Figure 1 illustrates the XRD spectrum of the pristine organoclay and that of the epoxy/organoclay nanocomposite with different clay content. The basal spacing of the pristine organoclay was about 24.18 Å presented as a single peak around $2\theta = 3.65°$. This peak was shifted to lower value when mixed with the epoxy to form the nanocomposite materials. This was an indication that epoxy

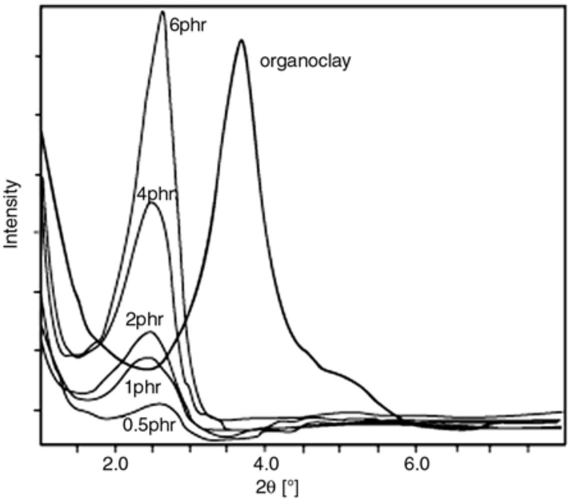

Figure 1. XRD spectrum of the different formulations

was intercalated between the layers of clay during mixing, which eventually expands or exfoliates the clay layers; the d-spacing was shifted from the original value of 24.18 Å to that around 34 Å.

By XRD, the formed nanocomposite simply would be defined as intercalated, in that there was an observed increase in the d-spacing as compared to the original clay d-spacing.

It also is observed that the higher the clay contents the higher the peak area. This is attributed to the high concentration of the organoclay that may agglomerate within the matrix and thus become difficult to disperse and to exfoliate within epoxy resin.

TEM images of the sample containing 1 phr organoclay are shown in Figures 2a and 2b, where the dark lines are the cross section of silicate, it reveals that although there were intercalated multilayer crystalline present, single exfoliated silicate layers were also prevalent. At low TEM magnification Figure 2a micrograph showed that the clay was well dispersed throughout the polymer with some agglomeration. Higher magnification (Figure 2b) showed that regions where both intercalated and exfoliated structures existed and regions were both intercalated tactoids and a few individual layers were present. Hence, the designation of an intercalated/exfoliated type of nanocomposite is recognized as already noted in XRD analysis.

This to conclude that achieving a full exfoliation with this material is quite difficult, and to reach an optimum one must try different ways and combinations of mixing.

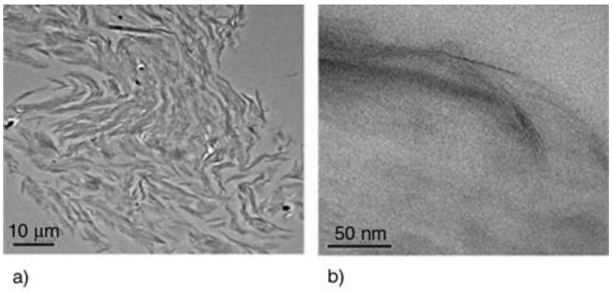

Figure 2. TEM micrograph of 1phr epoxy/organoclay nanocomposite at different magnification: a) low magnification, b) high magnification

3.2. Diffusion test

Materials (neat epoxy or epoxy/organoclay nanocomposite) immersed into water or into sulfuric acid at 80°C, gained mass due to the environmental solution uptake, as shown in Figures 3 and 4 for water and sulfuric acid respectively. The weight gain (M_t) over the equilibrium weight gain (M_∞) as a function of root time per specimen thickness ($t^{1/2}/l$); increased approximately linearly before saturation occurred.

The equilibrium mass uptake for neat epoxy was around 3% for immersion in water and around 18% for immersion in sulfuric acid. Obviously the mass uptake in acid is much higher than that in water due to the formation of a tertiary amine salt amine group [13], when all the amines in the resin are converted to amine salt, the weight gain reaches the equilibrium level [14].

In the case of water diffusion, no real performance of the added organoclay was found and similar trend is obtained as illustrated in Figure 3 the equilibrium mass uptake remains within the same value as for neat epoxy. It was expected that the incorporation of the organoclay increases the tortuosity path and thus decreases the equilibrium mass uptake, however, this was not the case, this may be explained by the fact that the organoclay was not fully exfoliated, and was rather intercalated with some agglomeration. Another important factor that could play an important role is that the organoclay may have kept some of its naturally hydrophilic characteristic and thus still attract water. Finally the presence of micro voids due to the increase in viscosity when mixing the organoclay. The free pore volume can easily take up the solvent molecules and increases the mass uptake.

Some authors find similar trend as in the case of Lan and Pinnavaia [3], Massam and Pinnavaia [15] and Becker *et al.* [12] where they found in their

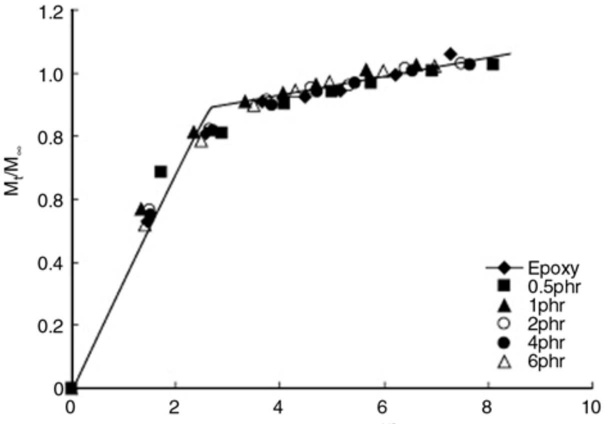

Figure 3. Weight gain in water as function of immersion square root time

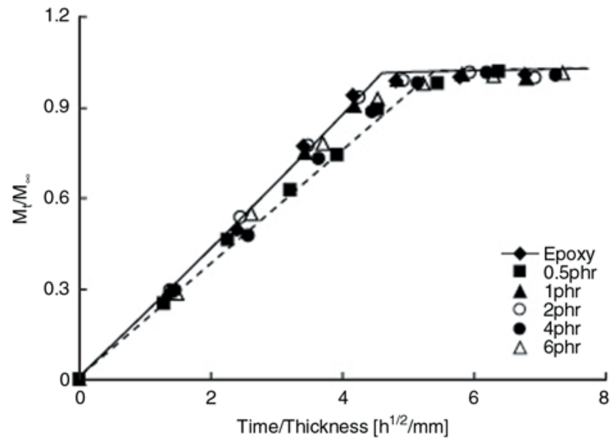

Figure 4. Weight gain in sulfuric acid as function of immersion square root time

studies concerning epoxy nanocomposite performance towards water and other organic solvent; that only the rate of absorption was reduced, and that the equilibrium water uptake was found to be relatively higher in the case of epoxy clay nanocomposite. The equilibrium moisture uptake was found to increase with the amount of layered silicate added.

It is suggested a dual effect between the benefit of adding high aspect ratio filler as a barrier properties enhancement to the above cited counter performance reasons i. e. not fully exfoliated, agglomeration, voids… etc.

On the other hand, for the case of acid uptake, a similar tendency was also obtained for neat epoxy and epoxy organoclay nanocomposite that is a linear increase as function of square root immersion time; however, lower values were obtained for the organoclay content of 0.5 phr as observed in Figure 4. At low organoclay content, better barrier properties performance was obtained, for the reason that the degree of exfoliation is higher with better dispersion and no agglomeration, it estimated that the tortuous path model appear to hold well only at very low clay loadings (<1 wt%) with significant deviations at higher loadings (1 to 5 wt%) and with change in humidity and temperature [16].

Acids diffuse quite easily into amine cured epoxy resin. The reaction between the resin and the penetrating acid cannot be excluded as already explained. The acid corrosivities are dependent rather on the chemical reaction running between the acid and the epoxy chain. These chemical reactions run in parallel with a purely physical diffusion processes.

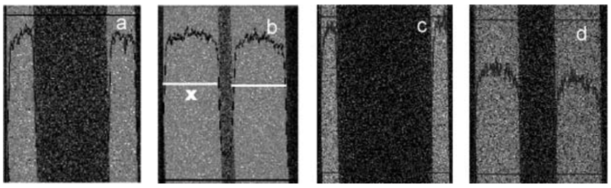

Figure 5. Example of EDS micrograph for S element detection at different immersion time: a) epoxy at 8 h, b) epoxy at 50 h, c) 0.5 phr at 8 h and d) 0.5 phr at 50 h

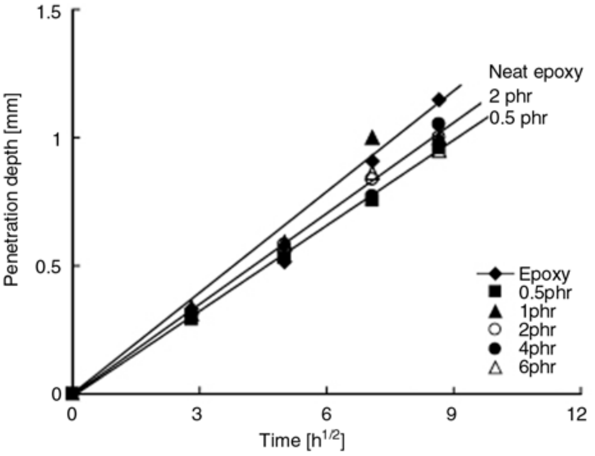

Figure 6. Sulfuric acid penetration depth as function of square root immersion time

To confirm the penetration of sulfur, observation with SEM/EDS was performed, it enabled to measure the penetration depth of the sulfuric acid by detection of the element S. Typical curves of the EDS micrographs are illustrated in Figure 5 where the dark line expresses the profile of the element S along to depth from surface, the penetration depth was calculated to be the distance from surface to level off the profile (*x* in Figure 5b).

Figure 6 shows the penetration depth as function of square root time, it is clearly observed the decrease of the penetration depth as organoclay was added to the epoxy system, the marked decrease was obtained as expected with 0.5 phr, however, all samples were fully penetrated within a short time around 120 hours which is considered too fast for protecting or coating application.

3.3. Mechanical properties

Three point bending test was performed for specimen under wet conditions, an average of three test samples were taken. Figure 7 illustrates the flexural strength of the initial value of the nanocomposite as function of the organoclay content. Flexural strength was relatively decreased as compared to

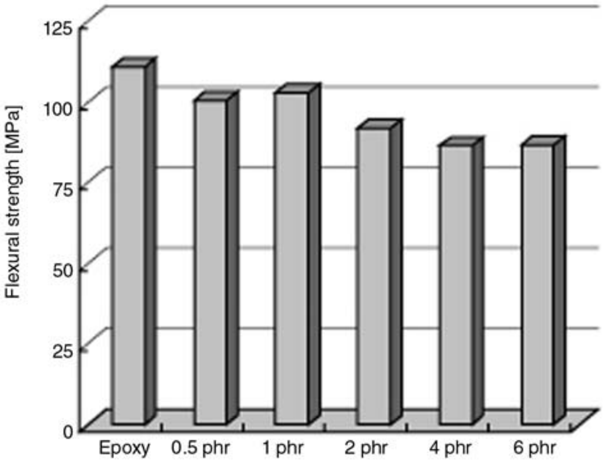

Figure 7. Flexural strength of the different formulation

the neat epoxy resin, this may be a result of the agglomeration effect of the organoclay within the epoxy matrix; making the distribution of the particles in the matrix an important factor to be considered in this case. It is known that the stress distribution around the particles increases the stress concentration of the propagating crack, which in turn induces relative early failure. The important parameter that affects this property is the quality of the interface in the composite that is the adhesive strength and the interfacial stiffness of the composite medium. These two factors play a crucial role in stress transfer and the elastic deformation from the matrix to the fillers [17].

The retention of the flexural strength as function of the immersion time is illustrated in the Figures 8 and 9 for water and acid respectively in wet condition, a decrease followed by a level off is observed as function of immersion time. This decrease is more expressed for the neat epoxy than in the case of the epoxy-clay nanocomposite. When organoclay was added the percent decrease of both modulus and flexural strength is more retained. The decrease is mainly due to the formation as already discussed of the tertiary ammonium salt consequently sever distortion is produced around the amine salt and the stability of the C–N bond decreases, causing the scission of the bonds and the decrease in the strength [14], however, when the organoclay is added, this distortion may be obstructed by its presence, even though deeper analysis of the chemical reaction that might occur must be performed.

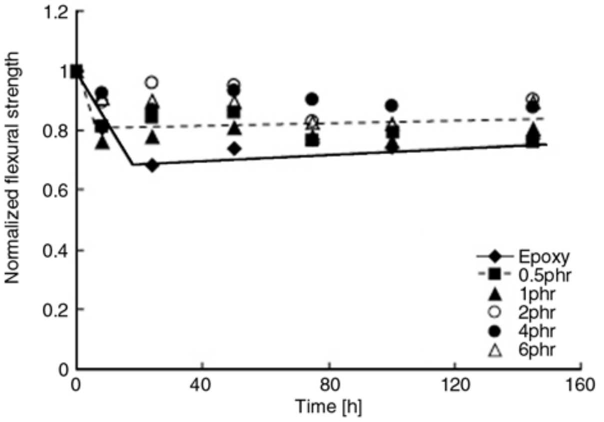

Figure 8. Normalized flexural strength of specimen immersed in water (wet condition)

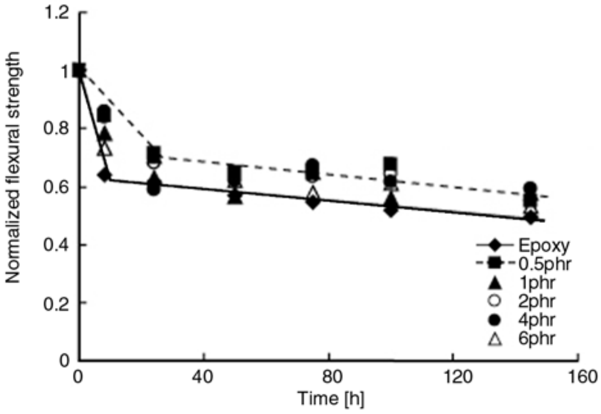

Figure 9. Normalized flexural strength of specimen immersed in sulfuric acid (wet condition)

4. Conclusions

A number of observations and conclusions can be drawn from this investigation:

The materials prepared were found to have inhomogeneous degree of exfoliation with rather high degree of intercalation. Under the present processing conditions, the additions of the organoclay can significantly improve the barrier properties against corrosive acid. When immersed in water the absorption parameter seems to be unaffected by the presence of the clay, this seems to be related to the fact that results of sorption are not very sensitive to the extent of filler exfoliation when the diffusing media i. e. water is strongly absorbed by the filler surface. Addition of clay leads to better mechanical properties at wet conditions.

References

[1] Usiki A., Kojima Y., Kawasumi M., Okada A., Fukushima Y., Kurauchi T., Kamigait, O.: Synthesis of nylon 6 clay hybrid. Journal of Materials Research, **8**, 1179–1184 (1993).

[2] Wang M. S., Pinnavaia T. J.: Clay-polymer nanocomposites formed from acidic derivatives of montmorillonite and an epoxy resin. Chemistry of Materials, **6**, 468–474 (1994).

[3] Lan T., Pinnavaia T. J.: Clay-reinforced epoxy nanocomposites. Chemistry of Materials, **6**, 2216–2219 (1994).

[4] Balabanovich A. I., Hornung A., Merz D., Seifert H.: The effect of a curing agent on the thermal degradation of fire retardant brominated epoxy resins. Polymer Degradation and Stability, **85**, 713–723 (2004).

[5] Zanetti M., Lomakin L. S., Camino G.: Polymer layered silicate nanocomposites. Macromolecular Materials and Engineering, **279**, 1–9 (2000).

[6] Zilg C., Thomann R., Finter J., Mülhaupt R.: The influence of silicate modification and compatibilizers on mechanical properties and morphology of anhydride-cured epoxy nanocomposites. Macromolecular Materials and Engineering, **280**, 41–46 (2000).

[7] Shah A. P., Gupta R. K., Gangarao H. V. S., Powell C. E.: Moisture diffusion through vinyl ester nanocomposites made with montmorillonite clay. Polymer Engineering and Science, **42**, 1852–1863 (2002).

[8] Kim J-K., Hu C., Woo R. S, Sham M-L.: Moisture barrier characteristics of organoclay-epoxy nanocomposites. Composites Science and Technology, **65**, 805–813 (2005).

[9] Rana H. T., Gupta R. K., GangaRao H. V. S., Sridhar L. N.: Measurement of moisture diffusivity through layered-silicate nanocomposites, AICHE Journal, **51**, 3249–3256 (2005).

[10] GangaRao H. V. S., Craigo C.: Fiber-reinforced composite bridge decks in the USA. IABSE Structural Engineering International, **9**, 286–288 (1999).

[11] Kshirsagar S., Lopez-Anido R. A., Gupta R. K.: Environmental aging of fiber-reinforced polymer-wrapped concrete cylinders. ACI Materials Journal, **97**, 703–715 (2000).

[12] Becker O., Cheng Y-B., Varley R. J., Simon G P.: Layered silicate nanocomposites based on various high-functionality epoxy resins: the influence of cure temperature on morphology, mechanical properties, and free volume. Macromolecules, **36**, 1616–1625 (2003).

[13] Ono S., Tsuda K., Kubouchi M., Nishiyama T., Hojo H.: Degradation behavior of amine cured epoxy resin and FRP in acid solutions. in ‘Proceeding of the Tenth International Conference on composite materials, Whistler, Canada’ Vol.**4**, 215–222 (1995).

[14] Tsuda K., Kubouchi M.: Decomposition of polymeric materials. Corrosion Engineering, **44**, 141–154 (1995).

[15] Massam J., Pinnavaia T. J.: Nanostructured powders and their industrial applications. Material Research Society Symposia Proceedings, **520**, 223–232 (1998).

[16] Powell C. E., Beall G. W.: Physical properties of polymer/clay nanocomposites. Current Opinion in Solid State and Materials Science, **10**, 73–80 (2006).

[17] Mohan T. P., Kumar M. R., Velmurugan R.: Mechanical and barrier properties of epoxy polymer filled with nanolayered silicate clay particles, Journal of Materials Science, **41**, 2929–2937 (2006).

eXPRESS Polymer Letters Vol.1, No.6 (2007) 370–377
Available online at www.expresspolymlett.com
DOI: 10.3144/expresspolymlett.2007.52

Morphology and thermal behaviour of SAN/EPDM blends

A. Ptiček[1], *Z. Hrnjak-Murgić*[1*], *J. Jelenčić*[1], *M. Mlinac-Mišak*[2]

[1]Faculty of Chemical Engineering and Technology, Marulićev trg 19, University of Zagreb, P.O. Box 177, HR-10000, Croatia
[2]DIOKI d.d., Žitnjak bb, Zagreb, HR-10000, Croatia

Received 20 March 2007; accepted in revised form 9 May 2007

Abstract. Blends of styrene-acrylonitrile (SAN) with ethylene-propylene-diene (EPDM) with and without high impact polystyrene (HIPS) as a compatibilizer were studied. One series of blends was prepared in composition 95/5, 90/10, 85/15, 80/20 and 60/40; and the second series of blends was prepared with the addition of 5 wt% of HIPS. Their morphology and thermal behaviour were inspected by scanning electronic microscopy (SEM) and dynamic mechanic analysis (DMA), respectively. Further on, blends were separated to their components by Soxhlet extraction in selective solvent and characterized by Fourier Transform Infrared Spectroscopy (FTIR) and gel permeation chromatography (GPC), respectively. The results of morphological observations revealed that the addition of a small percentage of compatibilizer decreases the domain size of the dispersed phase and the compatibility of the blends was enhanced. The shifts of values of glass temperatures (T_g) in the examined blends also indicate that with addition of compatibilizer HIPS miscibility between SAN and EPDM is improved.

Keywords: *polymer blends and alloys, thermal properties, morphology*

---

1. Introduction

Blending of styrene-acrylonitrile and ethylene-propylene-diene rubber may provide an efficient way with tailored properties. Styrene-acrylonitrile/ethylene-propylene-diene rubber (SAN/EPDM) system is a brittle/ductile combination but the blend does not result in a toughened plastic, given that two components are immiscible at the molecular level because if their difference in polarity and blends have poor mechanical properties compared to those of their neat components. The ability of rubber to improve the mechanical properties of glassy polymers depends mostly on the dispersed rubber particle size that implies compatibility of the rubber phase with the matrix [1]. Therefore, the introduction of a small amount of compatibilizer has been investigated to obtain more desirable properties. A compatibilizer can be made either separately and then added to a polymer blend or created *in situ* during the blending process [2, 3]. The first method has the advantage of better controlling the molecular architecture of the compatibilizer. The second method, often called reactive extrusion or reactive compatibilization, allows us to generate the compatibilizer *in situ* at the interfaces directly during blending [4, 5]. System called acrylonitrile-ethylene/propylene/diene elastomer-styrene (AES), which is formed by EPDM rubber dispersed into a glassy matrix of a SAN copolymer, containing also SAN molecules grafted onto the EPDM rubber (EPDM-g-SAN) which act as compatibilizing agents between the two immiscible components [6, 7]. Generally, the rubbery particles are grafted by a brittle polymer which is the same as the matrix. These grafted chains enhance the interfacial bonding between the rubbery particles and the brittle matrix, and also make the rubbery particles dis-

---

[*]Corresponding author, e-mail: zhrnjak@marie.fkit.hr

perse throughout in the matrix polymer to match the thermodynamic parameters. Elastomer-modified thermoplastic high impact polystyrene (HIPS) is one of the oldest styrenic polymers and provides a good balance between rigidity and elasticity and it is often used as a compatibilizer. Many authors have observed that some of the most important factors in controlling the mechanical properties of various styrene copolymers (like SAN and acrylonitrile-butadiene-styrene, ABS) and HIPS are rubber particle size [8, 9] and the volume fraction of the rubbery phase [10, 11]. In this study, we investigate the effect of high impact polystyrene as compatibilizer and *in situ* formed graft copolymer on the morphology and thermal properties of blends. SAN/EPDM and SAN/EPDM/HIPS blends with different fractions of the elastomer component were processed by extrusion resulting in polymer materials of different microstructures.

2. Experimental

2.1. Materials

Studied blends were prepared with ethylene-propylene-diene (EPDM, Keltan 312, DSM), containing 55 wt% ethylene and 4 wt% ethylidene norbornene, Mooney viscosity 36 MU and styrene-acrylonitrile (SAN, Tyril 790, The Dow Chemical Company) with 24 wt% AN, the melt flow rate (MFR, 220°C, 10 kg) was 27 g/10 min. The interfacial agent was high-impact polystyrene (PS-HI 417) supplied by DIOKI, (Croatia), with 8 wt% polybutadiene.

2.2. Preparation of samples

The extrusion process was carried out on a Haake Rheocord System 9000 twin-screw extruder (Haake, Karlsruhe, Germany), a co-rotating extruder with standard, non-intensive screw characteristics. Following temperatures have been chosen for the four heating zones (from hopper to die): 170/190/200/210°C and the screws rotation speed has been set to 60 rpm. Blends were injection moulded according to ISO 294 and dumbbell specimens were formed according to ISO 3167. Compositions of the studied blends are listed in Table 1.

Table 1. Composition of SAN/EPDM and SAN/EPDM/HIPS blends

Samples	SAN/EPDM					SAN/EPDM/HIPS				
SAN	95	90	85	80	60	95	90	85	80	60
EPDM	5	10	15	20	40	5	10	15	20	40
HIPS	–	–	–	–	–	5	5	5	5	5

2.3. Polymer blend separation

The prepared SAN/EPDM blends were separated to components by successive extraction in selective solvent for eight hours using Soxhlet method. To check the extraction efficiency, preliminary extractions have been made for 8, 24 and 48 hours. The styrene-acrylonitrile polymer is extracted in mixture of methanol/acetone (ratio 55:45 vol%), the EPDM polymer in hexane and the graft polymer is extracted in tetrahydrofurane (THF). The remaining part of the blend was considered as the gel content.

2.4. Gel permeation chromatography (GPC)

The molecular masses and their distributions ($\overline{M}_n$, $\overline{M}_w$) of extracted polymers were determined by the gel permeation chromatography (GPC) carried out on the PL-GPC 20 Polymer Laboratories instrument fitted with RI detector. Tetrahydrofuran was used as a solvent (c = 10 mg/5 ml). Molecular masses were calculated as polystyrene equivalents.

2.5. FTIR measurements

FTIR spectra of extracted polymers were recorded on Perkin Elmer Spectrum One in the range of 4000 to 500 cm^{-1}, with a resolution of 4 cm^{-1}. All samples were prepared as thin films (0.1 mm) cast from 6 wt% toluene solution.

2.6. Scanning electron microscopy (SEM)

Morphologies of the studied blends were characterised from a cross-section of cryogenically fractured surfaces of injection moulded samples (2 mm thick) using a Philips XL 30 Scanning Electron Microscope. Samples were immersed in liquid nitrogen for more than 15 min to cool down and then fractured immediately. The dried samples were sputter-coated with gold prior to scanning electron microscopy (SEM) examination.

2.7. DMA measurements

Dynamical mechanical properties of the blends were analyzed using a DMA Q 800 TA Instruments. Specimens for the dynamic mechanical test were cut into 50×10×1 mm. The glass transition temperatures (T_{g1} and T_{g2}) of the samples were measured at a frequency of 1 Hz with the temperature ranging from –100 to +150°C and a temperature rate of 10°C/min. After the testing at a particular temperature the samples were cooled to –100°C in nitrogen atmosphere.

3. Results and discussion

3.1. Analysis of polymer fractions in blends

To elucidate the extrusion process, reactions and interactions that are established [12–16], the separation of SAN/EPDM blends on its components was carried out by selective solvent extraction and the results are presented in Figure 1. Significant differences in the fractions of graft copolymer (EPDM-g-SAN), SAN polymer, EPDM polymer and gel were observed. The most significant component formed during extrusion is the graft copolymer, Figure 2, and it is expected to improve compatibility of two polymer phases in SAN/ EPDM blends. The increase of the ratio of formed graft copolymer in blends can be explained by the fact that increasing reaction temperature favours the

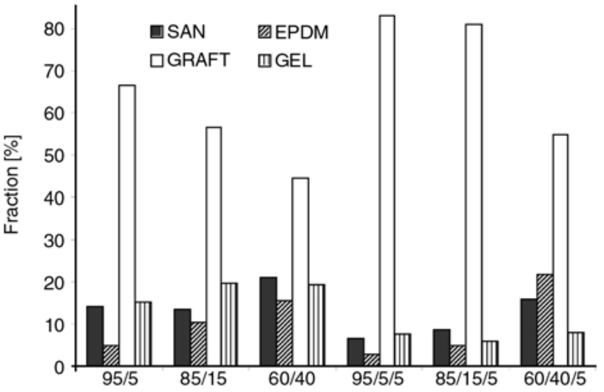

Figure 1. Fraction of extracted components: SAN, EPDM, graft polymer and gel from extruded SAN/EPDM blends processed without and with HIPS compatibilizer

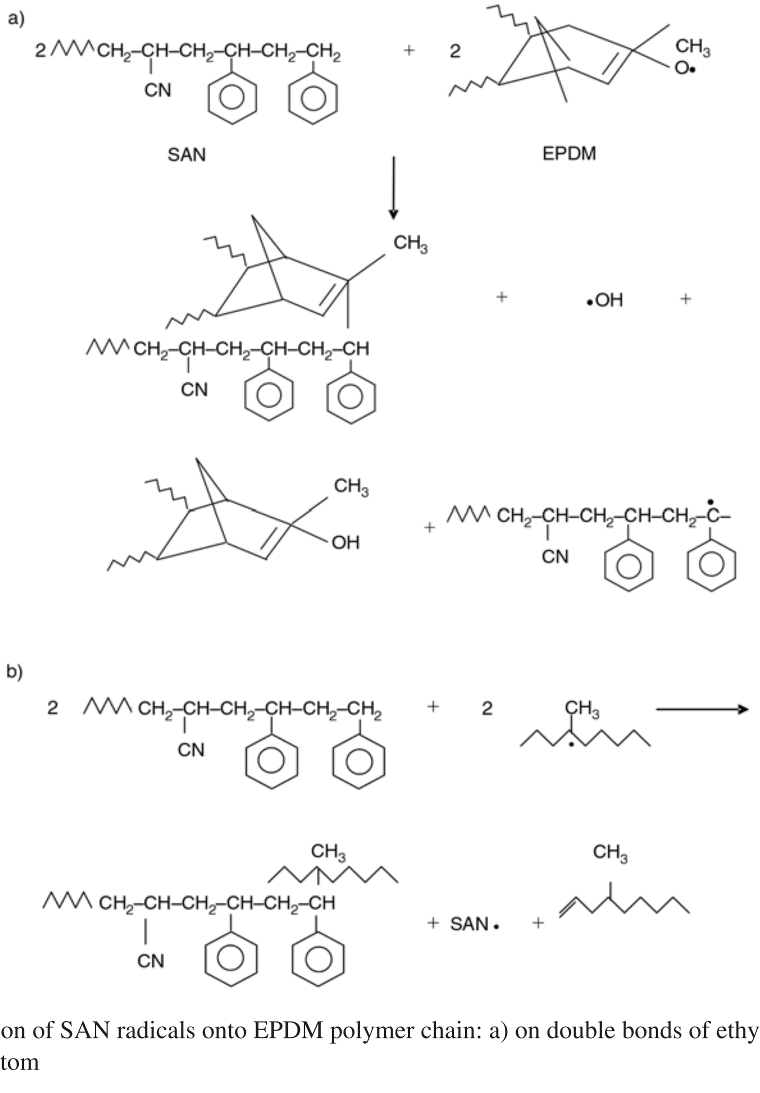

Figure 2. Grafting reaction of SAN radicals onto EPDM polymer chain: a) on double bonds of ethylidene norbornene, b) on tertiary C-atom

formation of polymer radicals and increases their mobility. Such chemical bonding improved compatibility in the blends and prevented further degradation of the polymer during the extrusion process [17]. Significantly higher concentration of graft copolymers is observed when the compatibilizer HIPS is present in the blends. From the results, Figure 1, it is observed that fraction of formed graft is in the interval of 45–68 wt% for samples prepared without compatibilizer while the fraction of formed grafts for samples with compatibilizer is 58–80 wt%. It is assumed that the high concentration of polymer radicals is present due to presence of double bonds of butadiene. Low concentration of SAN polymer obtained after extraction confirms that the most of SAN radicals participate in grafting or in crosslinking reaction. Formation of polymer radicals is also confirmed by the changes of molecular masses of blends components, see Figure 3. Molecular masses (M_n, M_w) of SAN polymer obtained after extrusion process are slightly increased, which indicates chemical bonding of SAN radicals between themselves. Changes of molecular masses of SAN matrix can significantly affect compatibility of blends, i. e. higher molecular masses would increase viscosity of matrix and that leads to finer morphology and better compatibility in blends [18]. The molecular masses of extracted EPDM from blends samples are slightly changed showing higher stability under process conditions, Figure 3. It is also known from the literature, EPDM rubber is more stable than SAN copolymer at higher temperatures (200°C) [19]. Further on, the values of molecular masses of the formed graft copolymers are approximately the same as those as SAN polymer because the high fraction of SAN polymer is present. On the other hand, crosslinking reaction results in the formation of a gel, which is present in higher concentration in blends prepared without HIPS and it will contribute to incompatibility of polymers in the blends.

Results of distribution of molecular masses of extracted SAN and EPDM-g-SAN components are shown in Figures 4 and 5. Comparing the differential curves of SAN polymer extracted from blend composition 95/5, Figure 4a, and curves of SAN extracted from blend composition 95/5/5, Figure 4b, it can be seen that there are significant changes in the distribution of molecular masses. Broad distribution of molecular masses indicates presence of newly formed SAN polymer chains of lower molecular masses denoting higher polydispersity of the system. On the other hand, narrow distribution of molecular masses means participating of SAN polymer in grafting reactions, which is supported by the results of higher fraction of graft copolymer, Figure 1. The similar behaviour of distribution of molecular masses of the extracted EPDM-g-SAN graft copolymer in the considered samples is observed, Figure 5.

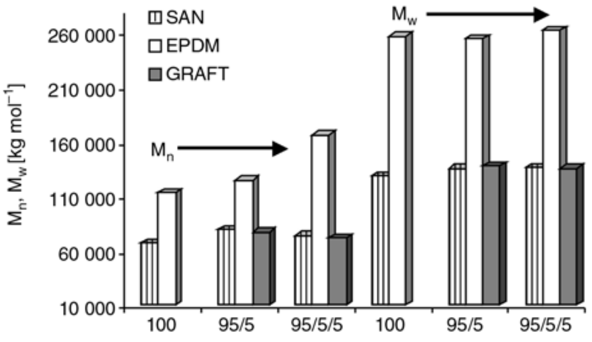

Figure 3. Number molecular masses, and weight molecular masses, of extracted SAN, EPDM and graft polymer from extruded SAN/EPDM blends and molecular masses of commercial SAN polymer and EPDM polymer

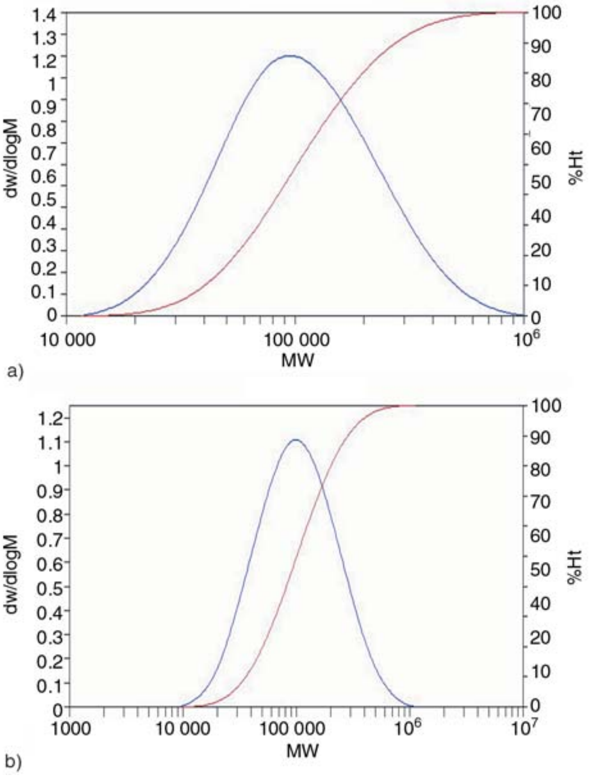

Figure 4. Integral and differential curves for the SAN polymer: a) SAN polymer extracted from SAN/EPDM blend composition 95/5, b) SAN polymer extracted from SAN/EPDM/HIPS blend composition 95/5/5

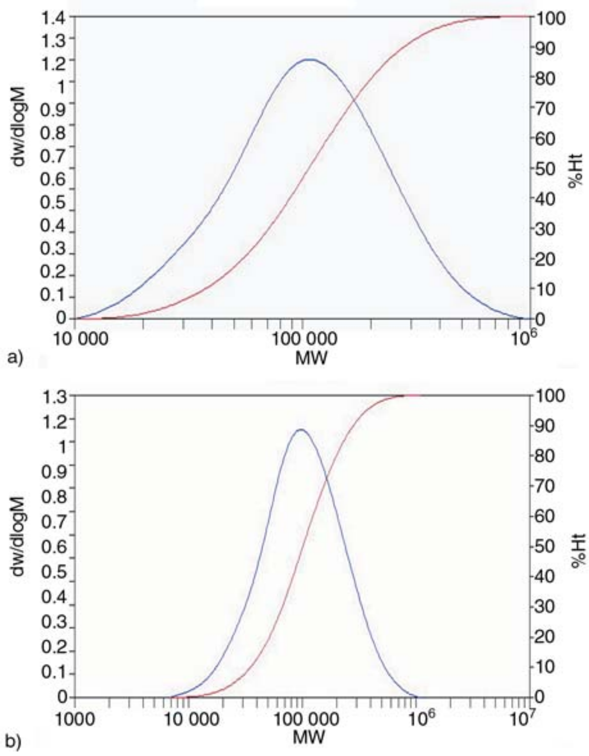

Figure 5. Integral and differential curves for the EPDM-g-SAN graft copolymer: a) graft copolymer extracted from SAN/EPDM blend composition 95/5, b) graft copolymer extracted from SAN/EPDM/HIPS blend composition 95/5/5

3.2. FTIR analysis

The structure of the EPDM-g-SAN graft copolymer was determined from FTIR spectra, as is shown in Figure 6. The characteristic absorption bands of EPDM rubber appeared at 722 cm^{-1} corresponding –(CH_2)– stretching and at 1374 cm^{-1} due to –C–CH_3 stretching; for SAN copolymer vibrations at 2237 cm^{-1} due to –CN groups and the vibrations at 1453 and 1493 cm^{-1} corresponding to aromatic ring were observed. On the other hand, graft copolymer, reveals characteristic vibrations of both SAN and EPDM polymers which indicate grafting reaction that appear during processing [20].

3.3. Dynamical mechanical analysis

Measurement of the glass transition temperatures T_g, were used to study miscibility of SAN/EPDM systems because the difference in the T_g values of EPDM and SAN was sufficiently large. There are two distinct glass transitions for all blends, in our case the lower glass transition is due to the EPDM phase (–50°C) and the higher glass transition (109°C) is due to the SAN phase (21–23). Table 2 contains the T_g values for EPDM, SAN and their blends with and without HIPS as a compatibilizer. From inspection of Table 2 it can be seen that with adding HIPS to the SAN/EPDM blends, the T_g values of EPDM phase shifts to –40°C, significantly higher values after addition of 5% HIPS, whereas that of the SAN phase moves to 104°C, a lower temperature, at HIPS content of also 5%. For the blends prepared with compatibilizer and with higher fraction of elastomer, slight shift of T_g values is observed. Meanwhile, the results do not reveal a new peak which would correspond to the HIPS phase. This means that a new isolated phase in SAN/EPDM blend was not formed and it is assumed that HIPS is located at the boundaries between SAN and EPDM [24]. From these results it can be concluded that by adding HIPS in SAN/EPDM blends glass transition becomes less distinct, indicating better interaction and the increasing compatibility between the SAN and EPDM polymers.

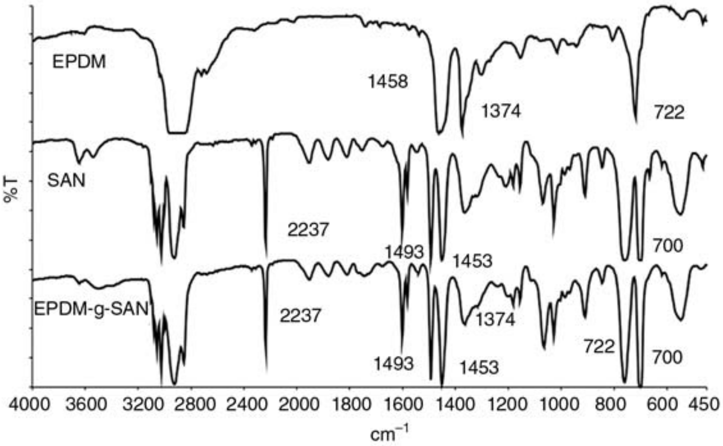

Figure 6. FTIR spectra of extracted SAN, EPDM and graft copolymer from extruded SAN/EPDM blend

Table 2. Glass transition temperatures (T_{g1}, T_{g2}) obtained for SAN/EPDM, SAN/EPDM/HIPS blends and for pure SAN and EPDM polymers

SAN/EPDM	T_{g1} [°C]	T_{g2} [°C]	SAN/EPDM/HIPS	T_{g1} [°C]	T_{g2} [°C]
95/5	–48.2±0.1	104.6±0.1	95/5/5	–40.0±0.2	104.9±0.1
90/10	–47.2±0.2	105.3±0.2	90/10/5	–43.7±0.1	106.2±0.1
85/15	–50.3±0.1	105.0±0.3	85/15/5	–49.7±0.1	104.9±0.2
80/20	–51.0±0.2	105.0±0.1	80/20/5	–49.2±0.2	104.6±0.1
60/40	–51.3±0.2	106.1±0.1	60/40/5	–49.0±0.1	106.1±0.2
EPDM	–50.0±0.2	–	SAN	–	109.0±0.1

3.4. Morphology of the blends

The micrographs of the cryogenically fractured surfaces of the SAN/EPDM blends compositions 95/5, 85/15, 60/40 are displayed in Figure 7. The inspection of these micrographs indicates two phases with different domain size and shape. As is well known from the literature [25], polymer present in the lower concentration usually forms a discontinuous phase whereas the polymer present in the higher concentration forms continuous phase and such morphology of blends is usually named a particle-in-matrix type. Finer morphology can be observed with lower concentration of EPDM, Figure 7a, in comparison with morphology of blends with higher concentration of EPDM, Figure 7b and 7c. The high interfacial tension between the SAN and EPDM phases leads to a larger size of the dispersed rubber phase (3.4 μm) as is well seen on Figure 7b in comparison with particle size on micrograph Figure 7a, where the size of dispersed phase is 0.5 μm. If the particle size is greater than the critical value the blends will still be a brittle and incompatible. For example, the effective toughness occurs at an optimum particle size of 0.1–1 μm for SAN [26] and when the optimum particle size of dispersed EPDM is achieved, necessary levels of adhesion with the SAN matrix is provided and effective increase of impact toughness is achieved. However, as the ratio of two polymers in blend progress toward equality, co-continuous phase is formed, Figure 7c. Further, the particle size of dispersed phase on micrograph Figure 7c is significantly higher in comparison with particle size on micrographs Figure 7a and 7b. It can be seen that partial separation of two phases is present because block segments of EPDM do not adhere to SAN phase completely.

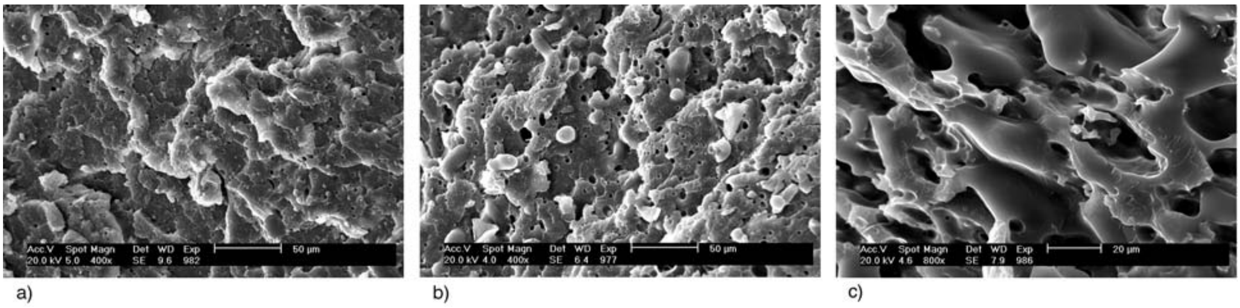

a) b) c)

Figure 7. SEM micrographs of fractured surface of SAN/EPDM blends of composition: a) 95/5, b) 85/15 and c) 60/40

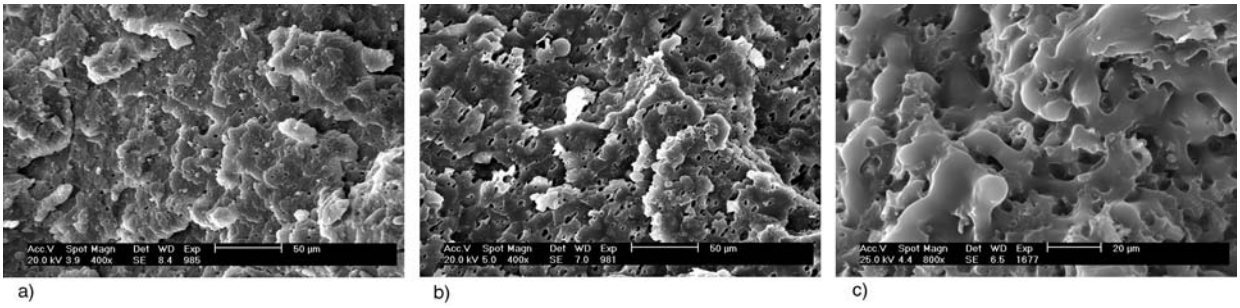

a) b) c)

Figure 8. SEM micrographs of fractured surface of SAN/EPDM/HIPS blend of composition: a) 95/5/5, b) 85/15/5 and c) 60/40/5

The compatibility of the SAN/EPDM system is improved by addition of HIPS as a compatibilizer as can be seen from micrographs in Figure 8. Especially finer morphology is observed for the samples prepared with compatibilizer, micrographs Figures 8b and 8c in comparison with the samples prepared without compatibilizer, micrographs Figures 7b and 7c. It was also seen that the size of the dispersed phase domain (EPDM) decreased with the addition of compatibilizer (2.1 μm), micrograph Figure 8b), no phase separation is present in the blend and the size distribution is more uniform. Such morphology could be also explained as result of the high fraction of the graft copolymer formed during the processing and there was a high degree of compatibility between the graft copolymer with the rubber particles and the matrix. The graft copolymer will be preferentially located at the interface resulting in better adhesion between the phases, thus reducing the interfacial tension and enhancing the adhesion. In other words, compatibilizers improved morphology and the compatibility of the blend due to reduction of the interfacial tension between phases, which comply with the many various theories from the literature [27–31].

4. Conclusions

High impact polystyrene, used as a compatibilizer significantly decreases the particle size of dispersed phase in SAN/EPDM polymer blends resulting in finer morphology and improved compatibility. Presence of compatibilizer was lead to the formation of a graft copolymer in high concentration during the processing of blends and such *in situ* formed graft makes an interphase between the two polymers as well as main component in bulk of blend. From the dynamic mechanic analysis of the blends, the glass transition temperature of the EPDM phase was increased from –50°C to –40°C, whereas that of the SAN phase was decreased from 109°C to 104°C with the addition of 5% of HIPS content indicating better adhesion of the phases.

References

[1] Shaw S., Singh R. P.: Studies on impact modification of polystyrene (PS) by ethylene-propylene-diene (EPDM) rubber and its graft copolymers. I. PS/EPDM and PS/EPDM-g-styrene blends. Journal of Applied Polymer Science, **40**, 685–692 (1990).

[2] Hoang T., Trung T., Yoo G., Ahn J. H., Zin W. C., Cho W. J., Ha C. S.: Compatibilizing of SAN/EPDM blends by grafting EPDM with methyl methacrylate. The Bulletin of the Korean Chemical Society, **22**, 1037–1040 (2001).

[3] Harrats C., Omonov T., Groeninckx G., Moldenaers P.: Phase morphology development and stabilization in polycyclohexylmethacrylate/polypropylene blends: uncompatibilized and reactively compatibilized blends using two reactive precursors. Polymer, **45**, 8115–8126 (2004).

[4] Baker W. E., Hu G. H., Scott C. E.: Reactive Polymer Blending. Hanser Publisher, Munich (2001).

[5] Charoensirisomboon P., Inoue T., Solomko S. I., Sigalov G. M., Weber M.: Morphology of compatibilized polymer blends in terms of particle size-asphericity map. Polymer, **41**, 7033–7042 (2000).

[6] Qu X., Shang S., Liu G., Zhang S., Zhang Y., Zhang L.: Effect of the addition of acrylonitrile/ethylene-propylene-diene monomer (EPDM)/styrene graft copolymer on the morphology-properties relationships in poly(styrene-co-acrylonitrile)/EPDM rubber blends. Journal of Applied Polymer Science, **91**, 1685–1697 (2004).

[7] Chiantore O., Guaita M., Lazzari M., Ravanetti G. P.: Thermal oxidative degradation of AES. Polymer Degradation and Stability, **47**, 141–148 (1995).

[8] Bucknall C. B.: Toughened Plastics. Applied Science Publisher, London (1977).

[9] Donald A. M., Kramer E. J.: Craze initiation and growth in high-impact polystyrene. Journal of Applied Polymer Science, **27**, 3729–3741 (1982).

[10] Bucknall C. B., Cote F. F. P., Partridge I. K.: Effects of rubber particle volume fraction on deformation and fracture in HIPS. Journal of Materials Science, **21**, 301–306 (1986).

[11] Bucknall C. B., Davies P., Partridge I. K.: Rubber toughening of plastics. X: Effects of rubber particle volume fraction of the kinetics of yielding in HIPS. Journal of Materials Science, **21**, 307–313 (1986).

[12] Pagnoulle C., Jerome R.: Particle-in-particle morphology for the dispersed phase formed in reactive compatibilization of SAN/EPDM blends. Polymer, **42**, 1893–1896 (2001).

[13] Chiantore O., Trossarelli L., Lazzari M.: Compatibilization effects in the thermal degradation of blends containing SAN and EPDM polymers. Polymer, **39**, 2777–2781 (1998).

[14] Hwang I. J., Lee M. H., Kim B. K.: Preparation and properties of SAN/EPDM/CPE ternary blends. European Polymer Journal, **34**, 671–675 (1998).

[15] Berzin F., Vergnes B., Delamare L.: Rheological behavior of controlled-rheology polypropylenes obtained by peroxide-promoted degradation during extrusion: Comparison between homopolymer and copolymer. Journal of Applied Polymer Science, **80**, 1243–1252 (2001).

[16] Hrnjak-Murgić Z., Kratofil L., Jelenčić J., Janović Z.: Reactive extrusion of SAN/EPDM blends. International Polymer Processing, **29**, 139–146 (2004).

[17] Thomas S., Groeninckx G.: Reactive compatibilisation of heterogeneous ethylene propylene rubber (EPM)/nylon 6 blends by the addition of compatibiliser precursor EPM-g-MA. Polymer, **40**, 5799–5819 (1999).

[18] Andradi L. N., Helmann G. P.: The percolation limits for two-phase blends of PMMA and copolymers of styrene and MMA. Polymer, **34**, 925–932 (1993).

[19] ver Strate G.: Ethylene-Propylene Elastomers. in 'Encyclopedia of Polymer Science and Engineering' (eds.: Mark H. F., Bikales N. M., Overberger C. G., Menges G.) Wiley Interscience Publication, New York, Vol **6**, 522–564 (1986).

[20] Hou L., Yang G.: Morphology and thermal behavior of MCPA6/SAN blends prepared by anionic ring-opening polymerization of ε-caprolactam. Journal of Applied Polymer Science, **100**, 1357–1363 (2006).

[21] Pandey K. N., Setua D. K., Mathur G. N.: Determination of the compatibility of NBR-EPDM blends by an ultrasonic technique, modulated DSC, dynamic mechanical analysis, and atomic force microscopy. Polymer Engineering and Science, **45**, 1265–1276 (2005).

[22] Chiu C-Y., Yen Y-J., Kuo S-W., Chen H-W., Chang F-C.: Complicated phase behavior and ionic conductivities of PVP-co-PMMA-based polymer electrolytes. Polymer, **48**, 1329–1342 (2007).

[23] Liau W. B., Tung S. H., Lai W. C., Yang L. Y.: Studies on blends of binary crystalline polymers: Miscibility and crystallization behavior in PBT/PAr (I27-T73). Polymer, **47**, 8380–8388 (2006).

[24] El-Sabbagh S. H.: Compatibility study of natural rubber and ethylene-propylene diene rubber blends. Polymer Testing, **22**, 93–100 (2003).

[25] Fox D. W., Allen R. B.: Compatibility. in: 'Encyclopedia of Polymer Science and Engineering' (eds.: Mark H. F., Bikales N. M., Overberger C. G., Menges G.) Wiley Interscience Publication, New York, Vol **3**, 758–774 (1985).

[26] Zeng Z., Wang L., Cai T., Zeng X.: Synthesis of high rubber styrene-EPDM-acrylonitrile graft copolymer and its toughening effect on SAN. Journal of Applied Polymer Science, **94**, 416–423 (2004).

[27] Anastasiadis S. H. Gancarz J., Koberstein J. K.: Compatibilizing effect of block copolymers added to the polymer/polymer interface. Macromolecules, **22**, 1449–1453 (1989).

[28] Teodorescu M., Dimonie M., Draghici C., Şerban S., Vasilievici G., Coleşa M.: Grafting styrene onto poly (vinyl acetate) by free radical chain transfer reactions. Reactive and Functional Polymers, **61**, 387–395 (2004).

[29] Li Y., Hu S., Sheng J.: Evolution of phase dimensions and interfacial morphology of polypropylene/polystyrene compatibilized blends during mixing. European Polymer Journal, **43**, 561–572 (2007).

[30] Ersoy O. G., Nugay N.: Combined effect of the nature of the filler and the compatibilizer on the weld line properties of filled blends. Composites Part A: Applied Science and Manufacturing, **38**, 162–173 (2007).

[31] Wang D., Xie X. M.: Novel strategy for ternary polymer blend compatibilization. Polymer, **47**, 7859–7863 (2006).

eXPRESS Polymer Letters Vol.1, No.6 (2007) 378–384
Available online at www.expresspolymlett.com
DOI: 10.3144/expresspolymlett.2007.53

Silane crosslinking of polyethylene: the effects of EVA, ATH and Sb_2O_3 on properties of the production in continuous grafting of LDPE

H. Azizi[*], *J. Barzin, J. Morshedian*

Iran Polymer and Petrochemical Institute, P.O.Box. 14965/115, Tehran, Iran

Received 31 January 2007; accepted in revised form 14 May 2007

Abstract. In this study, thermal, mechanical and fire retardant properties of silane-crosslinked low-density polyethylene (XLPE) containing ethylene-vinylacetate (EVA) copolymer, alumina trihydrate (ATH) and antimony trioxide (Sb_2O_3) have been studied. Samples were prepared in a single-screw extruder and the silane type was vinyltrimethoxy silane (VTMOS). Incorporation of ATH and Sb_2O_3 into polyethylene at sufficiently high loading introduces good fire retardancy expressed by limiting oxygen index (LOI). However, some tensile properties decreased. These limitations could be overcome by silane crosslinking. By incorporation of EVA into XLPE gel content increased and curing time decreased. Differential scanning calorimetric (DSC) analysis indicated the existence of two distinct melting endothermic peaks corresponding to two different crystalline phases. Results from mechanical properties showed that mechanical properties of XLPE/EVA blends improve by increasing EVA content up to 15 wt%.

Keywords: *material testing, polyethylene, silane croslinking, flame retardant, EVA*

1. Introduction

In many applications there is a need to improve the properties of polyethylene, in particular with respect to heat deformation resistance, but improvement in chemical resistance, stress cracking, etc., may be important as well. Crosslinking is then an obvious alternative and it is used today on large commercial scale in wire and cable and pipe industries [1–4]. In cable jacketing, however, in many occasions especially for low-voltage application (<10 kV) the mechanical and thermal-endurance properties become more important than electrical properties. For example a furnace cable operated at 500 V requires good mechanical properties and stability of mechanical properties at elevated temperature which after ageing is the most important consideration; whereas for oil-resistant and fire retardant cables, the requirements are very different. There are three common methods of crosslinking polyethylene: 1) peroxide 2) irradiation and 3) silane [5–10]. Nowadays, silane crosslinking is becoming increasingly popular as replacement in certain applications for the other methods due to lower capital investment and increased productivity [11, 12].

In addition to polyethylene, today's vinyl acetate modified polyethylenes are also used in the wire and cable industry. The incorporation of small amount of vinyl acetate into polyethylene results in a resin which extrudes much like polyethylene, while providing the ability to accept filler loading e.g carbon black [13–15].

Actually a wide range of properties is possible depending on the vinyl acetate content. Density, crystallinity and toughness can be changed by vinyl acetate. Some researchers have studied the proper-

---

[*] Corresponding author, e-mail: h.azizi@ippi.ac.ir

ties of crosslinked ethylene-vinyl-silane copolymers [16–17]. Another important requirement for cables in some applications is flame resistance. Due to corrosiveness and toxicity of smoke and other emission products generated during the combustion of thermoplastics containing halogen-based fire retardants, extensive works have been carried out to use the alternative halogen free fire retardants. In particular some metallic hydroxide fillers have been studied. These metallic hydroxides are gaining increasing importance in the industry because of the desirable combination of low cost, low smoke and relatively high fire retardant efficiency. However one of the major drawbacks of adding these fillers is that the mechanical properties become much poorer than those of samples without added fillers. Several methods can be used to improve the interaction between polymer and filler [18–23]. Crosslinking can be a suitable method for this purpose [24, 25]. Using of some other new synthetic fire retardants has also been reported [26, 27]. In our previous papers, factors affecting silane grafting and water crosslinking and mechanical and thermal properties of XLPE were investigated [28, 29]. In the present study the effect of EVA and two metallic hydroxides on properties of silane-grafted water-crosslinked polyethylene are investigated. Flammability, mechanical and thermal behaviors of samples are evaluated.

2. Experimental

2.1. Materials

The polyethylene used was low density polyethylene (LDPE) with trade name of poliran-LF0200 (melt index = 1.6 g/10 min, $d = 0.923$ g/cm^3) from Arak Petrochemical Co. Iran. The silane was vinyl trimethoxy silane (VTMOS, $d = 0.97$ g/cm^3, boiling point = 123°C) as tarde name Dynasilan from Silvento, Germany, in the liquid from. Di-cumyl peroxide (DCP) with trade name of Dicup- from Hercules ($d = 1.02$ g/cm^3) was used as initiator. The non-halogenic fire retardants were alumina trihydrate (ATH, $d = 2.42$ g/cm^3) and Antimony trioxide (Sb_2O_3, $d = 5.2$ g/cm^3) in powder form from Merck. Ethylene vinyl acetate copolymer (EVA) prepared by Exxon. (USA. VA% = 18, $d = 0.94$ g/cm^3). Dibutyltin dilaurate (DBTDL) and Irganox 1010 were used as catalyst and antioxidant, respectively.

2.2. Sample preparation

Compounding was carried out using a single-screw extruder ($L/D = 31$). The screw was modular and designed to achieve best mixing efficiency using different mixing elements such as pineapple, pin-mixers and Maddock along the screw. Two-step Sioplas crosslinking method was selected to prepare XLPE compounds. In this method, catalyst and antioxidant were added to compound as a masterbatch. The amount of EVA was 5, 15 and 25 wt% and for ATH and Sb_2O_3 was 10, 20 and 30 phr. Before blending, the ATH and Sb_2O_3 were pre-mixed with LDPE and fed into the extruder from main hopper. The extrudate was cooled and granulated and resulting granules were compounded with silane and DCP in the extruder to silane-grafted samples. Finally the 95 percent of grafted sample was mixed with 5 percent of catalyst masterbatch and then granulated. The temperature profile was 130, 150, 170, 190, 200, 210, 220°C and screw rotation speed was 40 rpm. The amount of silane and DCP was fixed at 1.5 and 0.15 phr for all samples, respectively.

The granules were compression molded into the sheets. Crosslinking was carried out by exposing the sheets to hot water for 16 hours.

2.3. Characterization

Melting behavior was studied using a differential scanning calorimeter (DSC) model PL 1500 from polymer laboratory. Thermal gravimetric analysis of different samples was carried out by using a STA 625 from Rheometric Scientific in a nitrogen atmosphere at a heating rate of 20°C/min. A mass of about 100 mg of samples was heated at temperatures ranging from 30 to 800°C. Tensile properties were determined using an Instron 6025 according to ASTM D 638.

The gel content of silane crosslinked polyethylene was determined according to ASTM D 2765.The solvent used in the analysis of gel content was Xylene. Flammability behavior was characterized using the limiting oxygen index (LOI) according to ASTM D 2863. The limiting oxygen index was defined as the minimum mole percentage of oxygen in a mixture of oxygen and nitrogen necessary to barely support flaming combustion of a material initially at room temperature under the conditions of test method.

3. Results and discussion

3.1. Effect of ATH and Sb_2O_3 on properties of XLPE

3.1.1. Flammability behavior

Table 1 summarizes the LOI and composition of samples studied. As it can be seen from Table 1, LOI for crosslinked polyethylene is higher than that of original LDPE. This can be explained by increasing the thermal stability of LDPE with crosslinking. Table 1 shows that the limiting oxygen index increases with the amount of alumina trihydrate and antimony trioxide. Generally metallic hydroxides are believed to inhibit the flammability of polymers mainly by diluting the fuel with water vapor, increasing the heat of the material and insulating the substrate from heat source and thus reducing the rate of thermal degradation. It is obvious from Table 1 that the effectiveness of metallic hydroxides is more pronounced at higher loading (>30 phr). Comparison between samples 6 and 10 indicates that crosslinking of filled LDPE increases the LOI.

An important result seen from Table 1 is when using both ATH and Sb_2O_3, for which LOI increases significantly. In other words, there is a synergistic effect by using both ATH and Sb_2O_3. In addition, it is interesting to note that at similar loading – especially at higher loadings – alumina trihydrate inhibits combustion more effectively than antimony trioxide. Some researchers have studied the mechanism of action of ATH and Sb_2O_3. It is believed that Sb_2O_3 is effective in combination with halogen-based fire retardants. Some researchers investigated the interaction and synergism of metallic hydroxides with zinc borate and zinc hydroxystannate [30, 31].

Table 1. LOI of different samples

Sample No.	Sb_20_3 [phr]	ATH [phr]	VTMO [phr]	LOI [%]
1	0	0	0.0	17
2	0	0	1.5	20.4
3	0	30	0.0	22
4	0	10	1.5	19.7
4	0	20	1.5	21
5	0	30	1.5	24
6	30	0	0.0	18
7	10	0	1.5	19
8	20	0	1.5	20
9	30	0	1.5	22
10	15	15	1.5	26

3.1.2. Mechanical properties

Table 2 shows the tensile strength and elongation at break of neat LDPE (sample A), XLPE (sample D), LDPE-ATH (sample B), XLPE-ATH (sample E), LDPE-Sb_2O_3 (sample C) and XLPE-Sb_2O_3 (sample F). It is clearly obvious that by addition of ATH and Sb_2O_3 tensile strength and elongation at break decrease significantly. This is possibly due to insufficient interactions between the polymer and the filler, which result in their inferior properties. In contrast, with crosslinking of LDPE tensile strength improves (samples E, F, G, B, C).

The effect of ATH on tensile strength and elongation at break of XLPE is shown in Figure 1.

Table 2. The effect of ATH and Sb_2O_3 on tensile properties of XLPE

Sample No.	Elongation at break [%]	Tensile Strength [N/mm²]	Sb_2O_3 [phr]	ATH [phr]
A	576	12.2	0	0
B	23	8.4	0	30
C	48	10.5	30	0
D	395	14.5	0	0
E	22	11.7	0	30
F	30	12.7	30	0
G	23	11.7	15	15

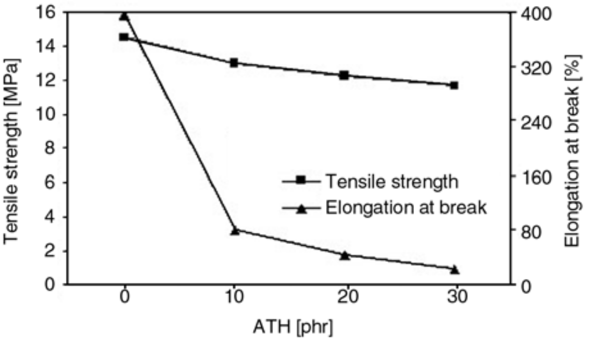

Figure 1. Variation of tensile strength and elongation at break of XLPE with ATH content

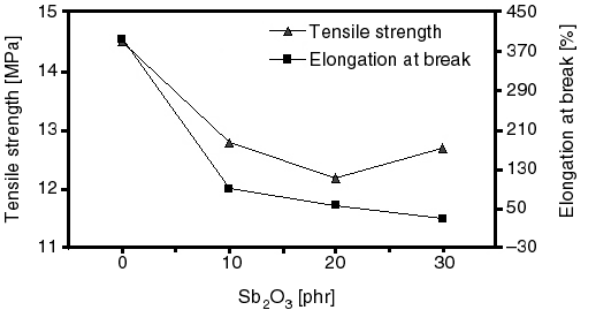

Figure 2. Variation of tensile strength and elongation at break of XLPE with Sb_2O_3 content

Generally, mechanical properties decrease with increasing filler content. Same results were found for XLPE-Sb_2O_3 samples (Figure 2).

3.1.3. Thermal decomposition behavior of XLPE-metallic hydroxide compositions

Polymers, being organic substances, have limited thermal stability. In the event of fire, due to a short circuit or other faults, the temperature of cable system may become very high. The thermal stability of the polymeric material is thus an important consideration in the selection of a cable.

The effect of crosslinking and addition of ATH and Sb_2O_3 (at 30 phr) on thermal decomposition behavior of LDPE is shown in Figures 3 and 4.

As it can be seen the onset decomposition temperature of LDPE-Sb_2O_3 (sample 7) is higher than that of LDPE-ATH (sample 6). However samples containing ATH show two-step decomposition. First at approx. 300°C ATH starts to decompose to yield water. But the temperature for maximum decomposition of ATH is the same as for Sb_2O_3.

With crosslinking thermal decomposition temperature of LDPE- filler samples did not change significantly.

The effect of alumina trihydrate and antimony trioxide on gel content is illustrated in Figure 5. Gel content decreases with increasing filler concentration, but the reduction is not considerable. This can be explained by inhibition effect of ATH and Sb_2O_3 for water permeation into LDPE structure. On the other hand surface of fillers may adsorb the silane component.

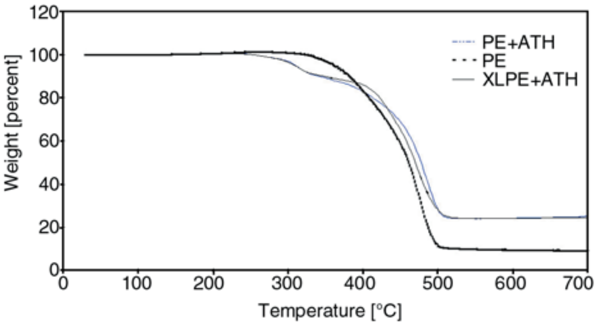

Figure 3. The effect of ATH and crosslinking on TGA thermogram of LDPE

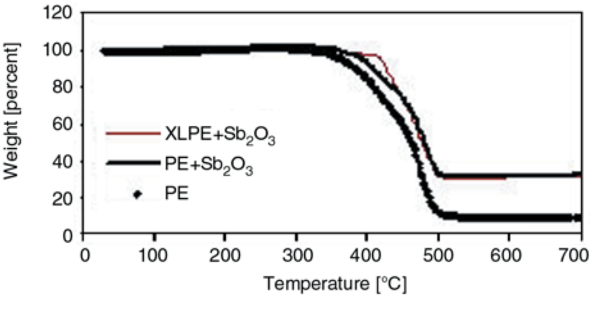

Figure 4. The effect of Sb_2O_3 and crosslinking on TGA thermogram of LDPE

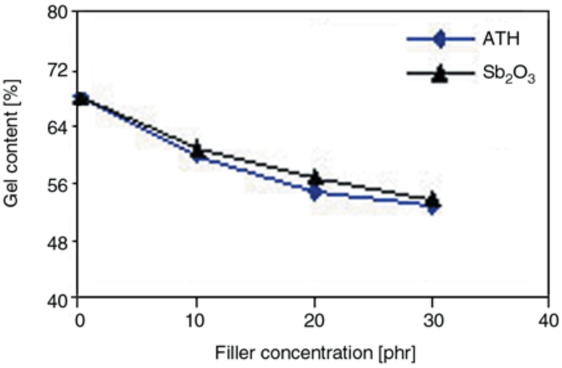

Figure 5. The changes of gel content with ATH and Sb_2O_3 concentration

3.2. Effect of EVA on properties of XLPE

3.2.1. Effect of EVA on gel content

Figure 6 shows the variation of gel content with EVA content. Gel content increases with increasing EVA concentration. By increasing EVA, crystallinity decreases and the amount of side chains increases therefore the permeation of water molecules into polymer structure increases and hence gel content increases. The polar groups of vinyl acetate can also facilitate the permeation of silane component into molecular structure of LDPE. On the other hand the peroxide-generated radicals can easily extract a hydrogen atom from EVA chains. It should be noted that compared to EVA, LDPE is relatively more difficult to crosslink. LDPE is a non-polar molecule with all its hydrogen atoms tightly bound to carbon atoms. The lack of highly reactive hydrogens means fewer sites for radical attack and lower reaction rates. EVA copolymers

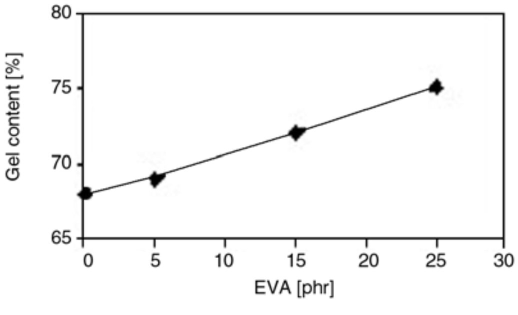

Figure 6. The effect of EVA concentration on gel content

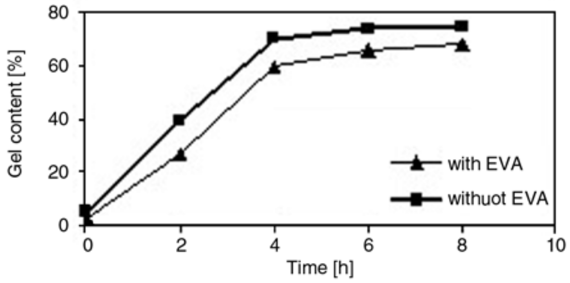

Figure 7. The influence of crosslinking time on gel content with and without EVA

are more readily crosslinked and accept high filler loading. In Figure 7 the influence of crosslinking time on gel content for LDPE/EVA blend is illustrated. The rate of crosslinking increases in presence of EVA.

3.2.2. Effect of EVA on thermal properties

Figure 8 shows the DSC thermogram of neat LDPE, neat EVA, LDPE/EVA and XLPE/EVA blend. As can be seen LDPE shows a sharp endothermic peak at 114.47°C. The effect of EVA and crosslinking on melting behavior of LDPE is shown. Blending of two semicrystalline polymers like LDPE and EVA with much lower crystallinity exhibits two distinct endothermic peaks corresponding to the melting of two different crystallites present in the blend. EVA shows two different peaks in DSC thermogram. In LDPE/EVA blend the melting point of LDPE shifted to lower values compared with that of neat LDPE. In XLPE/EVA blend two distinct endothermic peaks are presented. These peaks correspond to sol and gel fractions of the sample. In general, blending leads to broadening of melting peak.

The existence of two melting peaks for each blend which coincides exactly with peaks corresponding to two pure components eliminates the probability of the intermiscibility of the crystalline phases of two polymers. The polymers may be intimately mixed in the molten state; but as the blends are cooled from the melt, the crystallization of different components occurs separately, leading to two distinctly different crystalline states.

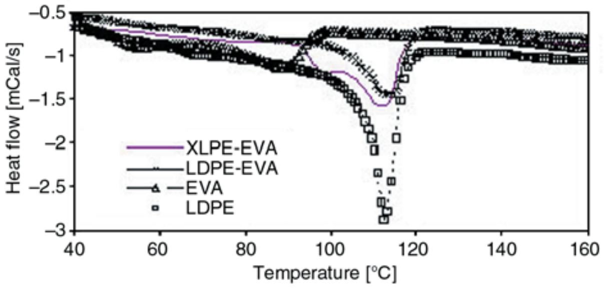

Figure 8. The effect of EVA and crosslinking on DSC thermogram of LDPE

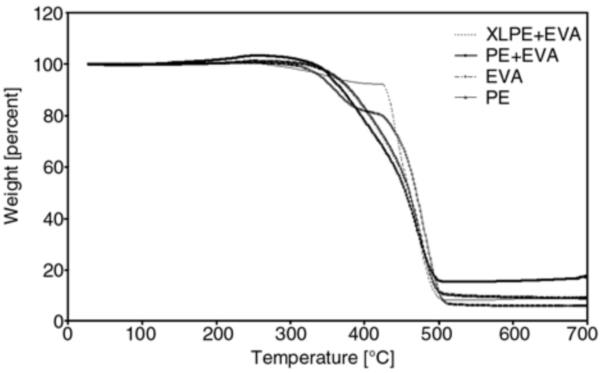

Figure 9. The effect of EVA and crosslinking on TGA thermogram of LDPE

Figure 9 shows the TGA curves of different samples. TGA analysis gives an idea of the thermal decomposition characteristics of different blends at elevated temperature. Two-stage decomposition is characteristics of EVA, whereas LDPE undergoes single-stage decomposition. The temperature at which EVA starts decomposing is about 350°C and the onset temperature of second-stage of decomposition of EVA is about 455°C.

In XLPE/EVA blend decomposition starts at 430°C. It means that decomposition temperature of XLPE/EVA blend is higher than that of LDPE/EVA blend.

3.2.3. Effect of EVA on mechanical properties of XLPE

The variation of tensile strength and elongation at break of XLPE versus EVA content is shown in Figure 10.

Tensile strength increases with increasing EVA concentration up to 15% beyond which it decreases slightly. It is found that for semicrystalline poly-

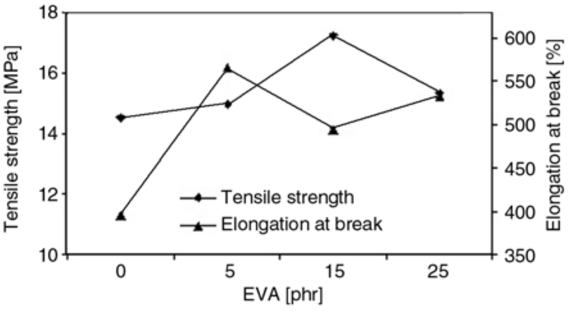

Figure 10. Variation of tensile strength and elongation at break of XLPE with EVA content

mers such as LDPE and EVA, the tensile strength depends not only on the degree of crystallinity but also on the extent of strain induced crystallization (strain-hardening) in the amorphous phase. This phenomenon is more prominent for EVA, which contains a higher ratio of amorphous zones compared to LDPE. Another factor in this study is crosslinking.

The introduction of crosslinking is in favor of the process of strain-induced crystallization by preventing chain slippage. On the other hand crystallinity decreases with crosslinking. As a result the competition between these factors indicates the trend of change of tensile properties. Generally elongation at break of samples containing EVA is higher than that of neat LDPE.

4. Conclusions

A study of the effect of ATH and Sb_2O_3 as non-halogenic flame retardants and EVA on continuous silane-crosslinking of LDPE has revealed the following:

- Flame retardancy is influenced by incorporating of metallic-hydroxide as flame retardant. LOI increases with increasing ATH and Sb_2O_3 content.
- Tensile strength and elongation at break of LDPE decrease by incorporating ATH and Sb_2O_3. With crosslinking the mechanical properties of filled-LDPE improve.
- The results of thermal gravimetric analysis showed that filled-XLPE is more thermally stable than virgin LDPE.
- Gel content decreases with increasing of ATH and Sb_2O_3 concentration while increases with increasing EVA content.
- Melting behavior of LDPE changes with adding EVA and crosslinking. In XLPE/EVA blend two distinct endothermic peaks corresponding to sol and gel fractions of sample are presented.
- Tensile strength and elongation at break of LDPE increase with increasing EVA up to 15 wt% beyond which tensile strength decreases slightly.

References

[1] Rado R., Zelenak P.: Crosslinking of polyethylene. International Polymer Science Technology, **19**, 33–47 (1992).

[2] Dufton P. W.: Recent developments in polymers for wire and cable: an industrial report. Rapra Technology, Shawbury (1995).

[3] Bostrom J-O., Gustafsson B., Lindbom L., Borealis A. B.: XLPE compound for fast cable line speed. IEEE Electrical Insulation Magazine, **13,** 33–36 (1997).

[4] Cameron R., Lien K. Lorigan P.: Advances in silane cross-linkable polyethylene. Wire Journal International, (**12**), 56–58 (1990).

[5] Sirisinha K., Kawko K.: Crosslinkable polypropylene composites made by the introduction of silane moieties. Journal of Applied Polymer Science, **97**, 1476–1483 (2005).

[6] Roberts B. E., Verne S.: Industrial applications of different methods of crosslinking polyethylene. Plastics Rubber and Composites Processing and Applications, **4**, 135–139 (1984).

[7] Vogt H.: Silane crosslined PE-LD for low-voltage cable. Kunststoffe German Plastics, **82**, 830–833 (1992).

[8] Rado R.: Preparation of crosslinkable polyethylene compounds. International Polymer Science Technology, **20**, 78–83 (1993).

[9] Thorburn B.: Crosslinking techniques for electrical jacketing materials. in 'Proceedings of the 52nd Annual Technical Conference, San Francisco, USA', 1379–1385 (1994).

[10] Shieh Y. T., Tsai T. H.: Silane grafting reactions for LDPE. Journal of Applied Polymer Science, **69**, 255–261 (1998).

[11] Kuan H-C., Kuan J-F., Ma C-C., Hung J-M.: Thermal and mechanical properties of silane-grafted water crosslinked polyethylene. Journal of Applied Polymer Science, **96**, 2383–2391 (2005).

[12] Huang H., Lu H. H., Liu N. C.: Influence of grafting formulations and extrusion conditions on properties of silane-grafted polypropylenes. Journal of Applied Polymer Science **78**, 1233–1238 (2000).

[13] Brogly M, Nardin M, Schultz J.: Effect of vinylacetate content on crystallinity and second-order transition in ethylene-vinylacetate copolymers. Journal of Applied Polymer Science, **64**, 1903–1912 (1997).

[14] Ray I, Khastgir D.: Low-density polyethylene (LDPE) and ethylene vinyl acetate (EVA) copolymer blends as cable insulants. Plastics Rubber and Composites Processing and Applications, **22**, 37–45 (1994).

[15] Ray I., Khastgir D.: Correlation between morphology with dynamic mechanical, thermal, physicomechanical properties and electrical conductivity for EVA-LDPE blends. Polymer, **34**, 2030–2037 (1993).

[16] Bolikhova V. D., Gvozdyukevich V. A., Glebko A. S, Drobinin A. N., Morozova L. S., Rumyansev V. D.: Production and properties of a silane-crosslinked ethylene-vinylacetate copolymer. International Polymer Science and Technology, **18**, 44–50 (1991).

[17] Palmlöf M, Hertberg T., Sultan B-A: Crosslinking reactions of ethylene vinyl silane copolymers at processing temperature. Journal of Applied Polymer Science, **42**, 1193–1203 (1991).

[18] Baillet C, Delfosse L.: The combustion of polyolefins filled with metallic hydroxides and antimony trioxide. Polymer Degradation and Stability, **30**, 89–99 (1990).

[19] Doi S., Isaka T.: Ethylene polymer compositions that are flame retardant. US Patent 4397981, USA (1983).

[20] Rychly J., Vesely K., Gál E., Kummer M., Jancar J., Rychlá L.: Use of thermal methods in the characterization of the high-temperature decomposition and ignition of polyolefins and EVA copolymers filled with $Mg(OH)_2$, $Al(OH)_3$ and $CaCO_3$. Polymer Degradation and Stability, **30**, 57–72 (1990).

[21] Vesely K., Rychly J., Kummer M., Jancar J.: Flammability of highly filled polyolefins. Polymer Degradation and Stability, **30**, 101–110 (1990).

[22] Hornsby P. R., Watson C. L.: A study of mechanism of flame retardance and smoke suppression in polymers filled with magnesium hydroxide. Polymer Degradation and Stability, **30**, 73–87 (1990).

[23] Hippi U., Mattila J., Korhonen M., Seppala J.: Compatibilization of polyethylene/aluminium hydroxide and polyethylene/magnesium hydroxide composites with functionalized polyethylenes. Polymer, **44**, 1193–1201 (2003).

[24] Yeh J. T., Yang H. M., Huang S. S.: Combustion of polyethylene filled with metallic hydroxide and crosslinkable polyethylene. Polymer Degradation and Stability, **50**, 229–234 (1995).

[25] Wang Z., Hu Y., Gui Z., Zong R.: Halogen-free flame retardation and silane crosslinking of polyethtylenes. Polymer Testing, **22**, 533–538 (2003).

[26] Haurie L., Fernandez A. I., Velasco J. I., Chimenos J. M., Cuesta J-M. L., Espiell F.: Synthetic hydromagnesite as flame retardant. Evaluation of the flame behaviour in a polyethylene matrix. Polymer Degradation and Stability, **91**, 989–994 (2006).

[27] Cai Y., Hu Y., Song L., Kong Q., Yang R., Zhang Y., Chen Z., Fan W.: Preparation and flammability of high density polyethylene/paraffin/organophilic montmorillonite hybrids as a form stable phase change material. Energy Conversion and Management, **48**, 462–469 (2007).

[28] Barzin J., Azizi H., Morshedian J.: Preparation of silane-grafted and moisture cross-linked low density polyethylene: Part I: Factors affecting performance of grafting and cross-linking. Polymer-Plastics Technology and Engineering, **45**, 979–983 (2006).

[29] Barzin J., Azizi H., Morshedian J.: Preparation of silane-grafted and moisture cross-linked low density polyethylene: Part II: Electrical, thermal and mechanical properties. Polymer-Plastics Technology and Engineering, **46**, 305–310 (2007).

[30] Antonietta G., Shanks R. A.: Structural and thermal interpretation of the synergy and interaction between the fire retardant magnesium hydroxide and zinc borate. Polymer Degradation and Stability, **92**, 2–13 (2007).

[31] Hornsby P. R., Cusack P. A, Cross M., Tóth A., Zelei B., Marosi G.: Zinc hydroxystannate coated metal hydroxide fire retardant. Journal of Materials Science, **38**, 2893–2899 (2003).

eXPRESS Polymer Letters Vol.1, No.6 (2007) 385–390
Available online at www.expresspolymlett.com
DOI: 10.3144/expresspolymlett.2007.54

Polyaniline nanofibers as a new gamma radiation stabilizer agent for PMMA

P. L. B. Araujo[1], *R. F. S. Santos*[2], *E. S. Araujo*[2*]

[1]Laboratório de Produtos Naturais Bioativos, DQ/UFRPE, Av. Dom Manoel de Medeiros, s/n, 52171-900 Recife, PE, Brazil
[2]Laboratório de Polímeros, DEN/UFPE, Av. Prof. Luis Freire, 1000, 50.740-540, Recife, PE, Brazil

Received 8 February 2007; accepted in revised form 15 May 2007

Abstract. Polyanilines are reported to exhibit stabilizing effects in rubber mixtures submitted to gamma-irradiation and thermo-oxidative treatment. Such abilities may be explained by their action as radical scavengers. Since radical formation followed by main chain scission is a widely accepted mechanism for radiolytic degradation of PMMA, polyaniline is a promising additive for commercial plastics submitted to radiosterilization processing. In this work, we investigated the ability of polyaniline emeraldine salt nanofibers (PANF-HCl) in preventing radiation damage on PMMA matrix. Effects of gamma-irradiation on PMMA/PANF-HCl composites films were assessed by comparison of the variation of viscosity-average molar mass (M_v) of PMMA at 25 kGy dose when compared to commercial PMMA films. Samples containing 0.15% PANF-HCl (wt/wt) retained 92% of the initial M_v after irradiation while control sample presented 42% of M_v retention. When exposed to 60–200 kGy doses, PANF-HCl embedded into PMMA matrix preserved their oxidation state but started to exhibit mild deprotonation. PANF-HCl nanofibers were characterized by Diffuse Reflection Infrared Fourier Transform Spectroscopy (DRIFTS) and Scanning Electronic Microscopy (SEM). PMMA/PANF-HCl composites films were characterized by SEM and UV-VIS spectroscopy.

Keywords: *nanomaterials, polyaniline, PMMA, gamma-irradiation, stabilization*

1. Introduction

Poly(methyl methacrylate) (PMMA) is a high transparent common polymer, presenting excellent mechanical and chemical properties [1]. PMMA is widely used for manufacturing of medical and dental supplies. Gamma irradiation is one of the most popular methods for sterilization of plastic medical devices, typically performed at 25 kGy sterilization dose [2]. When exposed to gamma-irradiation, PMMA undergoes radiolytic degradation by the formation of radicals followed by main chain scission and subsequent loss of mechanical properties [3]. While many additives have been used to protect polymers from thermo and photo-oxidative degradation [4–6], very little information on additives for radiolytic stabilization of PMMA has been published. In 1960, Charlesby observed that substances such as urea, di-m-toluylthiourea, aniline, 8-hidroxyquinoline and benzoquinone, in 10% (wt/wt), acted as protective agents against PMMA degradation caused by gamma irradiation [7]. Kolninov and Kolesnikova [8] showed that N,N,N’,N’-tetramethyl-4, 4’-diaminodiphenyl methane (Am) inhibited radiation induced degradation in PMMA matrix. Aquino and Araujo reported radio-protective action of a common photo-oxidative stabilizer, HALS (Hindered Amine Light Stabilizer), in PMMA films [9] and test specimens [10]. Both HALS [11] and Am [8] additives are believed to interrupt oxidative propagation reaction by scav-

---

[*]Corresponding author, e-mail: elmo@pesquisador.cnpq.br

enging of alkyl radicals. Substances presenting similar antioxidant activities are suitable candidates for radiostabilizing agents.

Polyanilines and other intrinsically conducting polymers (ICPs) present well-reported metal-like characteristics [12–16]. In addition, polyanilines exhibit antioxidant effect in rubber mixtures submitted to gamma-irradiation [17] and thermo-oxidative aging [17, 18]. Some reports show ICPs as biocompatible [19–22], biodegradable [22] and radical scavengers [23, 24] as well. Those important characteristics turn ICPs into attractive targets for studies of radiostabilizing effects on PMMA matrix.

In this work, we report a novel application of a conducting polymer, polyaniline, as radio-protecting for a conventional radio-sterilizable polymer, PMMA. Nanofibers of HCl doped polyaniline (PANF-HCl) were used at low amounts (0.15–0.30% (wt/wt)) into physical mixtures with commercial PMMA. Effects of gamma-irradiation on viscosity-average molar mass of commercial PMMA and PMMA/PANF-HCl composite showed that nanostructured PANI is an efficient protective agent against structural damage caused by gamma radiation.

2. Experimental

Aniline monomer, ammonium peroxydisulfate APS, butanone, calcium chloride ($CaCl_2$), hydrochloric acid (HCl), methylene chloride (CH_2Cl_2) and sodium dodecylsulfate (SDS) were of analytical grade. Aniline was vacuum distilled prior to use. Butanone was dried with $CaCl_2$ and distilled. Other chemicals and commercial PMMA (Acrigel, 100 kg/mol, RESARBRAS ACRILICOS, Brazil) were used as received.

HCl doped Polyaniline nanofibers (PANF-HCl) was synthesized through interfacial self-assembly polymerization according to Huang and Kaner [25], modified by the introduction of SDS as a surfactant agent [26]. Briefly, An (298 mg) and SDS (30 mg) were mixed with $CHCl_3$ (10 ml) and placed in a 50 ml beaker. 10 ml of a 1M HCl aqueous solution containing 182 mg of APS was gently added dropwise to the $CHCl_3$ solution, in order to prevent extensive mixing of the layers. The reaction was allowed to proceed overnight at room temperature. Precipitated material was filtered though a Hirsch funnel, washed with deionized distilled water and dried in a dissecator. Yields were around 1 mg of PANI-HCl per 10 mg of An reagent. PMMA/PANF-HCl mixtures were made as previously described [26]. In short, PANF-HCl dispersions in butanone (up to 250 mg/dl) were obtained after 5 to 10 min of sonication treatment of PANF-HCl powder mixed with this solvent, at room temperature (ultrasonic bath Quimis, 40 kHz). The obtained dispersions were combined to appropriate volume of a 6 g/dl PMMA/butanone solution and sonicated for 1 h at the same previously described conditions. 0.1 mm in thickness films containing 0.15 and 0.30% (wt/wt) PANF-HCl were obtained by casting from resulting mixture solution on glass plates. For comparison, PMMA in butanone solutions were sonicated for 1 h and PMMA film was also obtained by casting these solutions.

PMMA films and composite films were irradiated at 25 and 60 kGy dose in a gammacell irradiator (^{60}Co) at 3.84 kGy/h dose rate.

Scanning Electronic Microscopy (SEM, JEOL 6360) characterization of PANF-HCl, PMMA and PMMA/PANF-HCl was performed on gold-coated samples. Films thickness was measured by SEM on cross-section view of cryofractured samples. Diffuse Reflection Infrared Fourier Transform Spectroscopy (DRIFTS) characterization was obtained from crushed neat PANF-HCl powder placed on patches. Spectrum was performed in an ABB spectrophotometer using a FTLA 2000-100 accessory, with 300 scans, over a 4000–400 cm^{-1} region and a 4 cm^{-1} resolution. UV-Vis characterization of PMMA and PMMA/PANF-HCl films was done in a Perkin-Elmer spectrophotometer (Lambda-6). Viscosity-average molar mass (M_v) of PMMA and PMMA/PANF-HCl samples was determined with an Ostwald viscometer at 25°C using 0.3–3.8 g/dl butanone solutions through Mark-Houwink's equation: $[\eta] = K M_v^a$, where $[\eta]$ – intrinsic viscosity, $K = 6.8 \cdot 10^{-5}$ dl/g, $a = 0.72$ [27].

3. Results and discussion

Fine dark green powder of HCl Doped Polyaniline was obtained through an interfacial polymerization method in presence of SDS surfactant. SEM images of the final reaction product show fibrillar or rod-type nanostructures, with diameters ranging from 100 to 150 nm (Figures 1a and 1b). In the presence of SDS, PANF-HCl were thicker than those made in the absence of this surfactant [26]. Such charac-

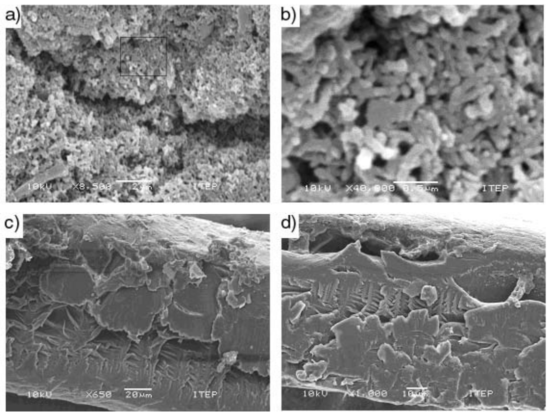

Figure 1. SEM images of: uncrushed PANF-HCl powder shows firmly packed aggregates of fibers or rods (a); higher magnification image of the region delimited by the square on Figure 1a (b); cross-sectional view of non-irradiated cryofractured PMMA/PANF-HCl film (0.3% (wt/wt)) (c) and neat PMMA film (d)

teristic may be desirable to ease the breaking up of the entanglements and to achieve a more homogeneous composite. Cross-section views of non-irradiated PMMA/PANF-HCl (0.3% (wt/wt)) (Figure 1c) and PMMA (Figure 1d) did not show any differences, probably due to the low PANF-HCl loads used in this work.

DRIFTS characterization of PANF-HCl exhibits bands at 1620 cm^{-1} attributed to C=N and C=C stretching of the quinoid diimine unit. C–C aromatic ring stretching of the benzenoid diamine unit appears at 1526 cm^{-1} and secondary aromatic amino group C–N stretching vibrations are shown at 1355 cm^{-1}. Each one of these bands is shifted approximately 60 cm^{-1} to higher wavenumber when compared to previous data obtained from HCl doped PANI by conventional FTIR method [28, 29]. However, the presence of ~1600 and ~1500 cm^{-1} bands implies the presence of amine and imine units in the molecular structure of PANF-HCl. Based on previous reports, the absorption intensity ratio of these two bands is an indicative of the oxidation state of the polymer [28, 30], as shown in the Equation (1):

$$R = \frac{I_{1620}}{I_{1526}} \tag{1}$$

From absorption intensity measured in DRIFTS data, R is equal to 1.05. This value identifies the emeraldine oxidation state of polyanilines [30]. Figure 2 shows the diffuse reflection IR spectra of PANF-HCl powder.

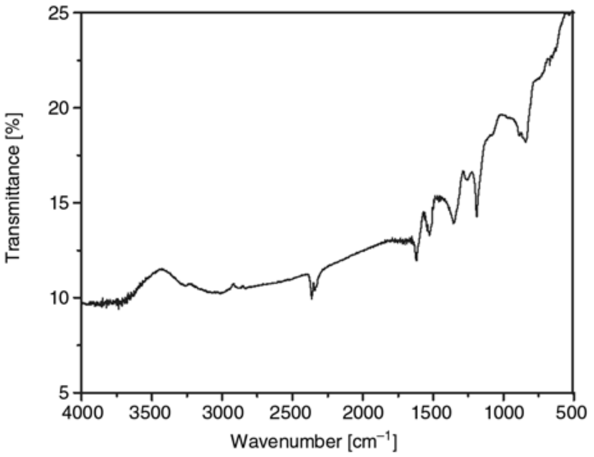

Figure 2. Diffuse reflection IR spectrum of neat PANF-HCl

Table 1. Variation of relative molar mass (M_v/M_{v0}) and protection index P[%] on irradiated polymeric system: PMMA + additive

<table>
<tr><th colspan="5">a) PANF-HCl composite films irradiated at 25 kGy dose[1]</th></tr>
<tr><th colspan="2">PANF-HCl
[% (wt/wt)]</th><th>$M_{v0}\cdot10^{-3}$
[g/mol]</th><th>M_v/M_{v0}
[%]</th><th>P
[%]</th></tr>
<tr><td colspan="2">0.15</td><td>90</td><td>92</td><td>93</td></tr>
<tr><td colspan="2">0.30</td><td>86</td><td>48</td><td>22</td></tr>
<tr><td colspan="2">Control</td><td>98</td><td>42</td><td>–</td></tr>
<tr><th colspan="5">b) HALS additivated PMMA films irradiated at 30 kGy dose[2]</th></tr>
<tr><th>HALS type</th><th>Additive
[% (wt/wt)]</th><th>$M_{v0}\cdot10^{-3}$
[g/mol]</th><th>M_v/M_{v0}
[%]</th><th>P
[%]</th></tr>
<tr><td rowspan="2">TINUVIN 622®[3]</td><td>0.30</td><td>137</td><td>96</td><td>70</td></tr>
<tr><td>0.60</td><td>144</td><td>96</td><td>68</td></tr>
<tr><td colspan="2">Control</td><td>155</td><td>87</td><td>–</td></tr>
</table>

[1]This work, [2]Reference [31], [3]Reference [9]

PMMA/PANF-HCl composite films prepared as previously mentioned were approximately 0.1 mm in thickness, stiff, slightly green, transparent and visually homogeneous. In order to assess possible radiostabilizing effects of PANF-HCl on PMMA matrix, films containing 0.15 and 0.30% PANF-HCl (wt/wt) were submitted to gamma irradiation at 25 kGy dose. Variation on viscosity-average molar mass before (M_{v0}) and after irradiation (M_v) showed that PANF-HCl containing samples underwent less degradation than control sample. Nevertheless, radio-protective actions decreased markedly when PANF-HCl concentrations increased from 0.15% to 0.30% (wt/wt) (Table 1). Radio-protective action of PANF-HCl can be seeing by comparison of α value (Equation 2), i. e. the number of main chain scissions per original molecule after irradiation:

$$\alpha = \frac{M_{v_0}}{M_v} - 1 \qquad (2)$$

were M_{v_0} is the molar mass of non-irradiated polymer and M_v is the molar mass after irradiation. From these values is possible to calculate the inhibition factor, P[%] (Equation 3), which indicates the reduction in yield of chain scissions in PMMA macromolecules containing PANF-HCl into polymer system:

$$P\,[\%] = \frac{\alpha_c - \alpha_a}{\alpha_c} \cdot 100 \qquad (3)$$

where α_c is the number of main chain scissions per original molecule in control samples and α_a in a given additivated sample, both irradiated at the same dose.

Composite containing 0.15% PANF-HCl (wt/wt) retained 92% of its initial molar mass after irradiation while control sample presented 42% of retention. PMMA/0.30% PANF-HCl composite films showed M_v/M_{v_0} ratio near to control value. In this case, PANF-HCl overload had an adverse effect on PMMA radioprotection. An excess amount of additive may act as an impurity that antagonizes the beneficial effect of the additive itself. The same phenomena could be observed when a type HALS additive, TINUVIN 622® [9], referred in the original work as D type, was used as radioprotective agent for PMMA in concentration higher than the optimum concentration of 0.30% [31] (Table 1b). P[%] values for PMMA/PANF-HCl (0.15% (wt/wt)) and PMMA/HALS (0.30% and 0.60% (wt/wt)) films show again higher protective action of PANF-HCl when compared to TINUVIN 622®, 93% and 70% and 68%, respectively (Table 1a and 1b). It is important to notice that PMMA control sample presented in the results of Table 1b was initially more resistant to radiation damage than the control sample used in this work (Table 1a).

PMMA/0.15% PANF-HCl composite films were irradiated at 60 to 200 kGy doses in order to verify possible alterations on PANF-HCl spectroscopic response on doses higher than the standard sterilization dose. UV-Vis absorption spectra of irradiated and non-irradiated composites are shown in Figure 3. PANF-HCl composite films showed three absorption bands at ~365, ~420 and 800–850 nm wavelength. These bands are typical of protonated form of polyaniline in the emeraldine oxidation state. The first absorption band is assigned to a π–π* transition of the benzenoid ring and the other two bands are associated with the polaron transitions [32]. The free carrier tail exhibited in the red/NIR region of these spectra is also observed when polyaniline doped with *d,l*-camphorsulfonic acid is exposed to secondary dopant [33]. UV-vis of dispersions of polyaniline nanoparticles prepared in the presence of SDS showed similar feature [34]. The occurrence of carrier tail is attributed to the expansion of the molecular coil of polyanilines induced by secondary dopants. This effect persists even in blends of polyaniline with common polymers [33]. Bands around 340 and 390 nm are probably from additives present on commercial PMMA. These bands markedly decrease in irradiated neat films (data not shown).

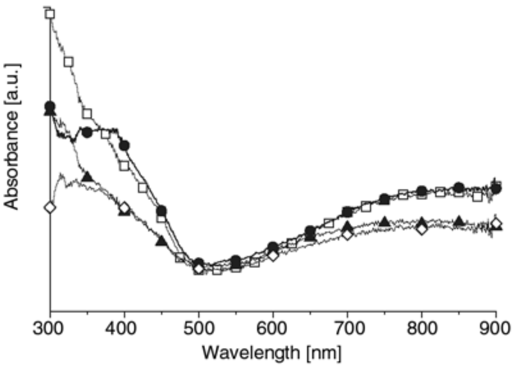

Figure 3. UV-Vis spectra. PMMA/PANF-HCl (0.15% (wt/wt)) composites films normalized by thickness and respective spectra of neat PMMA films. Non-irradiated (–•–) and irradiated at 60 kGy (–□–), 100 kGy (–▲–) and 200 kGy (–◊–)

After irradiation at 60 kGy, polaron bands at ~420 nm and 800–850 nm showed small decrease in intensity. This trend is confirmed by spectra of 100 and 200 kGy irradiated composite films. In addition there was a small increasing of absorption around 650–750 nm when compared to 800–850 nm bands. These data suggest that the irradiation initiated a process of deprotonation in PANF-HCl. Similar effects were reported to PMMA/polyaniline blends subjected to heat treatment in temperatures above 100°C [35].

4. Conclusions

It can be stated that polyaniline nanofibers doped with HCl (PANF-HCl), synthesized by the method described in this work, it is an effective protection agent against radiation damage on PMMA matrix, PMMA/0.15% PANF-HCl composite film exhibited a inhibition factor of 93% at the sterilization dose of 25 kGy. When exposed to 60–200 kGy doses, PANF-HCl embedded into the matrix preserved their oxidation state but started to exhibit mild deprotonation.

The radiostabilizing capacity of PANF-HCl has significant implications on the use of polymer composites as biomaterials. Considerable work remains to be done, in order to determinate and fully understand the mechanism of PANF-HCl protection on PMMA matrix.

References

[1] Chapiro A.: Radiation Chemistry of Polymeric Systems. John Wiley & Sons, New York (1962).

[2] Woo L., Ling M. T. K., Ding S. Y., Westphal S. P.: Effect of ionizing radiation on the thermal oxidative stability of medical polymers. Thermochimica Acta, **324**, 179–185 (1998).

[3] Guillet J.: Polymers photophysics and photochemistry. Cambridge University Press, New York (1987).

[4] Agnelli J. A. M.: Degradação de Estabilização de Polímeros. UFSCAR, São Paulo (1988).

[5] Gächter R., Müller H.: Plastics Additives Handbook. Hanser Publishers, Munich (1990).

[6] Smoliak L. Y., Prokopchuk N. R.: Estimation of parameters that correlate molecular structure of hindered amines with their stabilizing efficiency. Polymer Degradation and Stability, **82**, 169–172 (2003).

[7] Charlesby A.: Atomic Radiation and Polymers. Pergamon Press, New York (1960).

[8] Kolninov O. V., Kolesnikova V. V.: ESR study of stable *N,N,N',N'*-tetramethyl-4,4'-diaminediphenylmethane radicals in solid solutions. High Energy Chemistry, **35**, 328–334 (2001).

[9] Aquino K. A. S., Araujo E. S.: Uso de aditivos comerciais tipo *HALS* na estabilização radiolítica em filmes de PMMA nacional. Revista Brasileira de Pesquisa e Desenvolvimento, **6**, 45–52 (2004).

[10] Aquino K. A. S., Araujo E. S.: Caracterização estrutural do poli(metacrilato de metila) nacional estável à radiação gama: espectroscopia, propriedades óticas e viscosimetria. Revista Brasileira de Pesquisa e Desenvolvimento, **6**, 107–115 (2004).

[11] Mark H. F., Bikales N., Overberger C. G., Menges G.: Encyclopedia of Polymer Science and Engineering. John Wiley & Sons, New York (1989).

[12] MacDiarmid A. G., Chiang J. C., Richter A. F., Somasiri N. L. D., Epstein A. J.: Conducting Polymers. Reidel, Dordrecht (1986).

[13] Cotevieille D., le Méhautè A., Challioui C., Mirabeau P., Demay J. N.: Industrial applications of polyaniline. Synthetic Metals, **101**, 703–704 (1999).

[14] Pron A., Rannou P.: Processible conjugated polymers: from organic semiconductors to organic metals and superconductors. Progress in Polymer Science, **27**, 135–190 (2002).

[15] Bäcklund T. G., Sandberg H. G. O., Österbacka R., Stubb H., Mäkelä H., Jussila S.: Towards all-polymer field-effect transistor with solution processable materials. Synthetic Metals, **148**, 87–91 (2005).

[16] Reece D. A., Ralph S. F., Wallace G. G..: Metal transport studies on inherently conducting polymer membranes containing cyclodextrin dopants. Journal of Membrane Science, **249**, 9–20 (2005).

[17] Ismail M. N., Ibrahim M. S., Abd El-Ghaffar M. A.: Polyaniline as an antioxidant and antirad in SBR vulcanizates. Polymer Degradation and Stability, **62**, 337–341 (1998).

[18] Helaly F. M., Darwich W. M., El -Ghaffar A.: Effects of some polyaromatic amines on the properties of NR and SBR vulcanizates. Polymer Degradation and Stability, **64**, 251–257 (1999).

[19] Schmidt, C. E., Shastri V. R., Vacanti J. P., Langer R.: Stimulation of neurite outgrowth using an electrically conducting polymer. Proceedings of the National Academy of Sciences of the United States of America, **94**, 8948–8953 (1997).

[20] Garner B., Hodgson A. J., Wallace G. G., Underwood P. A.: Human endothelial cell attachment to and growth on polypirrole-heparin is vitronectin dependent. Journal of Materials Science: Materials in Medicine, **10**, 19–27 (1999).

[21] Kamalesh S., Tan P., Wang J., Lee T., Kang E. T., Wang C. H.: Biocompatibility of electroactive polymers in tissues. Journal of Biomedical Materials Research, **52**, 467–478 (2000).

[22] Rivers T. J., Hudson T. W., Schmidt C. E.: Synthesis of a novel, biodegradable electrically conducting polymer for biomedical applications. Advanced Functional Materials, **12**, 33–37 (2002).

[23] Gizdavic-Nikolaidis M., Travas-Sejdic J., Kilmartin P. A., Bowmaker G. A., Cooney R. P.: Evaluation of antioxidant activity of aniline and polyaniline. Current Applied Physics, **4**, 343–346 (2004).

[24] Gizdavic-Nikolaidis M., Travas-Sejdic J., Kilmartin P. A., Bowmaker G. A., Cooney R. P.: Conducting Polymers as free radical scavengers. Synthetic Metals, **140**, 225–232 (2004).

[25] Huang J., Kaner R. B.: A general chemical route to polyaniline nanofibers. Journal of the American Chemical Society, **126**, 851–855 (2004).

[26] Araujo P. L. B., Araujo E. S., Santos R. F. S., Pacheco A. P. L.: Synthesis and morphological characterization of PMMA/polyaniline nanofiber composites. Microelectronics Journal, **36**, 1055–1057 (2005).

[27] Brandrup J., Immergut E. H.: Polymer Handbook. John Wiley & Sons, New York, (1989).

[28] Abdiryim T., Xiao-Gang Z., Jamal R.: Comparative studies of solid state synthesized polyaniline doped with inorganic acids. Materials Chemistry and Physics, **90**, 367–372 (2005).

[29] Kulkarni M. V., Viswanath A. K., Marimuthu R., Seth T.: Spectroscopic, transport, and morphological studies of polyaniline doped with inorganic acids. Polymer Engineering and Science, **44**, 1676–1681 (2004).

[30] Huang L-M., Wen T-C., Gopalan A.: Synthesis and characterization of soluble conducting poly (aniline-co-2, 5-dimethoxyaniline). Materials Letters, **57**, 1765–1774 (2003).

[31] Aquino, K. A. S. Estabilizaçao Radiolítica do Poli(metacrilato de metila) utilizando aditivos comerciais. Master Dissertation, Federal University of Pernambuco, Brazil, 2000.

[32] Stejskal J., Kratochvíl P., Radhakrishnan N.: Polyaniline Dispersions 2. UV-Vis absorption spectra. Synthetic Metals, **61**, 225–231 (1993).

[33] MacDiarmid A. G., Epstein A. J.: The concept of secondary doping as applied to polyaniline. Synthetic Metals, **65**, 103–116 (1994).

[34] Kim B-J., Oh S-G., Han M-G., Im S-S.: Synthesis and characterization of polyaniline nanoparticles in SDS micellar solutions. Synthetic Metals, **122**, 297–304 (2001).

[35] Yang C. Y., Reghu M., Heeger A. J., Cao Y.: Thermal stability of polyanilines network in conduction polymer blends. Synthetic Metals, **79**, 27–32 (1996).

eXPRESS Polymer Letters Vol.1, No.6 (2007) 391–396
Available online at www.expresspolymlett.com
DOI: 10.3144/expresspolymlett.2007.55

Copolymers of N-cyclohexylacrylamide and n-butyl acrylate: synthesis, characterization, monomer reactivity ratios and mean sequence length

*P. Pazhanisamy**, *B. S. R. Reddy*

Industrial Chemistry Division, Central Leather Research Institute, Adayar, Chennai-600020, Tamil Nadu, India

Received 11 February 2007; accepted in revised form 14 May 2007

Abstract. Copolymerization of N-cyclohexylacrylamide (NCHA) and n-butyl acrylate (BA) was carried out in dimethylformamide at 55±1°C using azobisisobutyronitrile as a free radical initiator. The copolymers were characterized by ^{1}H-NMR spectroscopy and the copolymer compositions were determined by ^{1}H-NMR analysis. The reactivity ratios of the monomers were determined by both linear and non-linear methods. The reactivity ratios of monomers determined using linear methods like Fineman-Ross ($r_1 = 0.37$ and $r_2 = 1.77$), Kelen-Tudos ($r_1 = 0.38$ and $r_2 = 1.77$), ext. Kelen-Tudos ($r_1 = 0.37$ and $r_2 = 1.75$) Yezrieler-Brokhina-Roskin ($r_1 = 0.37$ and $r_2 = 1.77$) and non-linear methods like Tidwell-Mortimer ($r_1 = 0.37$ and $r_2 = 1.76$), ProCop ($r_1 = 0.36$ and $r_2 = 1.82$). The Q and e values for NCHA are 0.67 and 0.68 respectively. Mean sequence lengths of copolymers are estimated from r_1 and r_2 values. It shows that the BA units increases in a linear fashion in the polymer chain as the concentration of BA increases in the monomer feed.

Keywords: *polymer synthesis, molecular engineering, reactivity ratios, mean sequence length*

1. Introduction

Functional polymers are now being synthesized and used not only for their macromolecular properties but also for the properties of the functional groups [1]. Acrylic polymers have acquired prime importance in various avenues of application in leather, textile and building materials.

Moreover, the N-substituted acrylamides are used to prepare thermosensitive materials like poly(N-isopropylacrylamide) and copolymers of N-ethylacrylamide and styrene [2]. The thermosensitive polymers present also great potential in application as drug delivery system [3], human gene vectors [4] and biocatalysts [5].

The determination of copolymer composition and reactivity ratios of the monomers is important in evaluating the specific application of the copolymer [6]. The monomer reactivity ratios determined by conventional linearization methods are not always accurate and several non-linear methods have been attempted to determine their value [7–9]. ^{1}H-NMR spectroscopic analysis has been established as a powerful tool for the estimation of copolymer composition [10, 11].

The present article reports the synthesis and characterization of copolymers of N-cyclohexylacrylamide with n-butyl acrylate. The determination of monomer reactivity ratios of the monomers and mean sequence lengths of copolymers are also reported.

---

*Corresponding author, e-mail: p_pazhanisamy@yahoo.com

2. Experimental

2.1. Materials

The monomer N-cyclohexylacrylamide (NCHA) was prepared by the procedure described in the literature [12]. The comonomer n-butyl acrylate (BA) was freed from inhibitor by washing with 5% NaOH followed by distilled water, dried over CaH_2 and then distilled twice under reduced pressure. Azobisisobutyronitrile (AIBN) was recrystallized from chloroform. All the solvents were purified by distillation prior to their use.

2.2. Copolymerization

The copolymerization was carried out in glass reaction tubes (80 ml), provided with a gas inlet and outlet, at 55±1°C using AIBN as the free-radical initiator. The reaction tubes containing the required amount of monomers and initiator dissolved in DMF was deaerated by flushing with pure, dry nitrogen gas and then sealed. The conversions of the polymerization were controlled to be less than 10%. After the polymerization, the copolymers were precipitated by adding ice cold water. The precipitated polymers were filtered off and washed repeatedly with fresh methanol. The copolymers obtained were purified twice by dissolving in DMF and reprecipitating with methanol. The polymers were dried in vacuum at 60°C for 24 hours.

2.3. ^{1}H-NMR spectroscopy

The ^{1}H-NMR spectra of monomers and copolymers were recorded on the EM-390 NMR Spectrometer operating 90 MHz with $CDCl_3$ as solvent. The following peaks appear in NCHA spectrum; at 1.2–2.02 ppm for cyclohexyl CH_2 at 3.72 ppm for cyclohexyl methyne, at 5.38–6.28 ppm for vinyl protons and at 7.3 ppm for N–H proton. The following peaks appear in BA spectrum; at 0.9 ppm for CH_3, at 1.1–1.7 ppm for $(CH_2)_{b,c}$ at 4.1 ppm for OCH_2 and at 5.5–6.2 ppm for vinyl proton.

3. Results and discussion

Copolymers of NCHA and BA with different feed compositions were prepared by free-radical polymerization in DMF using AIBN initiator. Copolymerization was restricted to give less than 10% conversion. The monomer units in the copolymer are shown in Figure 1. The copolymer composition data of the monomers in the feed and copolymers is presented in Table 1.

3.1. Characterization

The ^{1}H-NMR spectrum of copolymer, poly(NCHA-co-BA) (0.5:0.5) is shown in Figure 2. The peak assignments for the copolymers were based on the spectra of monomers NCHA and BA. The following peaks appear in the copolymer spectrum: at 0.8 ppm for CH_3, at 1.1–2.1 ppm for cyclohexylmethylenes and $(CH_2)_{b,c}$ of BA, at 2.1–2.3 ppm for backbone CH_2, at 2.5 ppm due to backbone

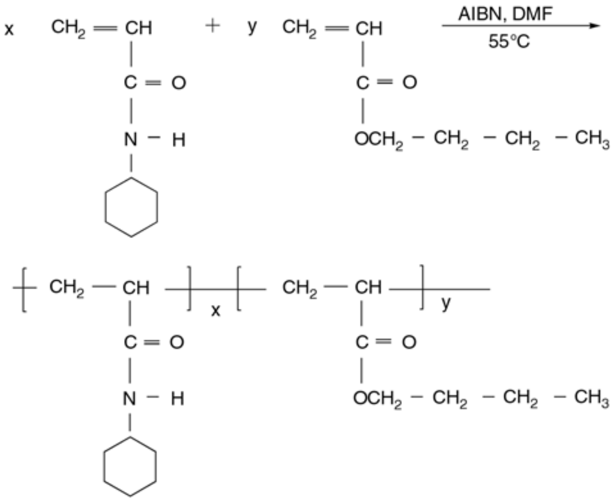

Figure 1. Synthesis of poly (NCHA-co-BA)

Table 1. Copolymerization of NCHA and BA in DMF at 55±1°C

Copolymers	Mole fraction of NCHA, M_1	Mole fraction of BA, M_2	% of conversion	Mole fraction of BA in copolymer m_2	$F = M_1/M_2$	$f = m_1/m_2$	H	G	η	E
1	0.2	0.8	7.08	0.88	0.250	0.136	0.460	–1.588	–0.6257	0.1813
2	0.3	0.7	8.10	0.82	0.429	0.220	0.836	–1.521	–0.5220	0.2869
3	0.4	0.6	8.40	0.74	0.667	0.351	1.267	–1.233	–0.3686	0.3788
4	0.5	0.5	7.60	0.67	1.000	0.493	2.028	–1.029	–0.2506	0.4939
5	0.6	0.4	8.04	0.58	1.500	0.724	3.108	–0.572	–0.1103	0.5993
6	0.7	0.3	8.52	0.48	2.333	1.083	5.026	0.179	0.0252	0.7075
7	0.8	0.2	7.84	0.37	4.000	1.703	9.395	1.651	0.1439	0.8187

$\alpha = (H_{min} \cdot H_{max})^{1/2} = 2.078$

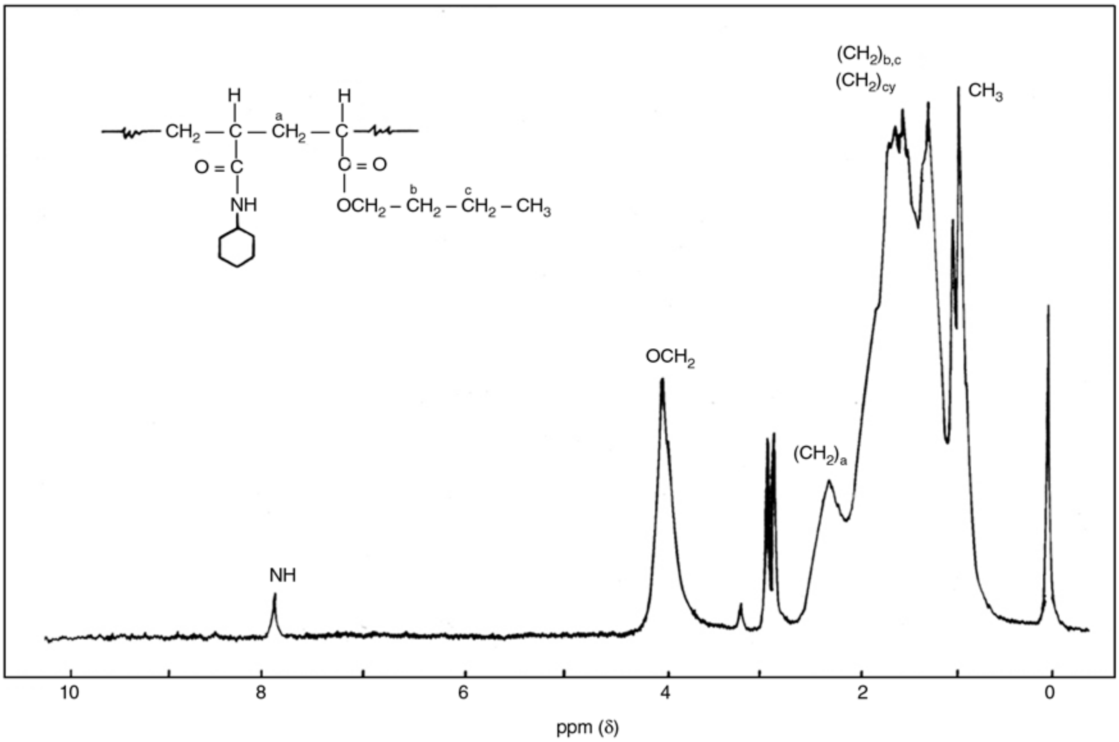

Figure 2. ^{1}H-NMR spectrum of copolymer, poly(NCHA-co-BA) (0.5:0.5)

methyne C–H, at 3.3 ppm for cyclohexyl methyne proton, at 3.9–4.2 ppm for OCH$_2$ and at 7.9 ppm for N–H.

3.2. Copolymer compositions

The copolymer composition was determined from ^{1}H-NMR spectral analysis of the copolymer. The assignment of the resonance peaks in the ^{1}H-NMR spectrum allows the accurate evaluation of the content of each kind of monomer incorporated into the copolymer chain.

The oxymethylene (OCH$_2$) peak area is used to determine the copolymer composition. The integrated intensity of this peak is compared to the total intensities of all the peaks in the copolymer spectrum, which is a measure of their relative areas [6]. The copolymer compositions can be obtained using Equation (1):

$$X_{\mathrm{BA}} = \frac{15A(\mathrm{OCH_2})}{2A_{total} + 3A(\mathrm{OCH_2})} \qquad (1)$$

where X – mole fraction and A – peak area. Table 1. gives the values of the corresponding mole fractions in the copolymers. The kinetic behavior was determined by plotting the mole fraction of BA in the feed against that in the copolymer (Figure 3).

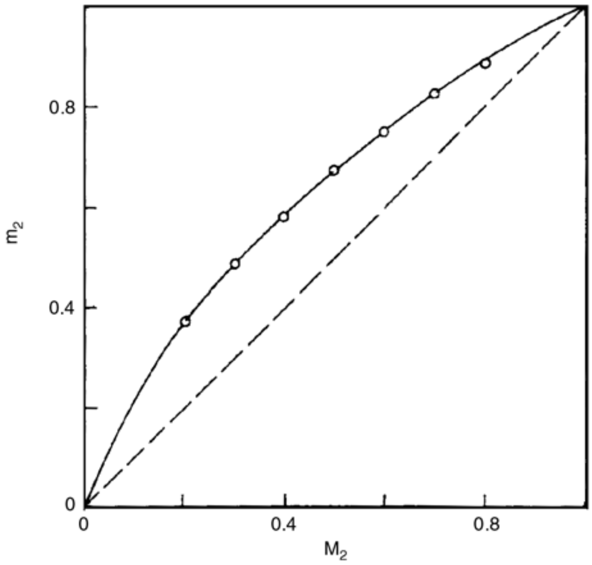

Figure 3. Copolymer composition diagram of poly(NCHA-co-BA) system

3.3. Reactivity ratios

From the monomer feed ratios and the resultant copolymer compositions, the reactivity ratios of monomer 1 (NCHA) and monomer 2 (BA) were evaluated by the methods of Fineman-Ross [13] (FR), Kelen-Tudos [14] (KT) and extended Kelen-Tudos [15] (EKT).

Table 2. Extended KT parameters for NCHA and BA copolymer system

Parameters	**Copolymer system**						
	1	**2**	**3**	**4**	**5**	**6**	**7**
ξ_2	0.0791	0.1018	0.1064	0.1050	0.1204	0.1411	0.1493
ξ_1	0.0430	0.0522	0.0560	0.0517	0.0581	0.0656	0.0636
Z	0.5334	0.4994	0.5123	0.4785	0.4666	0.4460	0.4064
F	0.2550	0.4405	0.6852	1.0303	1.5517	2.4282	4.1905
H	0.4780	0.8821	1.3371	2.1528	3.3257	5.4450	10.3087
G	–1.6198	–1.5619	–1.2668	–1.0601	-0.5915	0.1861	1.7298
H	–1.0715	–0.8153	–0.5343	–0.3327	–0.1355	0.0287	0.1525
E	0.3162	0.4604	0.5640	0.6756	0.7616	0.8405	0.9089

$\alpha = (F_{min} \cdot F_{max})^{1/2} = 1.0337$ $r_1 = 0.38$ and $r_2 = 1.77$ – KT
$r_1 = 0.37$ and $r_2 = 1.75$ – EKT

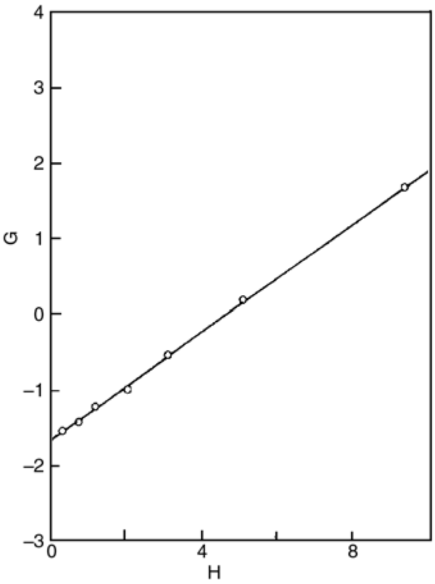

Figure 4. F-R Plot for (NCHA-co-BA) system

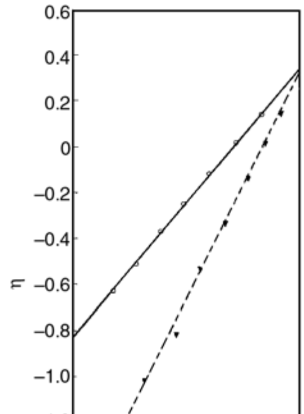

Figure 5. K-T (O) and EK-T (⅄) plot for poly(NCHA-co-BA) system

Table 3. Copolymerization parameter, for the NCHA and BA copolymer system

Methods	r_1^a	r_2^a	$r_1 \cdot r_2$
Fineman-Ross (F-R)	0.37	1.77	0.65
Kelen-Tudos (K-T)	0.38	1.77	0.67
Ext. Kelen-Tudos (EK-T)	0.37	1.75	0.65
Yezrielev-Brokhina-Roskin (YBR)	0.37	1.77	0.65
Tidwell-Mortimer (TM)	0.37	1.76	0.65
Procop Opt Pex2	0.36	1.82	0.65

$^a r_1$ and r_2 are the reactivity ratios for NCHA and BA respectively

The significant parameters of FR, KT and EKT equation are presented in Table 2. The reactivity ratios for NCHA (r_1) and BA (r_2) from the FR plot (Figure 4), KT and EKT plot (Figure 5) are given in Table 3.

The monomer reactivity ratios determined by conventional linearization methods are not always accurate and several non-linear methods have been attempted to determine their values [8]. The reactivity ratios were also determined by non-linear method (TM and Opt-Pex2) by using the ProCop computer program [16].

Tidwell-Mortimer (TM) method is the best non-linear method when the differential Mayo-Lewis equation is applied. The reactivity ratios estimated by TM are $r_1 = 0.37$ and $r_2 = 1.76$. The 95% joint confidence region for the determined r_1 and r_2 values using ProCop computer program is shown in Figure 6. The other differential methods used to estimate reactivity ratios provide very similar results and all reactivity ratios are located inside confidence domain.

The value(s) of r_1 is less than 1 and r_2 is greater than 1. r_1 shows that NCHA favors cross-propagation as opposed to homopropagation and r_2 shows that BA favors homopropagation over cross-propa-

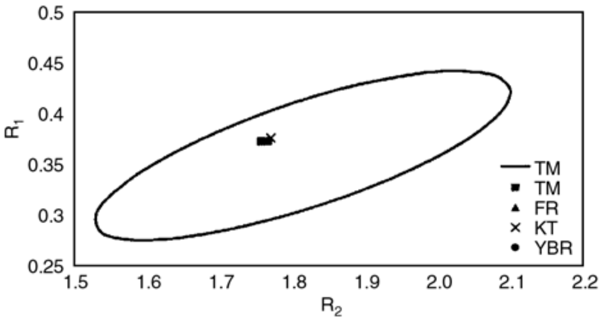

Figure 6. 95% joint confidence region of r_1 and r_2 values by Procop computer program

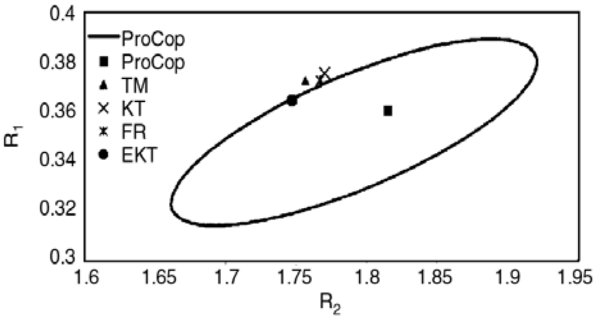

Figure 7. r_1 and r_2 values by (–) Procop, (□) Procop, (Δ) TM, (×) KT, (∗) FR, (•)EKT

gation. r_1 and r_2 together show that BA is generally more reactive than NCHA, hence the copolymers contain a higher proportion of BA units. The product of r_1 and r_2 is less than the unity (0.65), which indicates random distribution. The more these values diverge from unity, less random the distribution will be. A plot of copolymer composition against the composition of the feed is shown by a solid line in Figure 3. The dashed line represents the ideal random copolymerization.

3.4. Effect of conversion value

The ProCop computer program uses a non-linear calculation method (OPT-Pex2) which is able to minimize F(2) value taking into account the conversion values as well (Equation (2)):

$$F = \sqrt{\frac{\sum_{i=1}^{n}\left(m_i^{\exp} - m_i^{cal}\right)^2}{n-2}} \tag{2}$$

where $m_i^{\exp}$ is the copolymer composition experimentally determined for the i point, m_i^{cal} is the copolymer composition calculated at the conversion mentioned in Table 1 for the i experiment and n is the overall number of experiments.

The conversion effect may be a function of the feed composition and of the comonomer pair to undergo polymerization. If r_i and $r_j < 1.0$ the effect of conversion is relatively unimportant. Conversion values are more important to estimate the reactivity ratios when $r_i > 1.0$ and $r_j < 1.0$ [17]. In our copolymerization system the $r_1 < 1.0$ and $r_2 > 1.0$. Hence, the conversion values (7.1%–8.5%) play an important role in the estimation of reactivity ratios.

The reactivity ratios of NCHA and BA estimated via the ProCop method are $r_1 = 0.36$ and $r_2 = 1.82$ respectively. The reactivity ratio determined by various differential methods are shown in Figure 7 along with the result determined via a non-linear, method (ProCop) involving conversion. Regardless of the low conversion values, the reactivity ratios estimated by differential methods (linear or non-linear) are located outside of the confidence region because of the conversion effect. EKT, which also takes into account conversion values within a linear method, provides better reactivity ratios, located at the limit of the confidence domain. When conversion is taken into consideration the superiority of the non-linear integral method becomes obvious.

3.5. Mean sequence length

The mean sequence length [10] can be determined using the pertinent equations ((3) and (4)):

$$\overline{l_1} = r_1\frac{M_1}{M_2} + 1 \tag{3}$$

$$\overline{l_2} = r_2\frac{M_2}{M_1} + 1 \tag{4}$$

where r_1 and r_2 are the reactivity ratios and M_1 and M_2 represent the concentration of NCHA and BA respectively, in the monomer feed. The mean

Table 4. Mean sequence lengths in NCHA and BA copolymerization[a]

BA in feed, M_2 [Mole%]	l_1	l_2	l_1:l_2	Distribution[b]
0.80	1.09	8.26	1:8	N BBBBBBBBN
0.70	1.15	5.26	1:5	NBBBBBN
0.60	1.24	3.72	1:3	NBBBN
0.50	1.36	2.82	1:2	NBBN
0.40	1.54	2.21	2:2	
0.30	1.84	1.78	1:1	
0.20	2.44	1.45	2:1	

[a] $r_1 = 0.36$, $r_2 = 1.82$

[b] Only a few cases are illustrated (N = NCHA; B = BA)

sequence lengths of copolymers are given Table 4. It is significant to note from Table 4 that the BA units increases in a linear fashion in the polymer chain as the concentration of BA increases in the monomer feed.

4. Conclusions

Copolymers of NCHA and BA having different composition were synthesized in DMF by free radical polymerization. The structure of the copolymers was confirmed by ^{1}H-NMR Spectroscopy. The copolymer compositions were determined from ^{1}H-NMR analysis data. The reactivity ratios of monomers were determined by linear methods like Fineman-Ross ($r_1 = 0.37$ and $r_2 = 1.77$), Kelen-Tudos ($r_1 = 0.38$ and $r_2 = 1.77$), Ext. Kelen Tudos ($r_1 = 0.37$ and $r_2 = 1.75$) Yezrieler-Brokhina-Roskin ($r_1 = 0.37$ and $r_2 = 1.77$) and non-linear methods like Tidwell-Mortimer ($r_1 = 0.37$ and $r_2 = 1.76$), Procop ($r_1 = 0.36$ and $r_2 = 1.82$). The values are in good agreement. $r_2 > 1$ indicates BA is more reactive than NCHA thereby favouring the formation of longer blocks of BA as its concentration in the feed increases. The values of r_1 and r_2 diverge from unity, $r_1, r_2 < 1$ (0.65) shows random distribution. r_2 shows that BA favours homopropagation over cross-propagation. The mean sequence length determination shows that BA units increases in a linear fashion in the polymer chain as the concentration increases in the monomer feed.

References

[1] Akelah A., Moet A.: Functionalized polymers and their applications. Chapman and Hall, London, 1990.

[2] Nichifor M., Zhu X. X.: Copolymers of N-alkylacrylamide and styrene as new thermosensitive materials. Polymer, **44**, 3053–3060 (2003).

[3] Leroux J., Roux E., Le Garrec D., Hong K., Drummond D. C.: N-isopropylacrylamide copolymers for the preparation of pH-sensitive liposomes and polymeric micelles. Journal of Controlled Release, **72**, 71–84 (2001).

[4] Kurisawa M., Yokayama M., Okano T.: Gene expression control by temperature with thermo-responsive polymeric gene carriers. Journal of Controlled Release, **69**, 127–137 (2000).

[5] Kokufuta E.: Novel application for stimulus-sensitive polymer gels in the preparation of functional immobilized biocatalysts. Advances in Polymer Science, **110**, 157–177 (1993).

[6] Pitchumani S., Rami Reddy C., Rajadurai S.: Reactivity ratios of ethyl acrylate, n-butyl methacrylate copolymer system by ^{1}H-NMR analysis. Journal of Polymer Science: Polymer Chemistry Edition, **20**, 277–282 (1982).

[7] Dube M., Sanayei R. A., Penlidis A., O' Driscoll K. F., Reilly P. M.: A microcomputer program for estimation of copolymerization reactivity ratios. Journal of Polymer Science, **29**, 703–708 (1991).

[8] Polic A. L., Duever T. A., Penlidis A.: Case studies and literature review on the estimation of copolymerization reactivity ratios. Journal of Polymer Science Part A: Polymer Chemistry, **36**, 813–822 (1998).

[9] Hagiopol C., Frangu O., Dumitru L.: A nonlinear method for estimation of reactivity ratios in copolymerization processes. Journal of Macromolecular Science Chemistry Edition, **26**, 1363–1379 (1989).

[10] Pazhanisamy P., Ariff M., Anwaruddin Q.: Copolymers of α-methylstyrene with N-cyclohexylacrylamide: Synthesis, monomer reactivity ratios and mean sequence length. Journal of Macromolecular Science: Pure and Applied Chemistry, **34**, 1045–1054 (1997).

[11] Pazhanisamy P., Sulochana P., Anwaruddin Q., Ariff M.: Reactivity ratios of N-cyclohexylacrylamide-styrene copolymers by ^{1}H and ^{13}C-NMR spectroscopy. Journal of Polymer Science Part A: Polymer Chemistry, **35**, 193–195 (1997).

[12] Plaut H., Ritter J. J.: A new reactions of nitriles IV. Unsaturated amides. Journal of American Chemical Society, **73**, 4076–4077 (1951).

[13] Fineman M., Ross S. P.: Linear method for determining monomer reactivity ratios in copolymerization. Journal of Polymer Science, **5**, 259–262 (1950).

[14] Kelen T., Tüdős F.: Analysis of the linear methods for determining copolymerizatiom reactivity ratios I. A new improved linear graphical method. Journal of Macromolecular Science: Pure and Applied Chemistry, **9**, 1–27 (1975).

[15] Kelen T., Tüdős F., Turcsányi B., Kennedy J. P.: Analysis of the linear method for determining copolymerization reactivity ratios. IV. A comprehensive and critical re-examination of carbocationic copolymerization data. Journal of Polymer Science, **15**, 3047–3074 (1977).

[16] Hagiopol C.: Copolymerization- towards a systematic approach. Kluwer-Academic/Plenum Publisher, New York (1999).

[17] Hagiopol C, Frangu O.: Strategies in improving the accuracy of reactivity ratios estimation. Journal of Macromolecular Science: Pure and Applied Chemistry, 40 , 571–584 (2003).

eXPRESS Polymer Letters Vol.1, No.6 (2007) 397–405
Available online at www.expresspolymlett.com
DOI: 10.3144/expresspolymlett.2007.56

UV curing of a liquid based bismaleimide-containing polymer system

S. L. Fan[1,2], *F. Y. C. Boey*[2], *M. J. M. Abadie*[1,2*]

[1]Laboratory of Polymer Science & Advanced Organic Materials – LEMP-MAO, CC 021, Université Montpellier 2, Place E.Bataillon, 34095 Montpellier, France
[2]School of Materials Science and Engineering, Nanyang Technological University, 50 Nanyang Avenue, 639798 Singapore

Received 2 April 2007; accepted in revised form 12 May 2007

Abstract. A new liquid formulation of commercial bismaleimide and n-acryloylmorpholine was prepared that could be UV cured as an alternative to traditional thermal cure methods presently used for BMI in the industry. UV curing was shown to be an efficient method which promoted the reaction rate significantly and was able to achieve this at low temperatures (30–50°C). A free radical polymerization approach has been used to explain the cure mechanism and cure kinetics, using data elucidated from the DPC and FTIR. The cured thin film was shown to achieve very high thermal stability (~400°C), with the BMI shown to retard the thermal degradation temperature and rate.

Keywords: *thermosetting resins, bismaleimide, UV curing*

1. Introduction

Bismaleimide resins are well-known for their high performance since 1960s. As an ideal thermal resistant resins filling in the margin between epoxies and polyimides, bismaleimide also possesses some other remarkable properties such as low moisture absorption, highly crosslinked structures, high chemical resistance, high mechanical stability, etc. These advantages make bismaleimide applied widely in adhesive, packaging and aerospace industry. However two shortcomings, namely brittleness and poor process ability, have limit commercial bismaleimide for further application. These two drawbacks are due to the high density of crosslink and high crystalline content. Many investigations have been done or are focused on improving its properties in order to increase the application [1–7]. Other papers have shown the cure mechanism and kinetics for BMI and modified BMI systems during thermal curing [2, 8–10].

Several methods have been used to improve the processibility of bismaleimide [11]. Critical to this is the ability to process BMI into a liquid form with similar behavior to epoxy, for example [12]. This is done by formulations which include synthesizing of new liquid BMI resins through modification of the BMI molecule with other molecules and copolymers, or dissolving BMI into reactive organic diluents. Currently, bismaleimide 36 carbon cycloaliphatic branched structure (Q-Bond) [13] and polypropylenoxide–bismaleimide (MIA) [14] are two liquid BMI resins available, though they have very high viscosity and high cost. Attempts have been made to modify BMI by other molecules and copolymers to improve the processibility [15–16]. Typically, Cyanate ester [17] and diallyl bisphenol A [18] are used as copolymers to improve the processability. Dissolving conven-

---

[*]Corresponding author, e-mail: abadie@univ-montp2.fr

tional BMI resins into reactive organic diluents has proven difficult because of its low solubility and the requirement for high temperature thermal curing.

The use of radiation curing has been shown to give faster cure rates. This includes the use of microwave curing [19–21], UV [22–23] and e-beam [24–26] for curing of thin film thermosetting polymers have been shown to give practical and effective advantages [19–21].

N-acryloylmorpholine shows a capability to dissolve traditional BMI with high concentration. A liquid formulation which can be radiation cured enables it to be processed in more practical process methods, such as resin transfer molding (RTM) [3]. In addition, these cured products typically have better mechanical properties, especially improvement in its brittleness.

Although thermal curing is currently the most widely used method for curing BMI, it is also relatively low in efficiency and can have high cost. More recently, UV curing has been investigated by researchers such as Decker *et al.* [13]. The new curing method possesses many advantages, such as room temperature cure, high reaction rate, energy efficiency, low volatility of organic compound and easy control. The UV cure mechanism and kinetics for homo- and copolymerization of BMI, and their final cure properties were reported [2, 27, 28].

This paper reports on the study of a new liquid formulation for a BMI/n-acryloylmorpholine polymer system for UV curing. The photo polymerization behavior was investigated in situ by using a Differential Photo Calorimeter. The parameters for the cure kinetics were elucidated and the cure mechanism was proposed. The thermal stability of the material as a thin film was also studied.

2. Experimental

2.1. Materials

1,1’-(methylenedi-4,1-phenylene)-bismaleimide (BMI) was obtained from Aldrich Chemicals; n-acryloylmorpholine (AMP) was purchased from Polyscience, Inc. IRGACURE1000 was obtained from the Ciba Chemical Company and was used as photoinitiator. All chemicals were used without further purification. The structures of the chemicals are given in Figure 1.

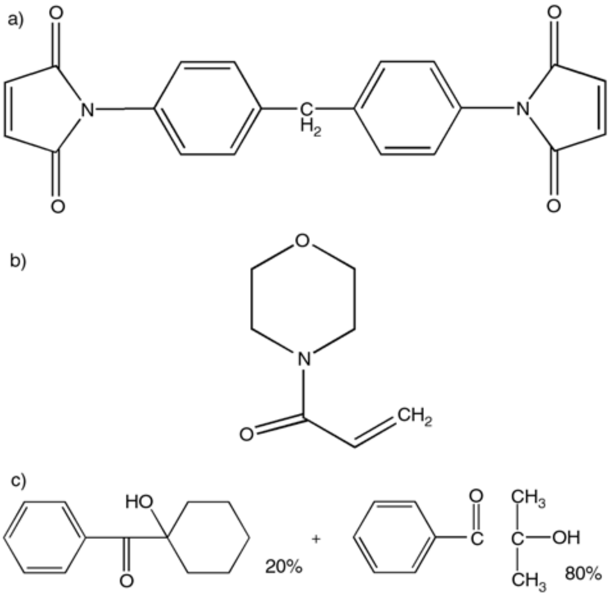

Figure 1. The chemical structures. a) 1,1'-(methylenedi-4,1-phenylene)-bismaleimide (BMI), b) N-Acryloylmorpholine, c) IRGACURE1000

2.2. Methods

2.2.1. Preparation of liquid formulation

The solubility of BMI in AMP was tested and the highest solubility is about 1:3 by molar ratio of carbon double bond (BMI:AMP) at 110°C. There was a critical point at 70°C where the solubility had a sudden increase. The liquid formulation was prepared in a brown bottle with magnetic stirring at 70°C. BMI powders dissolved and brown transparent solution was formed. A series of liquid formulations were prepared and the components are listed in Table 1.

Table 1. The components of liquid formulations

System	AMP [% by weight]	BMI [%]	Photoinitiator [%]
1	100	0	3
2	90	10	0
3	90	10	3
4	80	20	3

2.2.2. UV irradiation

The photopolymerization was conducted by using a Differential Photo Calorimeter (DPC) which recorded the real-time exothermal heat of reaction and calculated the kinetics of reaction. The intensity of the UV source was fixed at 18.5 mW/cm^2. About 1 mg of the sample was transferred into an aluminum pan and then placed into the DPC cell. A polyethyleneterephtalate film was used to cover the sample in order to prevent the oxygen diffusion and planarize the liquid film. A fully cured BMI/AMP film was used as reference. The sample was exposed isothermally from 5 to 10 minutes at different temperatures from 30 to 90°C with purge nitrogen.

2.2.3. Characterization

The FTIR was employed to monitor changes in C=C absorption in order to ascertain the formation of sequential product. The experiments were conducted in absorption mode at 4 cm^{-1} resolution with 32 scans per spectrum. A Spectrum GX System FTIR spectrometer, Perkin Elmer Instruments, was used.

The Differential scanning calorimetry (DSC) was performed at a heating rate of 10°C/min using a DSC 2920, TA Instruments Inc, to obtain the cure or thermal behavior information of these systems. The Glass transition temperature (T_g) was measured by a Modulated DSC system. Thermal degradation was investigated by using the TGA in a nitrogen atmosphere with a heating rate of 10°C/min till 700°C.

3. Results and discussions

The liquid formulations of bismaleimide/n-acryloylmorpholine with low viscosity have been prepared. Here we report the investigation of UV curing behaviors and the characterization of thermal properties.

Figure 2 is the DPC plot of four systems: AMP with photoinitiator, AMP/BMI without photoinitiator and AMP/BMI with photoinitiator (different concentration). An obvious exothermal peak was observed in each curve except the one of AMP/BMI without photoinitiator. The UV curing polymerization proceeded very fast and finished in several minutes, proving that this technique is more efficient than conventional thermosetting method. BMI was reported to have a capability to initiate a photopolymerization in some systems via accepter-donor mechanism [2, 27, 28], but for this study, a repetition of this capability could not be achieved. AMP resins polymerized very fast and the reaction completed within second. Christian Pichot indicated that the conversion could achieve nearly 100% for homopolymerization [29]. However, the exothermal peak drops down gradually with increasing BMI content, which indicated that bismaleimide has a negative influence on the photopolymerization behavior. This could be because BMI increases the viscosity of the liquid formulation and forms crosslink structure in the film. Table 2 lists some reaction parameters which also disclose the effect from bismaleimide. For example, the induction time expends from 1.7 s to 4.1 s at 50°C with an increase of BMI, while the enthalpy decreases from 511.7 J/g to 384.8 J/g.

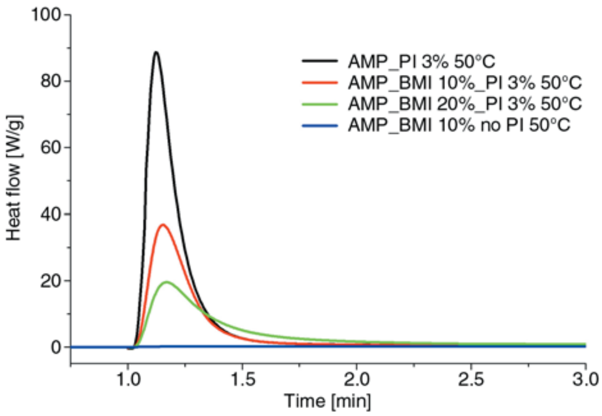

Figure 2. DPC plot of different systems

Figure 3 describes the effect of the ambient temperature on the effectiveness of photopolymerization. According to the enthalpy value (Table 2), the highest conversion was achieved at 50°C, and then dropped with higher temperature. This could be because of the competition between propagation and termination in free-radical mechanism. Another explanation is that some of the AMP resins evaporated during UV curing, so the enthalpy only

Table 2. The kinetics data of UV polymerization

	AMP				AMP + 10% BMI				AMP + 20% BMI			
***T* [°C]**	**ΔH**	**MP**	**RP**	**IT**	**ΔH**	**MP**	**RP**	**IT**	**ΔH**	**MP**	**RP**	**IT**
30	474.4	3.6	27.1	1.6	335.6	8.0	24.0	3.4	310.9	10.8	20.0	4.7
50	511.7	3.8	24.8	1.7	405.1	8.0	29.6	3.5	384.8	10.0	22.5	4.1
70	503.6	4.0	31.3	1.6	405.6	9.2	30.7	3.7	355.4	11.4	23.8	4.1
90	489.0	4.0	30.5	1.5	379.2	7.6	24.6	2.9	235.8	10.4	18.9	3,8

ΔH: enthalpy [J/g]; MP: maximum peak [s]; RP: reaction at peak [%]; IT: induction time [s]

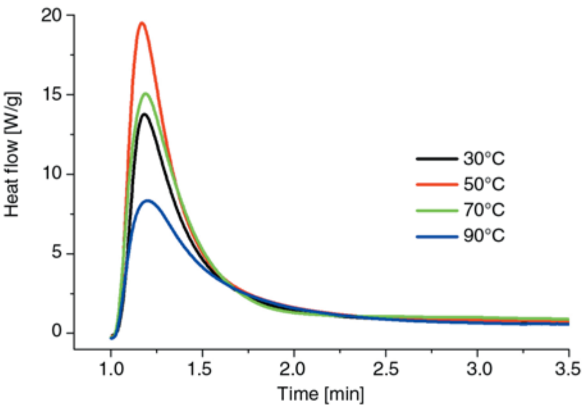

Figure 3. The temperature influence on UV curing. DPC plot of AMP/20% BMI/3% PI, 30–90°C

came from the remaining reactants. It is also possible that because of the relevant high concentration of photoinitiator, a thin film forms on the surface of sample, which absorbs much of UV light and acts as a shield to prevent the UV light penetrating into the bulk of liquid formulation, then the reaction stops. Anyway, this can be avoided by decreasing the concentration of photoinitiator and the thickness of the sample. The induction time (1% conversion) decreased with the rising of temperature, which is reasonable because resins become more active and easier to react at higher temperature.

3.1. Kinetics of photopolymerization

Cure kinetics is typically used to understand the cure reaction process quantitatively [30]. The results of the DPC gave the real-time exothermal heat which could then be used to calculate the kinetics of reaction. The conversion degree is calculated by Equation (1):

$$a = \frac{H_t}{H_{total}} \cdot 100\ [\%] \qquad (1)$$

where H_t is the sum of exothermal heat at time t, H_{total} is the total reaction heat (enthalpy), a is the conversion degree. The theoretical enthalpy of acrylate polymerization is 80.5 kJ/mol, [31] which is a little higher than the one of AMP resins, 72.3 kJ/mol. Our analysis and calculation are based on the assumption that the system reacted completely at 50°C because it's hard to get the H_{total} for 100% conversion. Anyway, a and H_t have a linear relationship, so the curve keeps the same shape no matter how much the ideal H_{total} is.

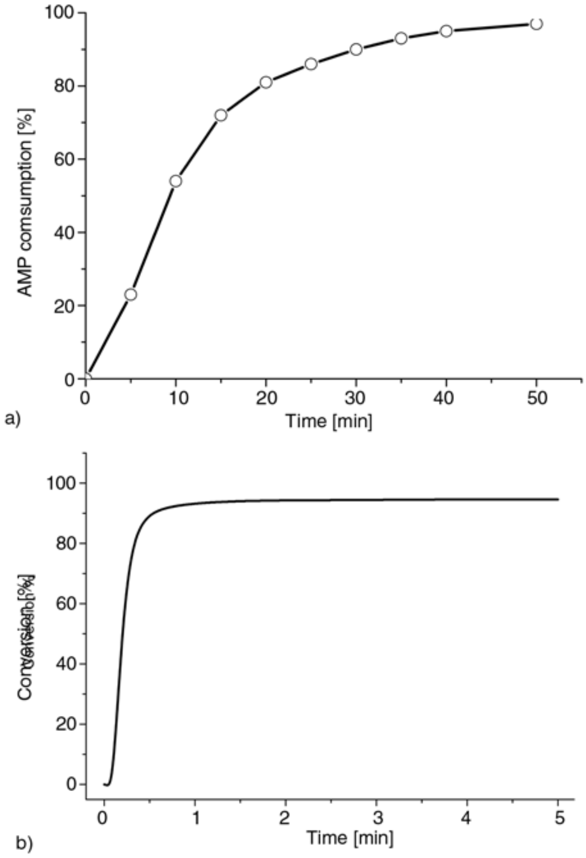

Figure 4. The compare of conversion *vs.* time for AMP homopolymerization in bulk solution and under UV curing. a) in 1,4-dioxane solution [29], b) by UV irradiation

For AMP/BMI system, homo- and copolymerization occurred simultaneously, so the calculation yielded the conversion of the overall reaction. Figure 4 compares the conversion of AMP polymerization in bulk for thermal curing to the conversion for a thin film by UV curing. The higher final percentage conversion and faster polymerization rate obtained for the latter demonstrate that the photoinitiated radical method is more efficient than for thermal curing.

The reaction rate can be calculated by Equation (2):

$$\frac{\mathrm{d}a}{\mathrm{d}t} = \frac{\Delta H_t}{\Delta t} \qquad (2)$$

Again, the calculation is for the overall reaction rate. Figure 5 plots the derivatives of the conversion versus time. The curve is typical for an autocatalytic kinetics type reaction. The results also show that high temperature has a negative effect to the reaction rate. Freddy also reported the kinetics of BMI with an organic reactant, but in thermal curing mechanism [32]. In his paper, the reaction fol-

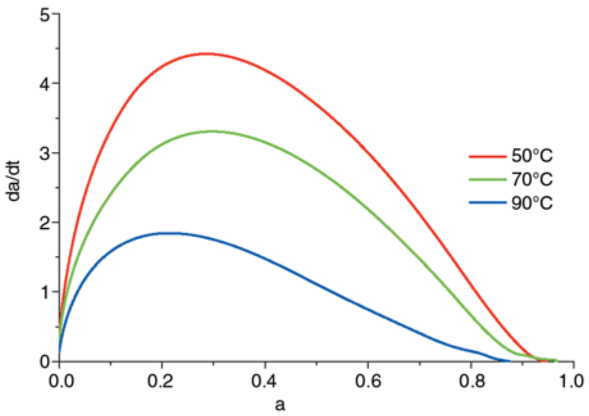

Figure 5. The overall reaction rate versus conversion of AMP/10%BMI/3%PI system

lowed the nth order model and the highest reaction rate is about 0.2 min^{-1}, much slower than the one of UV curing.

An autocatalytic kinetics model can be described by Equation (3):

$$\frac{da}{dt} = ka^m(1-a)^n \quad (3)$$

where d*a*/d*t* is the polymerization rate, *a* is the fraction of reactant converted, *k* is the Arrhenius-type reaction rate coefficient, *m* is the order of the initiation reaction, and *n* is the order of the propagation reaction. Empirically, *n* is assumed to be similar in value for different cure temperatures, and fixed to 1.5, *m* can be calculated. The kinetics parameters are listed in Table 3. These values are coincident with the analysis of DPC plot (Figures 2 and 3).

The rate coefficient, *k*, which is temperature dependent, can be used to calculate the activation energy of the reaction (Equation (4)).

$$k = A\exp\left(-\frac{E_a}{RT}\right) \quad (4)$$

where E_a is the overall activation energy, *A* is the overall frequency factor, *R* is the ideal gas constant, and *T* is the absolute temperature in Kelvin. When the sample is cured isothermally, if the Arrhenius relation is obeyed, the activation energy and frequency factor can be determined from the slope and intercept, respectively, of the best-line fit of Arrhenius plot by ln(*k*) *versus* 1/*T* (Equation (5)).

Table 3. Lists of the kinetics parameters

	AMP-10%BMI		AMP-20%BMI	
	m	**k**	**m**	**k**
30	0.479	11.7	0.332	5.83
50	0.675	21.8	0.364	7.04
70	0.661	17.8	0.418	6.55
90	0.386	10.0	0.249	4.03

$$\ln(k) = \ln(A) - \frac{E_a}{RT} \quad (5)$$

The calculated values of E_a and *A* are shown in Table 4. Normally an increase in the speed of the reaction should be reflected in an increase in the collision factor. In our case, the calculated E_a and *A* are coincident to the general conclusion. Boey *et al* studied the kinetics of thermal curing of BMI and modified BMI, the activation energy is about 95 J/g, [32] which is a little more than the one of UV curing, 64.6 J/g.

Table 4. The activation energy and frequency factor for AMP/BMI systems

	AMP-10% BMI	AMP-20% BMI
E_a [kJ/mol]	9.4±0.5	2.6±0.1
A [min^{-1}]	557.7	17.2

3.2. The mechanism of UV curing

N-acryloylmorpholine, which contains the acrylate function group, when cured using UV, follows a photo induced free radical polymerization mechanism [32]. Figure 6 shows a hypothesis structure of the AMP-BMI copolymer. The functionality of BMI ($f = 2$) would have made the film into an effectively 3-D network structure. The microstructure arrangement of the polymer phases of AMP and BMI is not clear. AMP and BMI are not in stoichiometric equilibrium because of the limited solubility of the latter. The final products may consist of homopolymerization of AMP, homopolymerization of BMI and copolymer of AMP and BMI, plus other side products.

The possible changes in the chemical bonds during the cure reaction have been analyzed using the FTIR method. The results in Figure 7 show the IR spectra of the monomers and cured polymers. The peaks at 790.7 and 950.7 cm^{-1}, which represent the C=C bond in AMP, have disappeared after polymerization. The strong absorption at 1234.2 cm^{-1} is identified as the C–N–C stretching vibration, weakened after polymerization. The absorption at 1610 cm^{-1}, representing the C=C stretching vibration has disappeared after irradiation. The absorptions at 692.3 cm^{-1} (C–H out-of-plane deformation

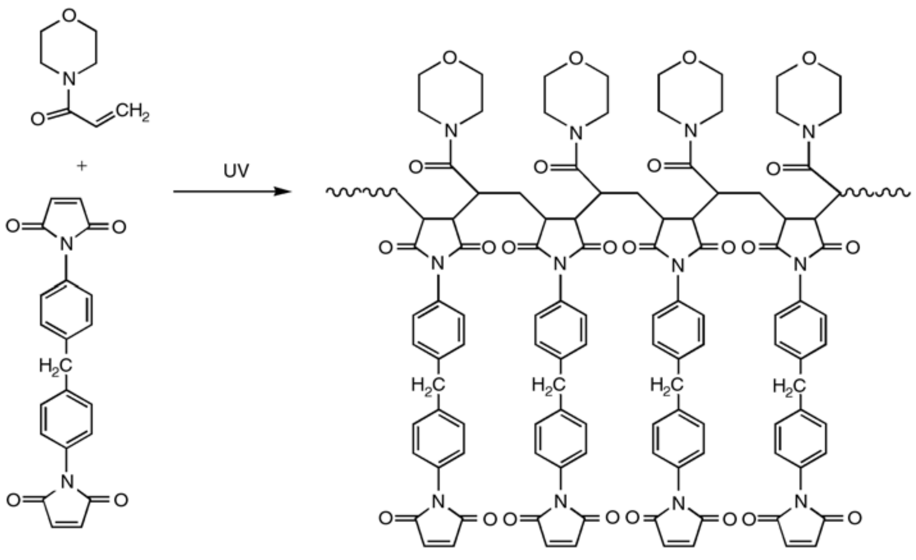

Figure 6. Scheme of co-polymerization of AMP-BMI

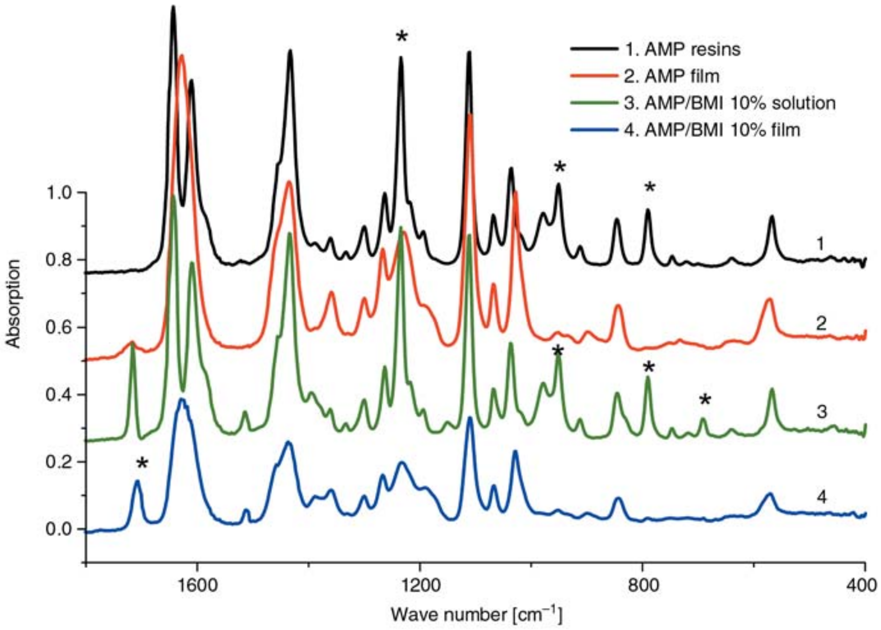

Figure 7. FTIR spectra of AMP-BMI systems: 1) AMP resins; 2) AMP films; 3) AMP/BMI 10% solution; 4) AMP/BMI 10% film

vibration), 1394.3 cm^{-1} (C=C stretching vibration), 1513.9 cm^{-1} (maleimide) are characteristic for bismaleimide. The absorption at 692.3 cm^{-1} is typically used to probe the concentration of BMI quantitatively and qualitatively. The peak has disappeared after irradiation, indicating that most of the BMI has been polymerized.

3.3. Thermal stability of AMP-BMI systems

Post curing process was conducted by using DSC with nitrogen purge to increase the conversion degree and to observe the performance of raw materials and product at high temperature. Figure 8 and Figure 9 compare the behaviors of the uncured polymer and the UV cured films. In Figure 8, it is seen that pure AMP resins started to polymerize by thermosetting at about 140°C and reached maximum rate at 170°C. It is also seen that by adding 10% BMI, the thermal cure peak is shifted to the right by about 30°C. This perhaps comes from the pre-reaction between AMP and BMI in the liquid formulation. The exothermic heat of thermosetting curing was calculated by integrating the curve of the exothermic peak in Figure 8, which is about 350 J/g, less than UV curing (~500 J/g, in Table 2). The small peak in DSC plot of AMP/BMI10%

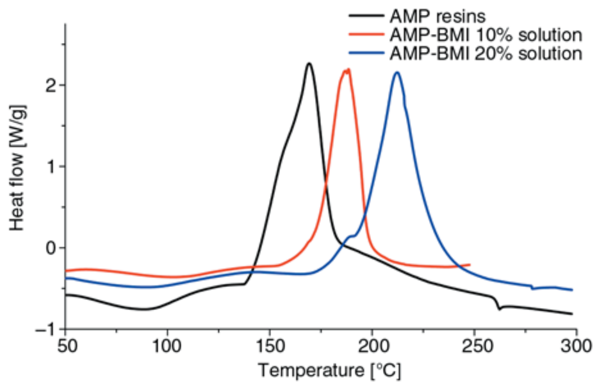

Figure 8. The DSC plot of liquid formulations of AMP/BMI systems

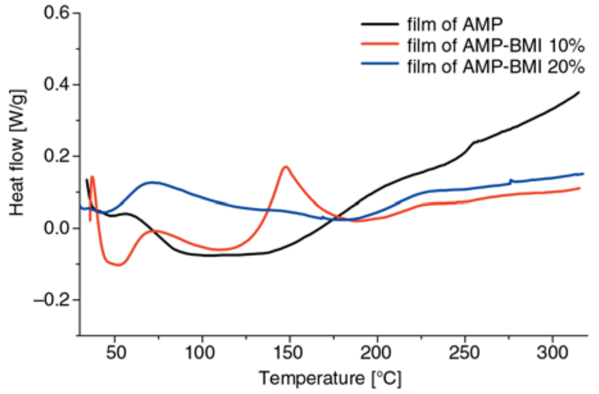

Figure 9. The post cure DSC plot after UV irradiation

cured film seen in Figure 9 is probably due to residual unreacted AMP or BMI resins.

3.4. Thermal degradation of AMP-BMI systems

The thermal degradation was investigated by using TGA. The plot is shown in Figure 10. Table 5 lists the temperatures for weight loss of 5% ($T_{5\%}$), the temperatures at maximum weight loss rate (T_{max}), maximum weight loss rate (R) and percentage char yield at 700°C (Y_c), to analyze the thermal stability. The addition of BMI decreased the conversion degree and also resulted in the production of oligomers in the process, which impaired the thermal stability of the polymer, resulting in a lower degradation temperature (comparing the $T_{5\%}$ values in Figure 10). Figure 11 plots the derivative of the Y-axis values in Figure 10. The resulting lot shows that addition of BMI clearly decreased the degradation rate, which is perhaps due to the crosslinking network structure in the film which limited the diffusion rate of broken segments, and also due to the high thermal stability of BMI itself.

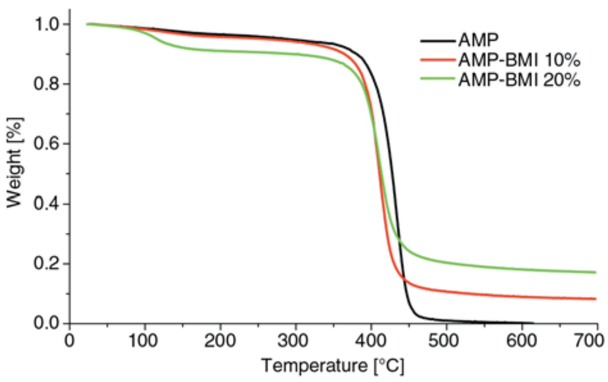

Figure 10. The TGA plot of AMP and AMP-BMI systems. 10°C/min

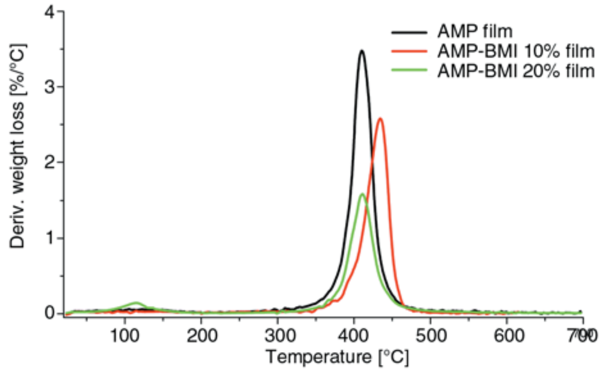

Figure 11. The derivation of TGA plot: AMP and AMP-BMI systems

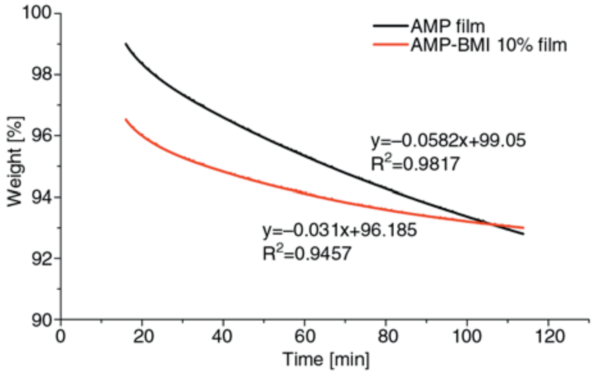

Figure 12. The isothermal TGA plot and calculation of degradation rate for the duration of thermal resistance: AMP and AMP-BMI10% films at 300°C

Table 5. Degradation results for AMP-BMI systems*

Composite	$T_{5\%}$ [°C][a]	T_{max} [°C][a]	R [%/°C][b]	Y_c at 700°C [%][c]
AMP	289.0	410.4	3.48	0.02
AMP-BMI 10%	263.2	434.2	2.58	8.23
AMP-BMI 20%	142.6	411.1	1.58	17.2

*reported data is an average of 5 samples, the standard derivation is around

[a] 5°C,

[b] 0.5%,

[c] 1%

The duration of the thermal stability was studied isothermally at 300°C for 100 minutes by using TGA. Figure 12 records the weight percent *versus* isothermal time. The curves show linear tendency, so we make a mathematical simulation of the relationship between weight and time by using a linear model. The results are listed as Equations (6) and (7):

$$y = -0.0582x + 99.05 \qquad R^2 = 0.9817 \tag{6}$$

$$y = -0.031x + 96.185 \qquad R^2 = 0.9457 \tag{7}$$

where y is the weight percent, x is the isothermal time. Equation (6) is for pure AMP film and Equation (7) is for AMP/BMI film. The slopes, representing the isothermal degradation rate, 0.0582 *vs.* 0.031%/min, indicate that BMI can slow down the degradation behavior. It is noted here that the simulation is only used to show the difference of thermal resistance between two materials, it doesn't refer to the degradation mechanism.

4. Conclusions

An initially liquid modified n-acryloylmorpholine/BMI was developed which could be UV cured. The formulation exhibited higher reactivity under UV curing compared to conventional thermal curing. A free radical mechanism was proposed which was elucidated using the DPC and FTIR. The overall curing kinetics parameters, such as reaction rate coefficient, the order of initiation reaction, activation energy and frequency factor were calculated by using isothermal DPC method. The relationship between reaction rate and conversion was obtained from this study. The thermal stability of the new formulation was also shown to be improved over thermally cured systems, with the stability reaching as high as 400°C; this was attributed to the significant increase in the BMI content for the system.

References

[1] Liu Y-L., Chen Y-J.: Novel thermosetting resins based on 4-(N-maleimidophenyl) glycidylether: II. Bismaleimides and polybismaleimides. Polymer, **45**, 1797–1804 (2004).

[2] Meng J., Hu X, Boey F. Y. C., Li L.: Effect of layered nano-organosilicate on the gel point rheology of bismaleimide/diallylbisphenol A resin. Polymer, **46**, 2766–2776 (2005).

[3] Boey F. Y. C., Song X. L., Yue C. Y., Zhao Q.: Effect of AlN fillers on the properties of a modified bismaleimide resin. Journal of Materials Processing Technology, **90**, 437–439 (1999).

[4] Hu X., Fan J., Yue C. Y.: Rheological study of crosslinking and gelation in bismaleimide/cyanate ester interpenetrating polymer network. Journal of Applied Polymer Science, **80**, 2437–2445 (2001).

[5] Fan J., Hu X., Yue C. Y.: Static and dynamic mechanical properties of modified bismaleimide and cyanate ester interpenetrating polymer networks. Journal of Applied Polymer Science, **88**, 2000–2006 (2003).

[6] Fan J., Hu X., Yue C. Y.: Dielectric properties of self-catalytic interpenetrating polymer network based on modified bismaleimide and cyanate ester resins. Journal of Polymer Science Part B: Polymer Physics, **41**, 1123–1134 (2003).

[7] Meng J., Hu X., Boey F. Y. C., Li L.: Effect of layered nano-organosilicate on the gel point rheology of bismaleimide/diallylbisphenol A resin. Polymer, **46**, 2766–2776 (2005).

[8] Boey F. Y. C., Santosh K. R.: Microwave radiation curing of polymers: Using a temperature equivalent method for cure reaction analysis. Advances in Polymer Technology, **19**, 194–202 (2000).

[9] Chia H. L., Jacob J., Boey F. Y. C.: The microwave radiation effect on the polymerization of styrene. Journal of Polymer Science Part A: Polymer Chemistry, **34**, 2087–2094 (1996).

[10] Boey F. Y. C., Yap B. H.: Microwave curing of an epoxy-amine system: effect of curing agent on the glass-transition temperature. Polymer Testing, **20**, 837–845 (2001).

[11] Abadie M. J. M., Xiong Y., Boey F. Y. C.: UV photo curing of *N,N'*-bismaleimido-4, 4'-diphenylmethane. European Polymer Journal, **39**, 1243–1247 (2003).

[12] Boey F. Y. C., Rath S., Ng A. K., Abadie M. J. M.: Cationic UV cure kinetics for multifunctional epoxies. Journal of Applied Polymer Science, **86**, 518–525 (2002).

[13] Decker C., Bianchi C., Morel F., Jönsson S., Hoyle C.: Mechanistic study of the light-induced copolymerization of maleimide/vinyl ether systems. Macromolecular Chemistry and Physics, **201**, 1493–1503 (2000).

[14] Bongiovanni R., Sangermano M., Malucelli G., Priola A.: UV curing of photoinitiator-free systems containing bismaleimides and diacrylate resins: bulk and surface properties. Progress in Organic Coatings, **53**, 46–49 (2005).

[15] Rao B. S.: Synthesis, characterization, and thermal stability of bismaleimides derived from maleimido benzoic acid. Journal of Polymer Science Part A: Polymer Chemistry, **27**, 2509–2518 (1989).

[16] Giulio D., Gautier C. M., Jasse B.: Fourier transform infrared spectroscopic characterization of aromatic bismaleimide resin cure states. Journal of Applied Polymer Science, **29**, 1771–1779 (1984).

[17]Gu A. J. : High performance bismaleimide/cyanate ester hybrid polymer networks with excellent dielectric properties. Composites Science and Technology, **66**, 1749–1755 (2006).

[18] Iijima T., Hayashi N., Oyama T., Tomoi M. : Modification of bismaleimide resin by soluble poly(ester imide) containing trimellitimide moieties. Polymer International, **53**, 1417–1425 (2004).

[19] Abadie M. J. M., Chia N. K., Boey F. Y. C.: Cure kinetics for the ultraviolet cationic polymerization of cycloliphatic and diglycidyl ether of bisphenol-A (DGEBA) epoxy systems with sulfonium salt using an auto catalytic model. Journal of Applied Polymer Science, **86**, 1587–1591 (2002).

[20] Boey F. Y. C., Chia N. K., Rath S. K., Abadie M. J. M., Gan G. K.: Low-energy electron beam-induced cationic polymerization with onium salts. Journal of Applied Polymer Science, **82**, 3099–3108 (2001).

[21] Rath S. K., Boey F. Y. C., Abadie M. J. M.: Cationic electron-beam curing of a high-functionality epoxy: effect of post-curing on glass transition and conversion. Polymer International, **53**, 857–862 (2004).

[22] Boey F. Y. C., Xiong Y., Rath S. K.: Glass-transition temperature in the curing process of bismaleimide modified with diallylbisphenol A. Journal of Applied Polymer Science, **91**, 3244–3247 (2004).

[23] Boey F. Y. C., Song X., Rath S. K., Yue C. Y.: Cure reaction for modified diallylbisphenol A/diaminodiphenylsulfone/bismaleimide. Journal of Applied Polymer Science, **85**, 227–235 (2002).

[24] Boey F. Y. C., Qiang W.: Experimental modeling of the cure kinetics of an epoxy-hexaanhydro-4-methylphthalicanhydride (MHHPA) system. Polymer, **41**, 2081–2094 (2000).

[25] Boey F. Y. C., Song X. L., Yue C. Y., Zhao Q.: Modeling the curing kinetics for a modified bismaleimide resin. Journal of Polymer Science Part A: Polymer Chemistry, **38**, 907–913 (2000).

[26] Boey F. Y. C., Qiang W.: Glass-transition temperature-conversion relationship for an epoxy-hexahydro-4-methylphthalic anhydride system. Journal of Applied Polymer Science, **78**, 511–516 (2000).

[27] Decker C., Bianchi C., Jönsson S.: Light-induced crosslinking polymerization of a novel N-substituted bis-maleimide monomer. Polymer, **45**, 5803–5811 (2004).

[28] Morel F., Decker C., Jönsson S., Clark S. C., Hoyle C. E.: Kinetic study of the photo-induced copolymerization of N-substituted maleimides with electron donor monomers. Polymer, **40**, 2447–2454 (1999).

[29] D'Agosto F., Charreyre M., Veron L., Lauro M., Pichot C.: Kinetic study of free-radical solution copoly-merization of N-acryloylmorpholine with an activated ester-type monomer, N-acryloxysuccinimide. Macromolecular Chemistry and Physics, **202**, 1689–1699 (2001).

[30] Boey F. Y. C., Qiang W.: Determining the gel point for an epoxy-hexaanhydro-4-methylphthalic anhydride (MHHPA) system. Journal of Applied Polymer Science, **76**, 1248–1256 (2000).

[31] Pappas S. P.: Radiation curing: science and technology. Plenum Press, New York (1992).

[32] Xiong Y., Boey F. Y. C., Rath S. K.: Kinetic study of the curing behavior of bismaleimide modified with diallylbisphenol A. Journal of Applied Polymer Science, **90**, 2229–2240 (2003).